ESTIMATING ELECTRICAL PARAMETERS OF THE HEART USING DIFFUSION MODELS AND ECG/MCG SENSOR ARRAYS

ESTIMATING ELECTRICAL PARAMETERS OF THE HEART USING DIFFUSION MODELS AND ECG/MCG SENSOR ARRAYS

By

RUND ABOU-MARIE, B.ENG. (MCMASTER UNIVERSITY)

A Thesis

Submitted to the School of Graduate Studies

In Partial Fulfillment of the Requirements

For the Degree

Masters of Applied Science in Engineering

McMaster University

MASTER OF APPLIED SCIENCE (2007)

(Electrical and Computer Engineering)

McMASTER UNIVERSITY

Hamilton, Ontario, Canada

TITLE: Estimating Electrical Parameters of the Heart Using

Diffusion Models and ECG/MCG Sensor Arrays

AUTHOR: Rund Abou-Marie

SUPERVISORS: Dr. Aleksandar Jeremic

NUMBER OF PAGES: xii, 98

ABSTRACT

The estimation of physiological parameters that characterize electrical signal propagation in the heart is an important component of the inverse problem in electrocardiography. Recent studies show that some patterns in cardiac electrical signals (e.g. spiral waves) are associated with the re-entrance phenomenon seen in cardiac arrhythmia. Therefore, further research in this field will lead to improved detection and diagnosis of cardiac diseases and conditions.

Electrical activity in the heart is initiated at the SA node and an electrical impulse propagates to the atria causing their mechanical contraction. Subsequent contraction of the ventricles (systole) followed by relaxation (diastole) completes the heart cycle. Evidence of electrical activity in cardiac cells is shown by a potential difference across the cell membrane that changes when ionic currents flow through the membrane's channels. This electrical activation of the heart can be modeled using a diffusion model in which the physiological parameters (e.g., conductivity) govern the resulting spatio-temporal process.

In this thesis we derive an inverse model for the electrical activation of the heart using the Fitzhugh-Nagumo diffusion equations which account for the dynamics of spiral waves in excitable media such as, in our case, cardiac cells. The electric potential is expressed through activator and inhibitor variables and we simulate the measurements of the electromagnetic field are on the torso surface. A signal processing model is derived

where the physiological parameters are deterministic or stochastic, and the resulting physiological measurements are a function of space, time, and the parameters.

We estimate these unknown parameters using an optimization algorithm that minimizes the cost function of the model. For our estimation we use Least Squares and we derive the Maximum Likelihood Estimator. We measure the performance using mean square error, and we compute the Cramer-Rao Lower Bound, which shows the minimum variance attainable.

In our simulations we use a finite element mesh of a human torso to describe a realistic geometry to generate the potentials on the surface. Our results indicate that estimating the physiological parameters of a diffusion equation from the measurements taken outside the torso are feasible. This further suggests that ECG/MCG signals can be used to provide detailed information about the physiological properties of the electrical impulse generated in the heart and aid in diagnosis of various pathological conditions including arrhythmia.

ACKNOWLEDGEMENTS

NOMENCLATURE

ECG   –   *Electrocardiogram*

MCG   –   *Magnetocardiogram*

SQUID –   *Super Conducting Quantum Inference Devices*

V   –   *Electric Potential*

B   –   *Magentic Potential*

E   –   *Electric Field*

J   –   *Current Density*

Q   –   *Charge*

Na   –   *Sodium*

K   –   *Potassium*

D   –   *Diffusion Coefficient*

ϕ –   *Concentration of Ions*

∇ –   *Gradient*

∇^2 –   *Laplacian*

μ_0 –   *Peremeability of Vaccum*

σ –   *Conductivity*

N   –   *Normal Distributioin*

E   –   *Expected Value*

F   –   *Faradays Constant*

TABLE OF CONTENTS

LIST OF FIGURES

1   INTRODUCTION

In electrocardiography the goal is to describe the electrochemical activity of each cell in the heart through the acquisition and interpretation of electric potentials on the torso surface. As a non-invasive and practical diagnostic tool, the main objective is to gain a better understanding of the electrical activity in the heart. From an academic standpoint the gathering of information about the heart provides insight into regional and localized areas within the heart's chambers and will increase the accuracy of future cardiac models. From a clinical aspect, creating a clear image of the heart's activation process plays a key role in the early detection and treatment of cardiac diseases [Jeremic, 2000].

Modeling the cardiac activation at the microscopic level is a subject of extensive research and is commonly described as the 'forward' problem. There exist numerous models that describe membrane potentials such as the Hodgkin and Huxley, Fitzhugh-Nagumo, and Aliev and Panfilov models [Gulrajani, 1998(1)].   In all such models the activation wavefront is simulated using parameters for which we have *a priori* knowledge.

Conversely, the inverse problem in electrocardiography is the estimation of physiological parameters that characterize electrical signal propagation in the heart from surface measurements. In the clinical environment the main purpose of solving this problem is to reduce the amount of information and to quantify parameters; thus providing detailed information about the electrical impulse generated in the heart, and aiding in the diagnostics of various pathological conditions.

1.1 THE INVERSE PROBLEM IN ELECTROCARDIOGRAPHY

The inverse problem of electrocardiography is actually one that is made difficult by two characteristics. The first characteristic is that it does not have a unique solution - that is the relationship between the true cardiac source and remote observations are non-unique such that the same set of measurements could result from more than one source configuration [MacLeod, 1998]. The second problematic characteristic is that it is an ill-posed problem because of attenuation and smoothing of the electromagnetic fields in the medium between the source and observations. As explained in Macleod, 1998, recovering the sources from the resulting remote measurements requires amplification and 'unsmoothing'. Then if this is applied to measurements that contain unavoidable model error, the result can be large or discontinuous error in the solution. One way of improving the ill-posed problem is to use a set of constraints on the solution which will restrict the admissible class of solutions, so that a continuous inverse exists. These constraints can be related implicitly through the definition of the cardiac source when devising the problem [Jeremic, 2003].

The electrical activation in the heart can be modeled using a diffusion model in which the physiological parameters govern the resulting spatio-temporal process. In our study, we derive an inverse model for the electrical activation of the heart using the Fitzhugh-Nagumo reaction-diffusion equations which account for propagation of the action potential in excitable media such as, in our case, cardiac cells.

1.2 BACKGROUND SUMMARY

In this section we present a brief overview of cardiac physiology. The human heart is a muscular organ that is responsible for pumping blood through the arteries and veins by repeated rhythmic contractions. The heart is composed of cardiac muscle that has the ability to self-excite and stimulate contraction. Adjacent cells are connected by junctions called intercalated discs which play a vital role as they allow the muscle to contract rapidly as a unit [Martini, 1999]. These gap junctions allow ions and small molecules to move from one cell to another, which creates an electrical connection between the two muscle cells. Therefore, an action potential can travel across an intercalated disc, moving quickly from one cardiac muscle cell to another [Martini, 1999].

The heart is encased in a protective double-walled sac called the pericardium, which then consists of an inner layer called the epicardium. The epicardium can then be described as the outer layer of the heart itself, while the myocardium and endocardium form the middle and innermost layers, respectively. The myocardium is the thickest layer, and the endocardium has a smooth surface to allow blood to flow easily through the heart's chambers. [Barrill, 2004]

The heart consists of four chambers, two atria and two ventricles, which along with the anatomy in this section are depicted in Figure 1-1. Blood from the body is returned to the heart via the superior and inferior vena cava. It enters the right atrium, which when it contracts allows the blood to flow through the tricuspid valve and into the right ventricle. The contraction of the right ventricle pumps the blood to the lungs through the pulmonary valve and pulmonary artery. Oxygenated blood returns to the left atrium of the heart via

the pulmonary veins and when this atrium contracts, blood travels through the mitral valve and into the left ventricle. Then the contraction of the left ventricle pumps the blood through the aortic valve and into the aorta which distributes the blood to the rest of the body. Thus during each contraction or 'systole', blood is pumped into the lungs and to the body from the right and left ventricles, respectively. The heart then refills during relaxation, or 'diastole' [Gulrajani, 1998(1)].

Each contraction of the heart is preceded and triggered by the electrical activation of the myocardial cells. The electrical activity of the heart starts within the 'pacemaker' cells that are collectively known as the sino-atrial node. As mentioned earlier, these pacemaker cells are spontaneously active, generating an action potential at regular intervals that in turn triggers the normal heartbeat [Gulrajani, 1998(1)]. We detail the electrical conduction system of the heart later in this thesis.

1.3 OUTLINE OF EXISTING LITERATURE

The underlying processes that control the cardiac activation can be described on a molecular level by the movement of ions. Several electrodynamic models that relate the membrane potential to variations in ionic current have been described in literature. In 1952, Hodgkin and Huxley proposed the first quantitative model of wave propagation in squid nerve, which had a great impact on modeling various nonlinear phenomena in biology. Then, as explained in Panfilov, 1996, the first physiological model of cardiac tissue was developed in [Noble, 1962]. Further studies in this field resulted in the

development of realistic ionic models that accurately reproduce most of the basic properties of cardiac tissue, including the depolarization and repolarization of the membrane.

In [Fitzhugh, 1955] the Hodgkin and Huxley model is reduced to a two-dimensional differential equations system. In [Abboud, 1993] a model of the heart is constructed where a full cardiac cycle is simulated, imitating the physiological activation wavefront propagation. The authors show that the reaction-diffusion model defined by the Fitzhugh-Nagumo model can be used to exhibit properties such as oscillations and variable excitability in cardiac cells. Further in [Moreau-Villeger, 2004] a study using the Aliev and Panfilov model is described by the authors as an extension of Fitzhugh-Nagumo, and is used to estimate the electrical activity in canine hearts. It is evident that the simulation of cardiac activity using a reaction-diffusion model to describe the action potential has garnered considerable attention in the last decade. Complimentary to this, the field of inverse electrocardiography was summarized comprehensively for example, in reviews by [Rudy, 1988]. More recent publications by [Horacek, 1995] and [Gulrajani, 1998] have focused on formulating the inverse problem in ways that increase accuracy of results and remove obstacles to clinical application.

1.4 RESERCH OBJECTIVES

In this section we outline our research objectives in using a realistic torso mesh along with our derived inverse model for the electrical activation of the heart using the Fitzhugh-Nagumo reaction-diffusion equations.

1. Investigate the feasibility of using our derived algorithm for estimating parameters of the diffusion model using ECG and MCG arrays.

2. Determine and interpret whether the combination of ECG/MCG sensors versus ECG sensors alone contributes any additional, clinically relevant, information to our inverse problem.

3. Outline preliminary framework for future work

1.5 RESEARCH APPROACH

In our study we try to develop our numerical model in two main steps: First the computation of a transfer vector that establishes a relationship between the cardiac potentials and those on the torso surface. Then second, the solving of an optimization problem by using the aforementioned transfer vector. We outline our research approach in the following steps:

1. Develop a computational model which includes the use of a finite element method tool, along with a realistic mesh of the human torso to simulate the measurement of the electromagnetic field on the surface.

2. Derive a signal processing model whereby the physiological parameters and the resulting physiological measurements are a function of space, time, and the (possibly random) generated parameters. We do this for two cases; first with deterministic (and potentially unknown) heart parameters, and second the case where the parameters are assumed random.

3. Develop parametric statistical models for corresponding measurements from ECG / MCG sensor arrays in the presence of modeling noise

4. Solve the optimization problem using Nonlinear Least Squares to estimate unknown parameters, and compare with derived Maximum Likelihood Estimator

5. Compute the Cramer-Rao Lower Bound on the variance of the estimators to examine and analyze the performance.

1.6 THESIS LAYOUT

This thesis is comprised of six chapters. In Chapter 2 we introduce the reader to electrophysiology concepts that directly relate to this study. We then present the physical model including the governing diffusion equations. Chapter 3 discusses the mathematical model, where we introduce our software tools and present the analytical form for our forward spatio-temporal model. In Chapter 4 we describe the statistical model, including the development of our measurement model and estimation algorithms. Then in Chapter 5 we demonstrate the applicability of our research using numerical examples for least-squares and maximum likelihood estimation. In this chapter, we also present our performance analysis. We use mean square error and Cramer Rao lower bound computations to evaluate our results. Our study is concluded in Chapter 6 where we also discuss future directions for this research.
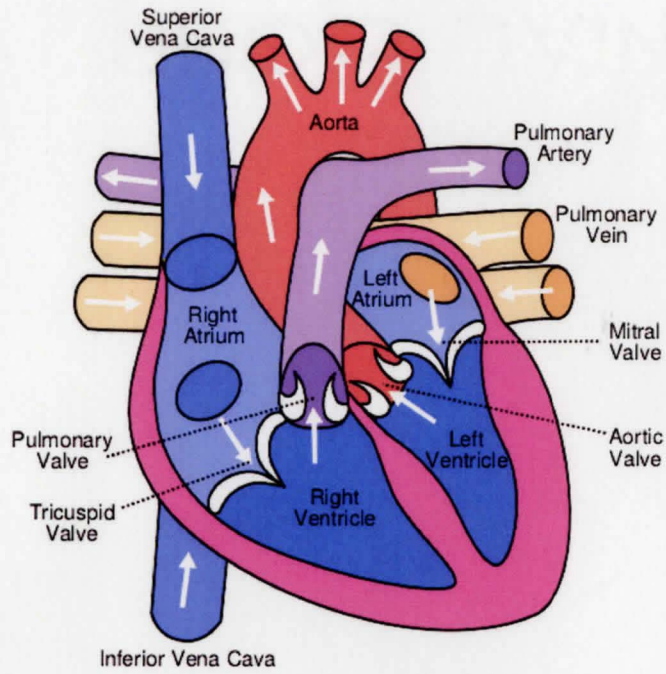
Figure 1 - 1: Anatomy of the Human Heart
* http://www.biomed.metu.edu.tr/courses/term_papers/artificial-hearts_gokduman.htm

2   PHYSICAL MODEL

2.1 ELECTRICAL ACTIVITY IN THE HEART

Electrical activity in the heart can be analyzed at the microscopic, mesoscopic and macroscopic levels. The flow of currents that control the cardiac activation can be described at the microscopic level as the exchange of ions between different cells. The mesoscopic level includes intracellular interactions in different regions, while the macroscopic scale describes the heart's behavior as an organ.

2.1.1 Cell Membrane

The cell membrane is described as a dielectric layer of phospholipids with a conducting electrolytic solution both inside and outside the cell [Guevara, 1991]. The membrane carries a potential across the inner and outer surfaces, and in Figure 2-1 we see that it can be modeled by a basic resistor-capacitor circuit, where C_m represents the membrane capacity [Durrer, 1970]. The dependence of the voltage across the membrane on the charge Q is expressed as,

$$V_m = \frac{Q}{C_m}$$

(1)

where we assume C_m is constant over time. The change of the voltage with respect to time is then expressed,

$$\frac{\partial V_m}{\partial t} = \frac{1}{C_m}\frac{\partial Q}{\partial t} = -\frac{\sum I_c}{C_m} \qquad (2)$$

where I_c denotes ionic currents that flow across the cell membrane at time t. The negative sign follows convention in representing the flow of positive ions out of the cell [Sasche, 2004].

The membrane of every cardiac cell is characterized by its selective permeability to ions. If the membrane is predominantly permeable to one specific ion, it will have an equilibrium voltage at which there is a balance of concentration. This voltage is defined by the Nernst Equation,

$$E_r = \frac{RT}{zF} ln \frac{C_o}{C_i} \qquad (3)$$

where T is the temperature, z is the charge on the specific ion, R is the gas constant, and F is Faraday's constant. C_o and C_i represent the concentrations of the ions outside and inside the cell, respectively.

2.1.2 Hodgkin and Huxley Model

The Hodgkin-Huxley Model is a set of non-linear ordinary differential equations that approximates the electrical characteristics of excitable cells such as neurons and cardiac muscle fibres. In [Hodgkin, 1951] a model that represents different types of ionic currents passing through the membrane is given by,

$$I = C_m \frac{\partial V_m}{\partial t} + I_i, \qquad (4)$$

where,

I is the total membrane current density

I_i is the total ionic current density consisting of different ionic components

V_m is the transmembrane voltage (intracellular potential-extracellular potential)

C_m is the membrane capacity

In Figure 2-1 we also see that the current in the membrane can be divided further to express the ionic current density as a sum of that carried by sodium (Na) , potassium (K) and other (mainly chloride) ions (L). This can be expressed,

$$I_i = I_{Na} + I_K + I_L \qquad (5)$$

A cell membrane's permeability to certain ions has a significant impact on the propagation of the action potential in the heart. In [Hodgkin, 1952] the authors showed that the ionic permeability of the membrane can be expressed using ionic conductance, and that the individual currents can be expressed as,

$$
\begin{aligned}
I_{Na} &= g_{Na}\left(V_m - E_{Na}\right) \\
I_K &= g_K\left(V_m - E_K\right) \\
I_L &= g_L\left(V_m - E_L\right)
\end{aligned}
\qquad (6)
$$

where g denotes the conductance and we use subscripts to denote the respective ion. The model equation is then summarized in the following expression,

$$C_m \frac{\partial V_m}{\partial t} = I - g_K n^4\left(V_m - E_K\right) - g_{Na}m^3 h\left(V_m - E_{Na}\right) - g_L\left(V_m - E_L\right) \qquad (7)$$

where the variables n, m, and h are so called gating variables that are dependent on the membrane potential. In developing this system of equations from their research, Hodgkin

and Huxley in fact provided a model that forms the basis for virtually all models of excitable membrane behavior [Bray, 2002].

2.1.3 Fitzhugh-Nagumo Model

The Fitzhugh-Nagumo model is a generic model that represents the reduced Hodgkin and Huxley model of the cell membrane. The model can be used to illustrate a cardiac cell's excitability, and its threshold phenomena, and in certain conditions the presence of oscillatory wave activity. Nagumo then applied it to an electrical device, and the final model is expressed as [Fitzhugh, 1955],

$$
\begin{aligned}
\frac{\partial u}{\partial t} &= u(u - \alpha)(1 - u) - v + I \\
\frac{\partial v}{\partial t} &= \varepsilon(u - \gamma v)
\end{aligned}
\tag{8}
$$

where u represents the 'fast variable' or potential, v represents the 'slow variable' which is a sodium gating variable or the recovery of potential, and I is the input current. The rest of the variables, denoted by α, γ and ε, are parameters that describe the resting state and dynamics of the system. The constant α represents a threshold for excitation of the membrane, ε accounts for the excitability and represents the coupling between the slow and fast phases, and γ is a shunting variable that describes the cell membrane, mainly the recovery growth of the potential. In our study we use this system to describe signal propagation, which we will discuss in later sections. If $I = 0$, the system is in a stable resting state, however if the value of I increases, for example to 0.4, it exhibits oscillatory activity [Varghese, 1995]. It can be easily seen that Fitzhugh's equations are much

simpler than those of Hodgkin and Huxley, and because of this it has been used widely to reproduce qualitative characteristics of electrical impulses along nerve and cardiac fibres. These characteristics include the existence of an excitation threshold and recovery period so both depolarization and repolarization can be modeled [Bray, 2002].

2.1.4 The Action Potential

The flow of ionic currents gives rise to change in the action potential in the heart, which in essence represents the activation wavefront. Subsequent mechanical contraction of the heart completes the cardiac cycle, as will be explained later in this chapter.

In a cardiac cell at resting potential there is an unequal intracellular and extracellular ionic composition, which results in a potential of approximately -70mV across the membrane. [Durrer, 1970]. The concentrations of sodium and chloride ions are high outside the cell relative to their intracellular, while the concentration of potassium is high inside the cell relative to its extracellular concentration. In fact, intracellular negativity results from the membrane's high permeability to potassium at rest that causes intracellular potassium to diffuse out of the cell. An action potential results when the membrane is depolarized, or in other words, the potential is raised by 15-20mv and there is a sudden increase in membrane permeability to sodium ions and decrease in potassium permeability. [Sachse, 2004]. Sodium channels open resulting in a large influx of sodium ions and the membrane potential increases to approximately 30mV, after which the gates are closed and repolarization begins. The four phases of a cardiac potential waveform is depicted in Figure 2-2. Phase 0 is the activation or depolarization phase described above. In Phase 1, the sodium channels are closed (i.e. the sodium permeability decreases), and a rapid yet

slight repolarization stage is seen. Phase 2 is considered the plateau phase, during which there is a steady depolarized transmembrane potential. During this stage, although the inward flow of ions is equal to the outward flow, the decreasing membrane potential again changes the membrane permeability so that repolarization starts, which we see in Phase 3. At this stage membrane potential decreases towards its original value, until it reaches the resting membrane potential in Phase 4, during which it will remain steady until the next action potential [Plonsey, 1982].

2.1.5 Excitable Media

Cardiac cells are classified as excitable media, meaning they are spatially distributed systems characterized by their ability to propagate signals without any damping. In the heart for example, traveling waves generate contractions to pump blood in a well ordered manner [Bub, 2000]. These kinds of systems have three main characteristics. First, they are seen as a group of elements that have diffusive type coupling to each other. This means that each element can send information to its neighbor; in cardiac muscle, this is done through the movement of ionic currents I_{Na} and I_K to neighboring cells. In addition, each cell of the excitable media must have a well defined resting state that is not sensitive to small perturbations. Then, if an impulse with strength greater than a specific threshold is met the cell can exit this defined state and return to it at a later time which is called the refractory point [Bub, 2000].

As the wave of activity propagates across cell membranes, diffusive coupling is initiated when an impulse over the threshold causes the cell to exit its resting state, which in turn causes the neighboring channels to be excited above threshold. Therefore, the current in

one cell results in a change in the potential of a neighboring cell. Since the ionic currents across the membrane depend on voltage, a nonlinear relationship between the membrane voltage and current is established [Guevara, 1991].

2.2 REACTION-DIFFUSION SYSTEMS

At the macroscopic level, the heart can be modeled such that the actual motion of ions is done through diffusion. In reaction-diffusion systems non-linear partial differential equations (PDEs) are used to describe excitation and propagation across excitable media. Modeling wave propagation in two dimensions is possible when equations are coupled to each other by diffusion, and it can essentially be described by Fick's law of diffusion. The change in the concentration of ions ϕ causes a change in the current density, resulting in a transmembrane voltage drop. The change in current density with respect to time is related to a diffusion coefficient denoted by D as follows,

$$\frac{\partial \phi}{\partial t} = \nabla \cdot \left(D(\phi, r) \nabla \phi(r, t) \right) \tag{9}$$

where D depends on the coordinate and/or concentration. We illustrate an example of a reaction-diffusion system in the following [Sachse, 2004],

$$\frac{\partial u_i}{\partial t} = f_i\left(u_1, \ldots, u_n\right) + \nabla \cdot \left(D \nabla u_i \right), \qquad i = 1, \ldots, n \tag{10}$$

where n is the dimension, or number of variables in the equation system. In (10) u_i is a state variable that represents cellular states; some examples include the transmembrane voltage, ionic concentrations, or ionic channel conductivity. A change in state variables is initiated by f_i which is seen as an excitation term, and in such active systems, once the

activator variable is initiated, it will continue to propagate. In (10) $\nabla \cdot \left(D\nabla u_i \right)$ represents a diffusion term, where D denotes a diffusion variable. Note that to simplify the notation the dependence on space and/or concentration is assumed implicitly. This diffusion term describes random motion of ions from areas of higher concentration to those of lower concentration, and as such can be viewed as averaged Brownian motion of particles.

The Fitzhugh-Nagumo equations seen in Section 2.1.3 are one of the common implementations of reaction-diffusion systems in simulating the propagation of waves in heart tissue,

$$\frac{\partial u}{\partial t} = D\nabla^2 u + u\left(u - \alpha \right)\left(1 - u \right) - v$$

$$\frac{\partial v}{\partial t} = \varepsilon\left(u - \gamma v \right)$$

(11)

where the $\nabla^2 u$ represents the spatial derivative. Note that in (11) we assume that the diffusion coefficient D is constant and that the medium is isotropic, however the expression can be extended to reflect a nonhomogeneous case or anisotropy in the medium which can be found in [Rogers, 1994]. Similar to (8), the state variables in (11) are u and v which represent the activator and the inhibitor respectively.

The cardiac cell can be seen as a current or electrical potential source because action currents flow into surrounding extracellular medium. Therefore the electrical impulse in the heart can be seen as a source of electromagnetic fields which we can measure on the torso surface. We want to be able to use these measurements in an inverse approach to image the electrical activity in the human body to the lowest level that we can feasibly observe.

2.3 CONDUCTION SYSTEM IN THE HEART

Electrical activity in the heart is initiated at the sino-atrial (SA) node, an impulse generating pacemaker located in the right atrium at the junction of the superior vena cava [Durrer, 1970]. A simplified depiction of the heart's conduction system is shown in Figure 2-3.

The tissue in the SA region is highly specialized such that they slowly depolarize, as opposed to remaining at rest, until a threshold is reached. Subsequently, self-excitation takes place, therefore initiating a heart beat through excitation of neighbors [Durrer, 1970]. The pulse propagates rapidly triggering a synchronous atrial contraction and the activity is conducted to the ventricles through the atrio-ventricular (AV) node, another area of specialized tissue, however with slow propagation velocity. The electrical wave is transmitted so slowly that this node, located just above the ventricles, can be considered as a delay line between the excitations in the two parts of the heart. When the impulse reaches the ventricles, it travels at a high velocity, approximately 2 m/s, through the bundles of His and a network of Purkinje fibres that subsequently convey it to sites within the left and right ventricles and septum [Holden, 1998]. Subsequent contraction of the ventricles (systole) followed by relaxation (diastole) completes the heart cycle [Guevara, 1991]. These waves of electrical activity spread throughout the heart muscle, causing rhythmic contractions. The waves of excitation in the heart travel at a velocity of approximately 0.5 m s^{-1} with amplitude defined by the action potential. We can therefore deduce that one wave can cover the entire area of the heart easily. In Figure 2-4 we illustrate action potentials recorded in different regions of the heart. Note that the

waveforms are displaced in time, reflecting the temporal sequence of propagation [Nerbonne, 2000]. If for any reason (i.e. medical condition) the heart rhythm is broken, the loss of synchronization can cause the atria and ventricles to contract at different times, thereby interrupting the pumping functions of the heart. Further, the action potential may be reduced and re-entrant propagation, in which the same wave of activity repeatedly passes through the same tissue, can occur [Holden, 1998]. The repeated excitation of the same heart tissue can interrupt the synchronous contractions that pump blood around the body.

2.4 ELECTROMAGNETIC FIELDS OUTSIDE A VOLUME CONDUCTOR

Electric currents in the body give rise to measurable electric and magnetic fields that can be measured using ECG/MCG sensors outside the torso. We are able to measure the electromagnetic fields outside arbitrary volume conductors including the torso, and we present expressions that relate these fields to the internal current sources discussed in Section 2.1. Derivations and proofs are presented in Appendix A.

2.4.1 Electric Potential within Volume Conductor

In electrophysiology it is understood that a conducting medium extends continuously, and if it is three dimensional it is called a volume conductor. As we noted in Section 2.2 we assume isotropic diffusion parameters. For the cases of anisotropy, the activation wavefront in the heart would take strange shapes which will affect the surface measurements to an unknown extent. We leave further investigation for future work.

First we examine a homogenous and isotropic volume conductor. In regions that contain no bioelectric sources current density $\mathbf{J}$ is linearly related to $\mathbf{E}$, the electric field intensity. We assume that the capacitative component of tissue impedance is negligible for small frequencies [Geselowitz, 1967]. Therefore in a region with no bioelectric sources and with conductivity σ, the current density is expressed,

$$\mathbf{J} = \sigma\mathbf{E} \qquad\qquad\qquad (12)$$

We also assume that electromagnetic wave effects can be neglected; that is while signals propagate the currents at any instant depend only on the sources at that instant, and are independent of any previous history. The electric field at each instant is therefore computed from the gradient of V, the electric scalar potential [Geselowitz, 1967],

$$\mathbf{E} = -\nabla V \qquad\qquad\qquad (13)$$

The current at any instant can be represented by a distribution of impressed current density $\mathbf{J}^i$, which arises when a conversion of energy from chemical to electric form occurs as part of the bioelectric activity of muscle cells [Malmivuo, 1995]. Therefore combining the active regions and those with no bioelectric sources, (12) is modified into

$$\mathbf{J} = \sigma\mathbf{E} + \mathbf{J}^i \qquad\qquad\qquad (14)$$

Since we deemed tissue capacitance as negligible, as sources vary the charges on any boundary interfaces redistribute themselves in a short time in response to any source change [Malmivuo, 1995] . Therefore using (13),

$$\nabla \cdot \mathbf{J} = 0$$
$$\nabla \cdot \mathbf{J}^i = \nabla \cdot \sigma \nabla V = \sigma \nabla^2 V \qquad\qquad (15)$$

Under these assumptions and conditions, a solution to the PDE in (15) is presented in [Geselowitz, 1967]. Let $R = r - r'$ define the distance between the observation point r and r', a point in the source region. Then the potential V due to a bioelectric source $\mathbf{J}^i$ that is within an infinite homogenous volume conductor is computed using the following expression,

$$4\pi\sigma V = \int_v \mathbf{J}^i \cdot \nabla\left(\frac{1}{R}\right)dv \tag{16}$$

where σ denotes the conductivity. For an inhomogeneous volume conductor with a volume source, instead of the assumed uniform medium, additional terms are needed to account for the different conductivities. In Figure 2-5 we assume the ellipses represent a cross-section model of the human torso, which we call volume G and is divided into M number of homogenous regions separated by boundaries S_p, $p = 1, \cdots, M$. Similar to the previous section, each region is isotropic with $\mathbf{J}^i = \sigma\mathbf{E}$ and is denoted G_p, $p = 1, \cdots, M$. At each boundary, the electrical potential and the normal component of the current density are continuous resulting in, [Geselowitz, 1967],

$$\begin{aligned} V'(S_p) &= V''(S_p) \\ \sigma'_p \nabla V'(S_p) \cdot \mathbf{n}_p &= \sigma''_p \nabla V''(S_p) \cdot \mathbf{n}_p \end{aligned} \tag{17}$$

where the prime and double prime notation represents each side of the boundary, and the normal direction is from single prime to double prime. Further in [Geselowitz, 1967], Green's theorem used such that the electric potential anywhere within the inhomogeneous volume conductor is given by,

$$4\pi\sigma V = \int_G \mathbf{J}^i \cdot \nabla\left(\frac{1}{R}\right)dv + \sum_p \int_{S_p} V\left(\sigma_p'' - \sigma_p'\right)\nabla\left(\frac{1}{R}\right)\cdot dS_p - \int_{S_p}\sigma V\nabla\left(\frac{1}{R}\right)\cdot dS_o \qquad (18)$$

where S_o denotes the boundary at the torso surface.

2.4.2 Magnetic Field on the Surface

The magnetic field outside a volume conductor is related to the internal current sources such that the current density $\mathbf{J}^i$ gives rise to a magnetic field $\mathbf{B}$ given by [Geselowitz, 1970],

$$\mathbf{B} = \left(\frac{\mu_o}{4\pi}\right)\int_G \mathbf{J}^i \times \nabla\left(\frac{1}{R}\right)dv \qquad (19)$$

where μ_o denotes permeability. Substituting (19) into (14) and with vector analysis, we obtain the following expression for the magnetic field outside an inhomogeneous volume conductor,

$$\mathbf{B} = \left(\frac{\mu_0}{4\pi}\right)\int_G \mathbf{J}^i \times \nabla\left(\frac{1}{R}\right)dv + \left(\frac{\mu_0}{4\pi}\right)\sum_p \int_{S_p}\left(\sigma_p' - \sigma_p''\right)V\nabla\left(\frac{1}{R}\right)\times dS_p \qquad (20)$$

In both (18) and (20) the second term on the right hand side represents the effect of inhomogeneities and external boundaries on the electric and magnetic fields. For derivations, please see Appendix A.
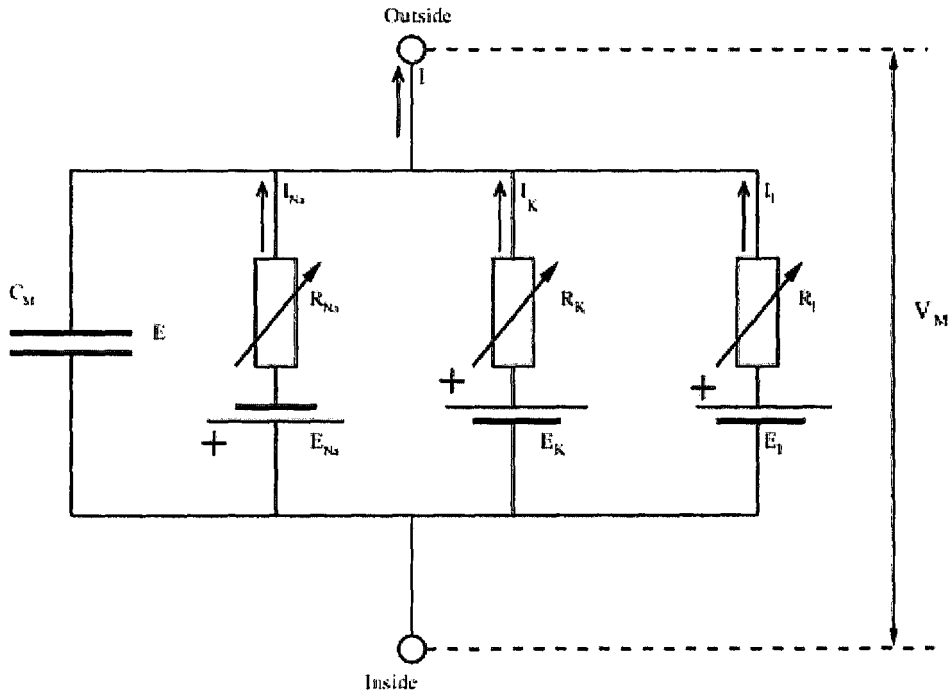
Figure 2 - 1: Cell Membrane as an Electrical Circuit
*[Hodgkin, 1952]
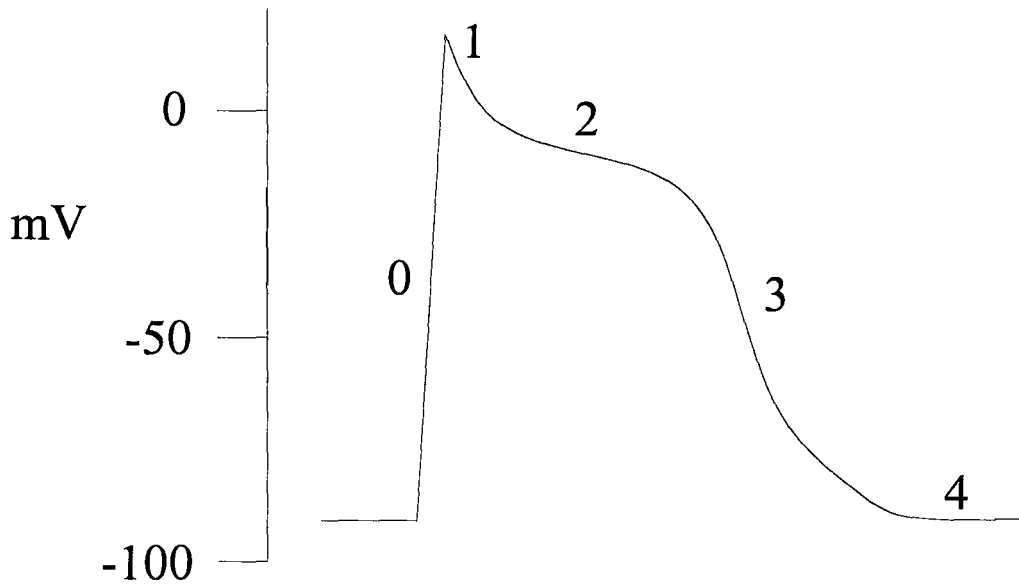
Figure 2 - 2: Cardiac Potential
* [Nerbonne, 2000]

Figure 2 - 3: Conduction System of the Heart
*http://www.mtsu.edu/~jshardo/bly2020/cardiovascular/heart.png
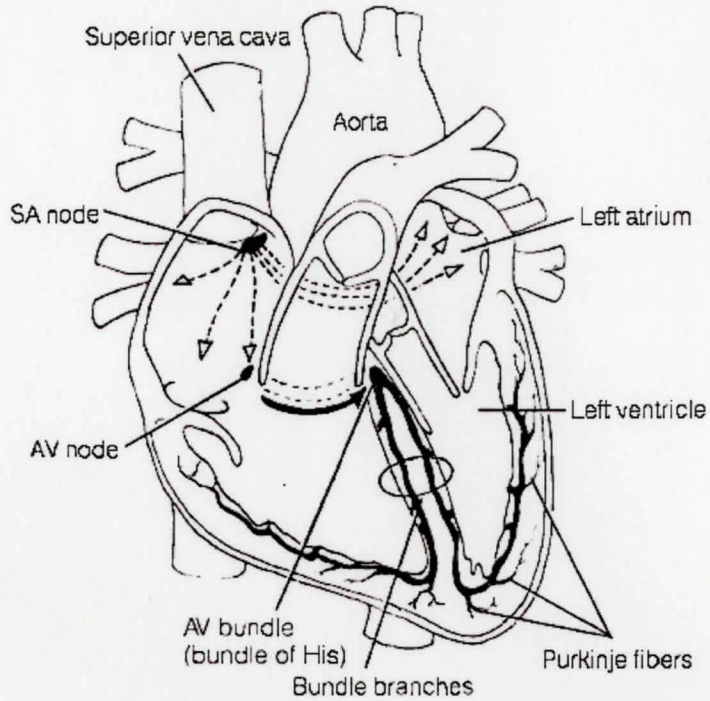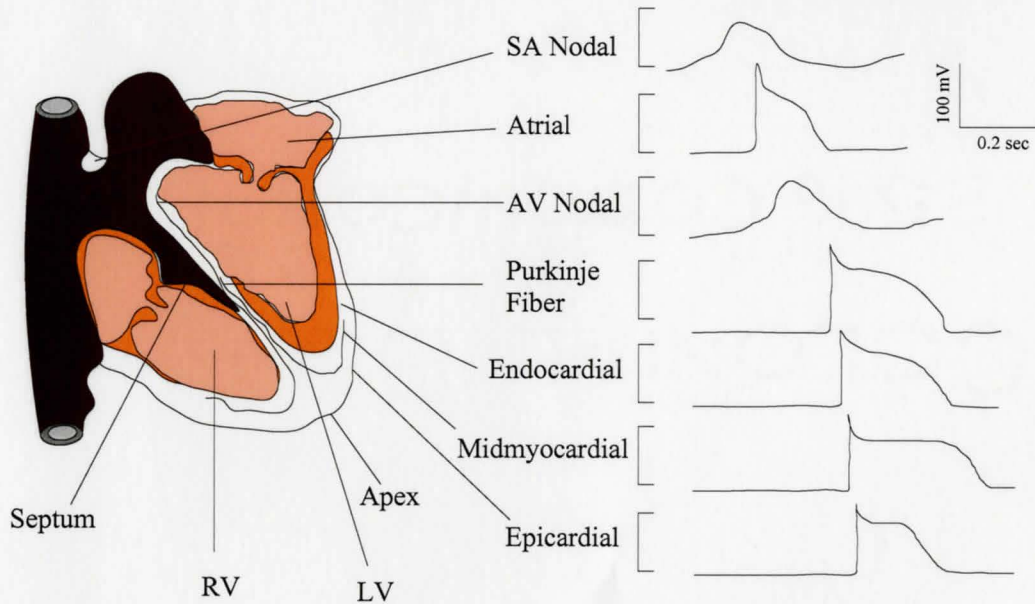
Figure 2 - 4: Action Potentials in the Heart
*[Nerbonne, 2000]
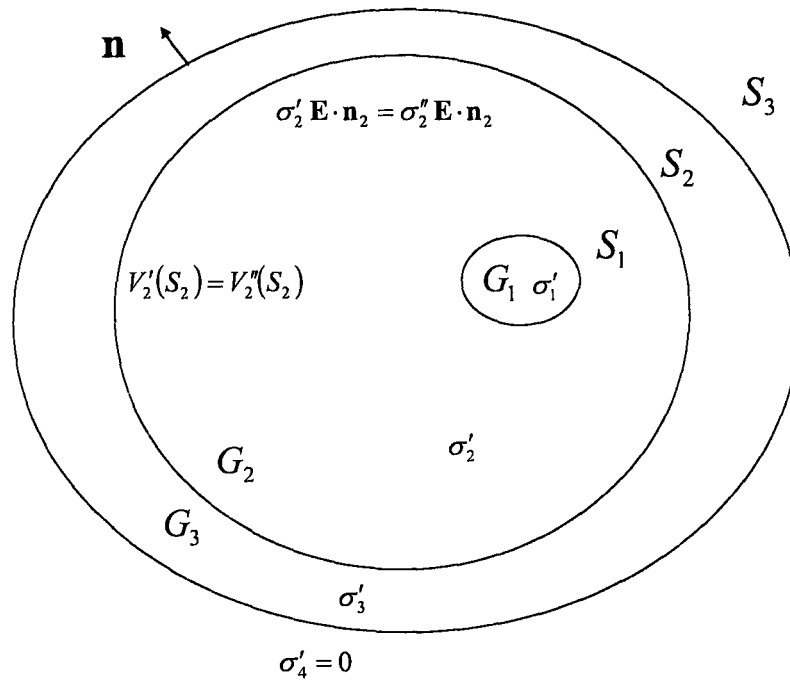
Figure 2 - 5: Inhomogeneous Model of the Torso

3   MATHEMATICAL MODEL

3.1 FINITE ELEMENT METHOD

The Finite Element Method (FEM) is a numerical technique that is commonly used in biomedical modeling because of its ability to solve PDEs over complex domains. [Jin, 2002]. Although it was originally developed for use with structural analysis in mechanical and civil engineering, over the last two decades it has become an important and extremely useful tool for solving electromagnetic problems. The method involves discretizing the domain into smaller parts, and the quality of this discretization is one aspect that is important for the effectiveness of any applications. This numerical technique for solving boundary value problems has many variations; however we present only a brief introductory summary.

Every boundary value problem can have a corresponding functional F, a variational expression whose minimum corresponds to the governing differential equation under the given boundary conditions. The following example shows the functional $F(\varphi)$ that corresponds to the diffusion equation we discussed in Chapter 2,

$$\frac{\partial \varphi}{\partial t} = D \frac{\partial^2 \varphi}{\partial x^2} \qquad (21)$$

$$F(\varphi) = 0.5 \int_0^1 \left(\frac{\partial \varphi}{\partial x} \right)^2 \partial x + \int_0^1 \frac{\partial \varphi}{\partial t} \varphi \, \partial x \qquad (22)$$

where D denotes the diffusion coefficient and φ represents the unknown potential. Trial functions are defined as functions for which the functional assumes a certain value, which we denote using $F(\widetilde{\varphi})$ [Jin, 2002]. Note that both φ and the trial functions are dependent on x and t however we deliberately omit them to reduce notation.

The concept of dividing the computational domain into elements is called 'meshing'. The number of elements determines many characteristics of the mesh, and will influence several factors of the solution, including accuracy and computational cost. In 2D problems, triangles are commonly used, while in 3D problems they are usually tetrahedral or cubes. If we use a tetrahedral, each element has four nodes, one at every vertex. Correspondingly, every vertex has a local node index, meaning a label that is local to the element. In addition, every element also has a global index, which is a label that identifies the element among others in the entire domain. To help identify the mesh, an array with the local and global indices is usually kept. We show an example in Figure 3-1, where the mesh consists of M number of elements, and $i = 1,2,3,4$ represents the label for each local node. The 'meshing' of the domain can be done using any of the meshing tools that exist.

Using the aforementioned discretization the problem's domain is divided into subdomains. For an arbitrary element there is an unknown value for the trial function $\widetilde{\varphi}^e$, which is expressed as an interpolation of the unknown nodal values,

$$\widetilde{\varphi}^e = \sum_{i=1}^{4} N_i^e \, \varphi_i^e \qquad\qquad (23)$$

where we use superscript e to denote the trial function for the eth element. Note that we omit the dependence on x and t again to reduce notational complexity. Further, $\widetilde{\varphi}_i^e$ is the value of $\widetilde{\varphi}^e$ at the ith node of the eth element, and N_i^e is the interpolating function. The functional F is then written in terms of the elemental subfunctionals,

$$F(\widetilde{\varphi}) = \sum_{e=1}^{M} F^e(\widetilde{\varphi}^e) \qquad (24)$$

Then an approximate solution can be computed by using defined boundary conditions and minimizing (24) given by [Jin, 2002],

$$\min(F(\widetilde{\varphi}) = \frac{\partial F(\widetilde{\varphi})}{\partial \varphi_i^e} = 0 \qquad (25)$$

In bioengineering applications most modeling is that of 3D objects, for which a corresponding mesh of tetrahedral shaped elements is the most common and we use it in this research study.

3.2 COMSOL MULTIPHYSICS SOFTWARE

Comsol Multiphysics (FEMLAB) is a finite element analysis and solver software package that is useful for various physics and engineering applications. The term multiphysics refers to coupled systems of PDEs, where information from one system is provided to the other thereby influencing its behaviour. For example as we saw in Chapter 2, in the generation of the action potential the movement of ions through the channels affects the membranes of neighbouring cells. Another example is electric and magnetic fields, which

were seen in (21) as a coupled system. The software is interactive, allowing the user to create a new model by drawing the geometry, and if needed, to enter a custom PDE. The user can also use specialized physics applications models that include predefined templates and user interfaces already set up with equations and variables for specific areas. Finally, it is also possible to load and modify an existing model in Comsol's Model Gallery. With respect to FE analysis, it is possible to create a model, and then manually create a mesh with specific parameters, for example, the size of the elements, or its general coarseness. In Figure 3-2 we illustrate an example of a fine tetrahedral mesh generated for an ellipse in Comsol. Comsol also offers an extensive interface to Matlab, a software that acts mainly as a numerical computing environment. The advantage of this interface is that every Comsol model has a FEM structure that can be exported to Matlab. The user is then free to incorporate any numerical techniques that exist in Matlab's functionality.

Our goal in this study is to develop an estimation model for the electrical properties of the signals generated in the heart. In this work, we use Comsol along with a model of the human torso and heart to simulate the electrical propagation, and then we use Matlab to modify and develop the estimation algorithm.

3.3 COMSOL MODEL

3.3.1 Electrical Signals of the Heart

The model named *Electrical Signals of the Heart* is part of Comsol's Model Gallery, and

was provided to the software company by [Fillipi, 2005]. It presents the geometry of the

heart as a prolate spheroid with two chambers, implemented in the general PDE mode.

For the heart, we use the physics described here but we apply them to a more realistic

mesh, described in the next section. We use this model, along with a realistic geometry of

the torso to conduct our simulations. In this model from Comsol, the PDEs correspond to

the Fitzhugh-Nagumo model as discussed in Chapter 2. However, this can be extended to

an arbitrary set of equations. The equations used for the diffusion of the electrical activity

are,

$$
\frac{\partial u_1}{\partial t} = D\nabla^2 u + (\alpha - u_1)(u_1 - 1)u_1 + (-u_2)
$$
$$
\frac{\partial u_2}{\partial t} = \varepsilon(\beta u_1 - \gamma u_2 - \delta)
$$

(26)

where u_1 represents the activator, which initiates the excitation, while u_2 represents the

gate variable, that acts as an inhibitor during the resting period of the heart cycle. The

constants, α and ε represent the threshold for excitation and excitability, respectively.

The rest state and dynamics of the system are represented by β, γ and δ. In these

equations, the diffusion coefficient in (11) is assumed to have the value 1. However in our

approach we treat D as an unknown parameter that can be estimated, along with the rest

of the constants described above. The initial condition that is already defined involves

the top two quadrants of the model. First, u_1 has an initial potential distribution so that one quadrant of the heart is at a constant elevated potential V_0, while the rest remains zero. As for the inhibitor variable u_2, the adjacent quadrant has another elevated value v_0, where $v_0 < V_0$. The initial conditions are expressed by the following,

$$u_1(0,x,y,z) = V_0\big((x+d)>0\big)\cdot\big((z+d)>0\big)$$
$$u_2(0,x,y,z) = v_0\big((-x+d)>0\big)\cdot\big((z+d)>0\big)$$

(27)

where d is a small displacement of 10^{-5} that is used to shift the potential of the main axes, making the model more physically realistic [Fillipi, 2005]. In Figure 3-3 we show the model of the heart in Comsol at initial condition. As a stand alone model, the boundary conditions are insulating assuming that no current is flowing into or out of the heart. We will compute the electromagnetic field which is in principle the signal that is measured by ECG/MCG sensor array, and as such we are interested in the value of the potential on the surface. Therefore when the heart model is inserted into the torso we use boundary conditions that reflect the continuity of the electric potential across the human body.

3.3.2 Torso Model

To model the human body using a realistic geometry we use a finite element mesh of the torso and heart, generously given by Dr. MacLeod, Department of Bioengineering, University of Utah. The coarse mesh is created using data from MRI scans, which defined the boundaries. We import the mesh into the Comsol software, under the quasistatics electric currents mode.

We choose the quasistatics for electromagnetic fields application mode because of our assumption in Chapter 2 that the propagation currents at any instant depend only on the sources at that instant. This means the process happens infinitely slowly compared to the propagation of the electromagnetic wave. For this model, we assume the torso is isotropic and homogenous and that the initial condition for the electric potential V, which is the dependent variable, is zero.

The imported data defines a coarse mesh, and we take the following steps to create a more refined one. We highlight our steps in Figures 3-4,5-8. We first try to allocate each element of the torso to defined subdomains, shown in Figure 3-4. However, this yields a mesh with coarse discretization and poor shape of elements which can introduce incorrect results, numerical errors, and greatly affect the execution time of the FEM computation. We instead choose a different method, where we start with defining and then refining the cardiac and torso surfaces first, shown in Figures 3-5, 3-6. Next, we create the torso shell and we join the entire composition, shown in Figure 3-7 and 3-8, respectively. In this way, we refine a new Comsol geometry for the torso model.

3.3.3 Forward Spatio-Temporal Model

To simulate the collection of electric potentials and magnetic field on the torso surface, we join both geometries. However, Comsol's prolate spheroid geometry is rather mismatched with the realistic torso mesh, and therefore, we use a realistic mesh of the heart geometry while keeping the physical model identical to that in Section 3.3.1. In an attempt to be anatomically correct, we place the heart in the mid left chest area of the body and we couple the two in the software; we show the entire geometry in Figure 3-9.

In Comsol, the advantage of the multiphysics feature is obvious as we implement both application modes discussed earlier; the general PDE mode for the heart, and the quasistatics for the torso. The initial conditions of the whole model are those of the heart component in the PDE mode, but slightly modified so that a small sphere is at an elevated potential rather than an entire quadrant as described earlier. Also, the electric potential that represents the dependent variable in the torso is initially zero. The boundary conditions determine the propagation of the signal from the source inside the heart, to the torso surface. To solve for the electromagnetic field, we enforce the continuity condition at the boundary between the heart and torso and we enforce the insulating condition at the torso surface. Then, running the simulation will represent the collection of the electromagnetic fields can be expressed by the following,

$$\mathbf{y}(\mathbf{r}, \mathbf{t}) = a(\mathbf{r}, \mathbf{t}, \theta^k) \qquad (28)$$

where θ is a vector that represents electrical properties of the activation at the SA node and properties of the heart. It is easily seen that (28) is a function of space and time, and we show the resulting models for the electrical potential, electric field, and magnetic field in Figures 3-10, 3-11, and 3-12, respectively. Then we export the Comsol model to Matlab, to be modified and to implement the measurement and estimation model.
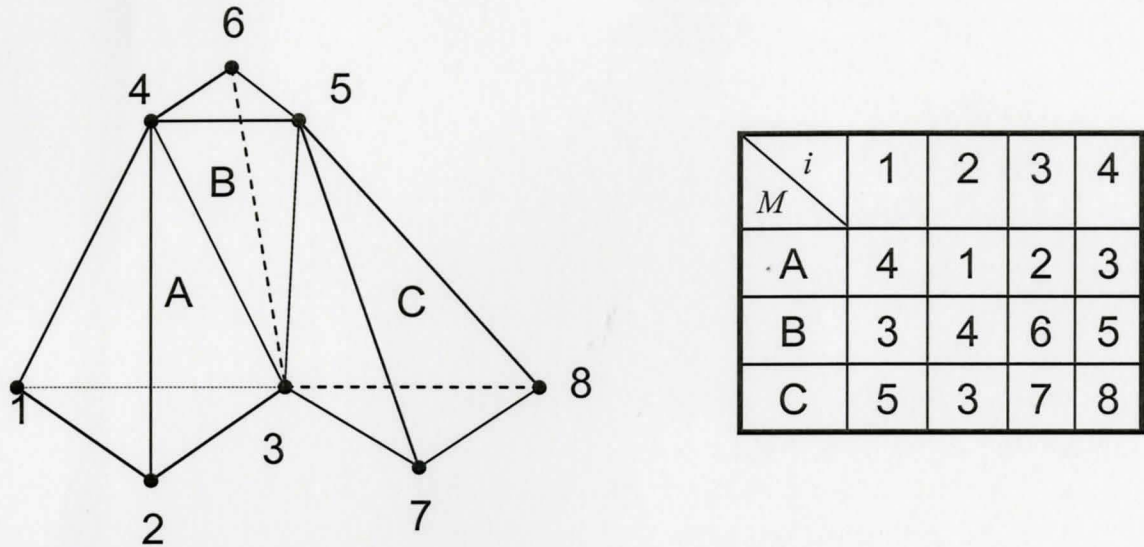
Figure 3 - 1: Global and Local Nodes, FEM

M \ i	1	2	3	4
A	4	1	2	3
B	3	4	6	5
C	5	3	7	8
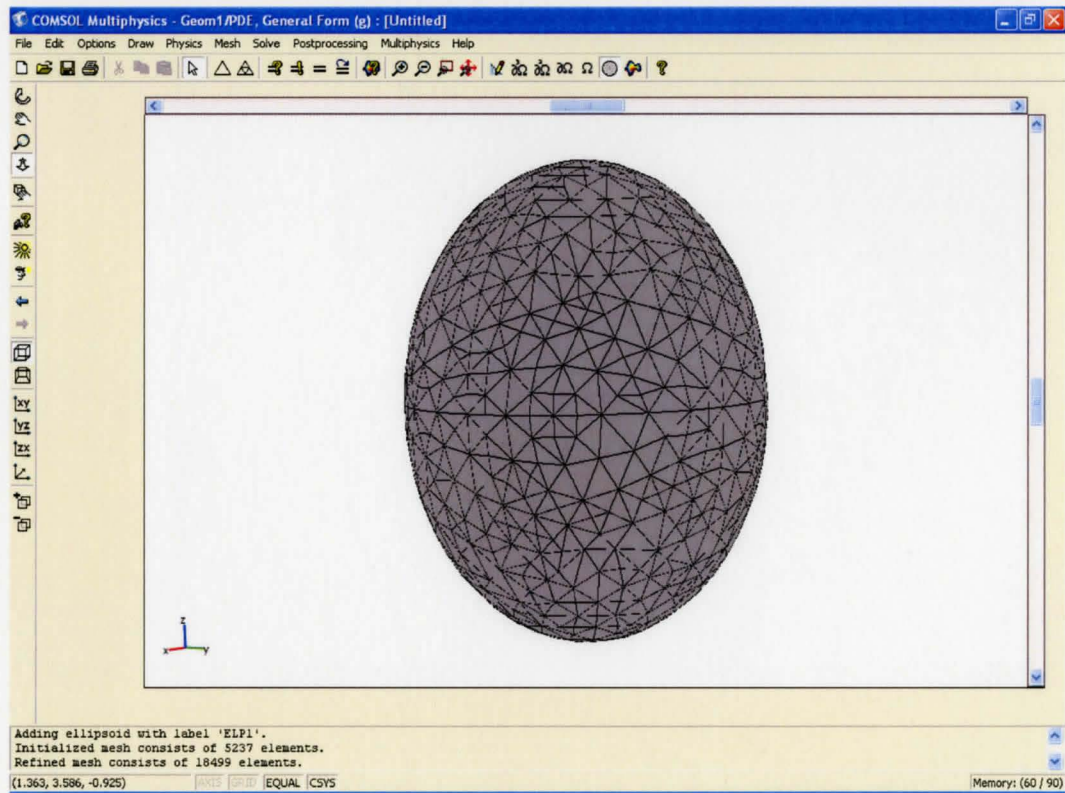
Figure 3 - 2: Comsol Sample Mesh
* [Fillippi, 2005]
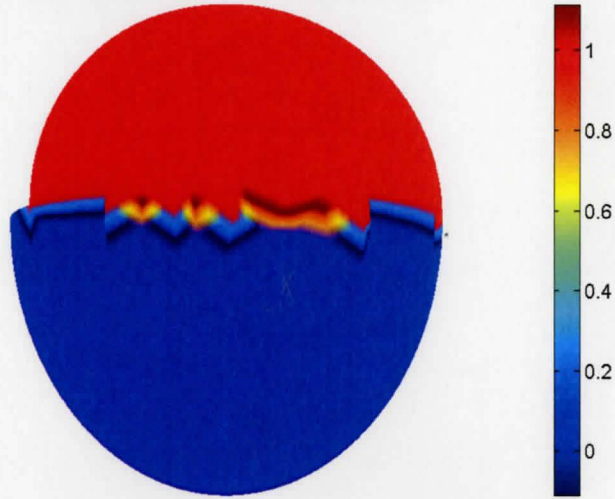
Figure 3 - 3: Comsol Electrical Signals of the Heart Model
*[Fillippi, 2005]

Method One

Step 1: Element = Domain
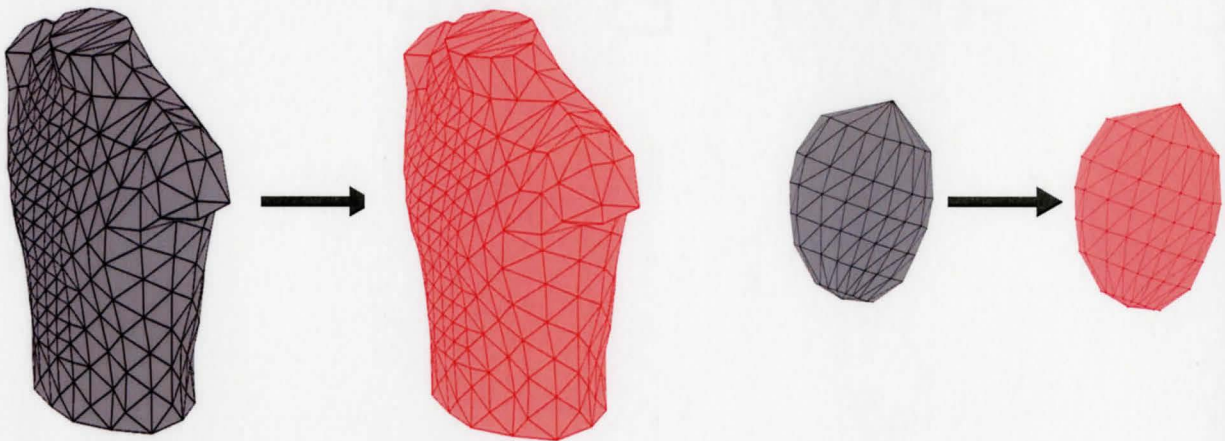
Figure 3 - 4: Method One - Refining Mesh
*[Attalla, 2006], [MacLeod, 2006]

Method Two

Step 1: Define surfaces
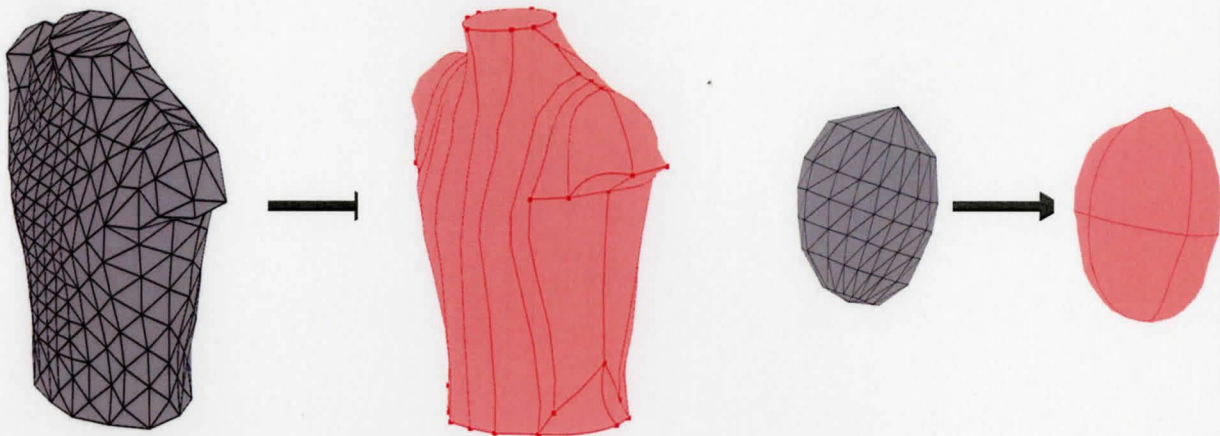
Figure 3 - 5: Method Two - Refining Mesh
*[Attalla, 2006], [MacLeod, 2006]

Step 2: Refine surfaces
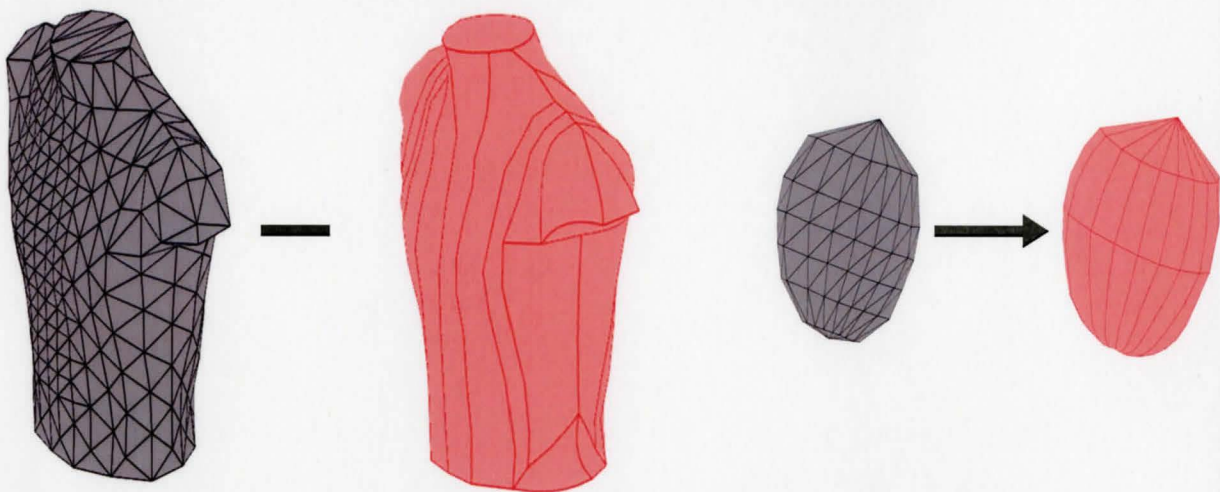
Figure 3 - 6: Step 2 - Refining Mesh
*[Attalla, 2006], [MacLeod, 2006]

Step 3: Creating the torso shell
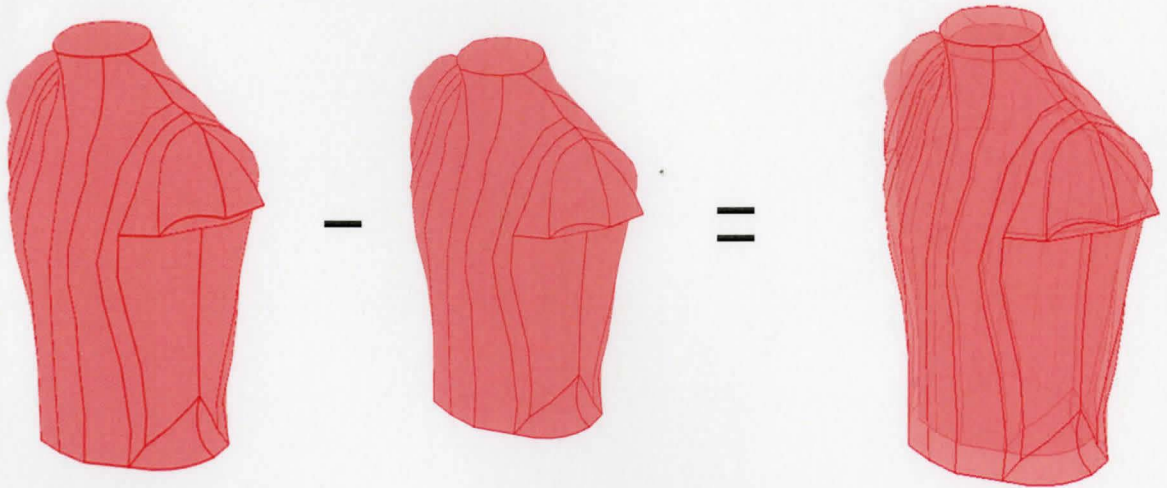
Figure 3 - 7: Step 3 - Refining Mesh
*[Attalla, 2006], [MacLeod, 2006]

Step 4: Join heart, torso, and the outer region
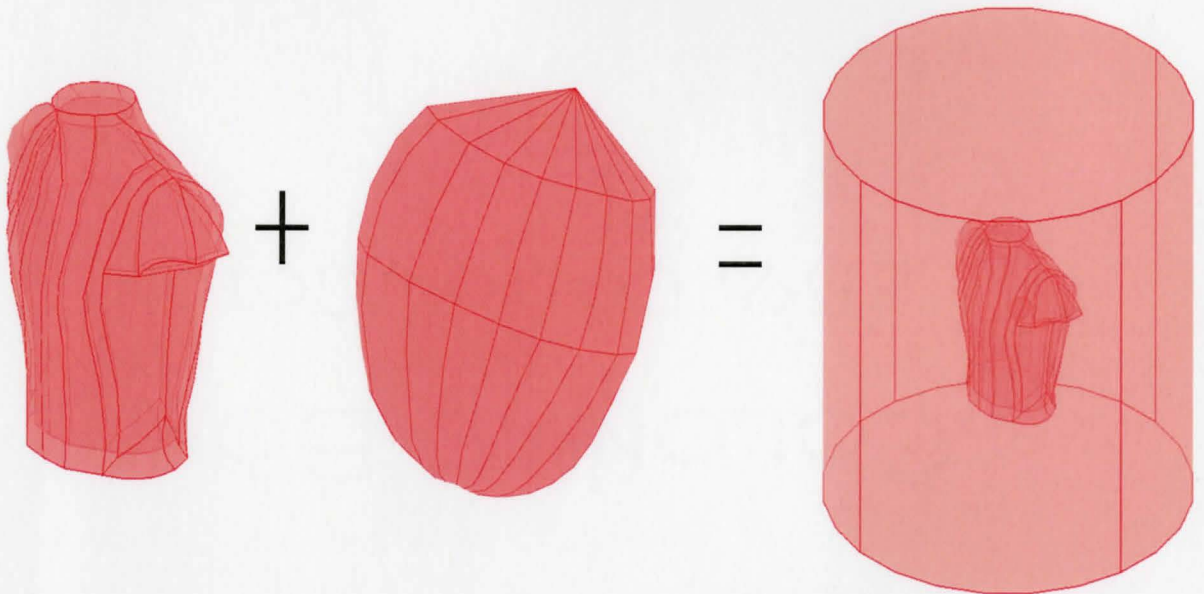
Figure 3 - 8: Step 4 - Refining Mesh
*[Attalla, 2006], [MacLeod, 2006]
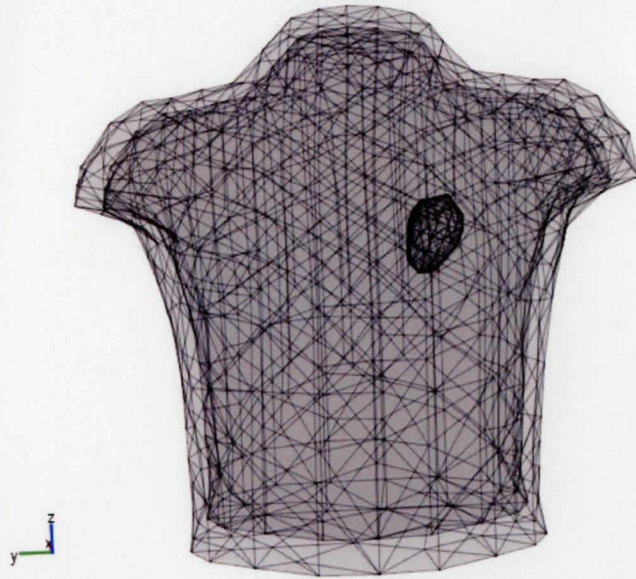
Figure 3 - 9: Comsol Torso with Heart Mesh
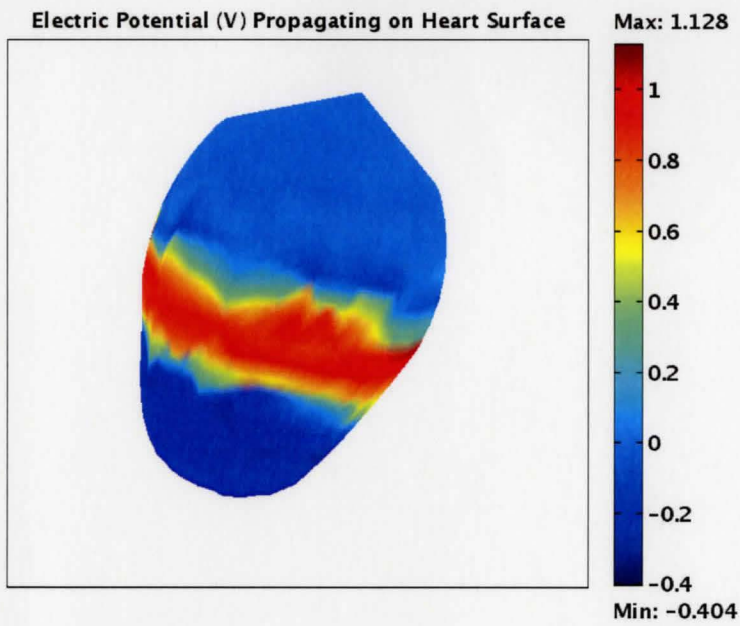
Figure 3 - 10: Electric Potential Propagating Through the Heart

Electric Field (V/m) on Torso Surface   Max: 8.00e-6
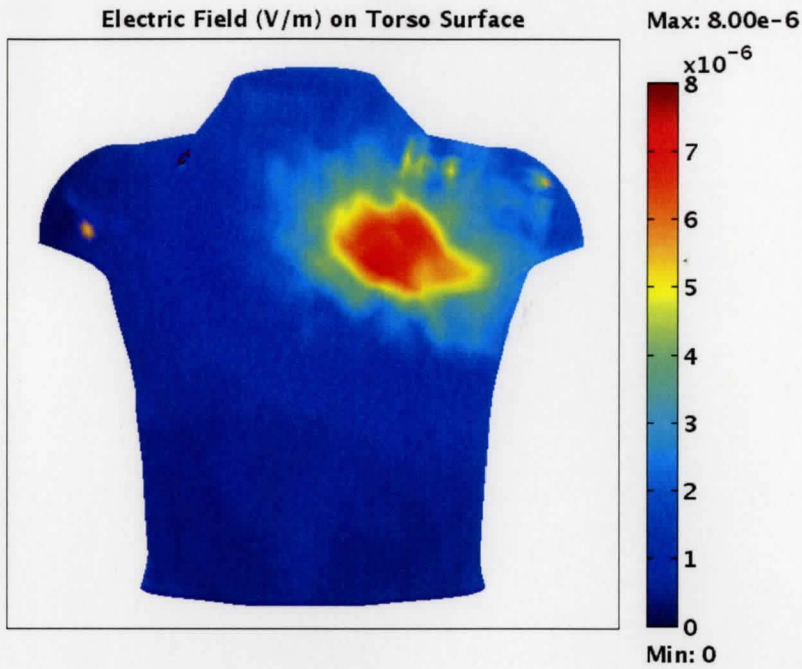
Figure 3 - 11: Electric Field on Torso Surface

Magnetic Field (T) on Torso Surface   Max: 1.00e-8
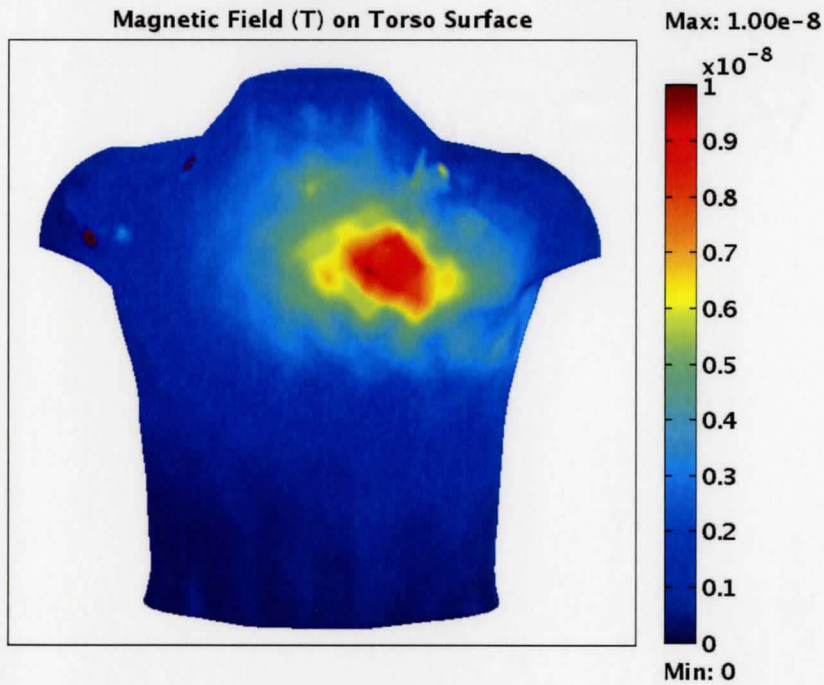
Figure 3 - 12: Magnetic Field on the Torso Surface

4   STATISTICAL MODELS

4.1 SENSOR ARRAYS

In electrocardiography ECG sensor arrays can be used to record the electrical activity of the heart on the torso surface. An ECG system usually consists of 32, 64, or 128 electrodes which are placed on the torso surface and use electro-chemical transducers to measure the electrical potential between various locations. This measurement technique is commonly used as part of a non-invasive and inexpensive diagnostic test for conditions such as arrhythmias and disorders in the activation sequence [Macfarlane, 1989].

Similar to electrocardiography, magnetocardiography currently extracts clinically relevant information from biosignals generated in the heart [Koch, 2001]. In a magnetocardiogram (MCG), the magnetic field is passively recorded as part of a completely noninvasive procedure without any contact to the body. Common MCG systems consist of 32 or 64 channels and a SQUID type magnetometer that measures small fields over the torso [Itozaki, 2003]. A typical MCG records information that is complementary to that given by an ECG, including the depolarization and repolarization of the action potential over time [Steinberg, 2005]. However, one major principle of MCG is that it is sensitive to tangential currents in the heart, whereas an ECG measures radial currents [Baule, 1970]. This is a significant difference because in a normal heart the main direction of the activation is radial, and therefore an MCG may show any illness-induced deviations from the normal direction of propagation with better accuracy than an ECG [Benjamin, 2005].

It is anticipated that future research will allow the MCG to contribute additional information and pave new diagnostic paths in a profoundly valuable way in clinical cardiology. For example, in fetal cardiology, during the last period of pregnancy the strong distortion of electrical signals within layers of tissue rules out surface ECG electrodes. However, fetal heart signals still create magnetic fields that can be measured with MCG. Nevertheless, at this point in time, various factors make ECG the more common technique [Koch, 2001]. One major reason is that biosignals in terms of magnitude are weaker than typical noise levels generated by power lines, or other emitters of electromagnetic interference. Hence MCG systems require powerful noise suppression techniques. One way is to place the system in a magnetically shielded room, which incurs heavy costs [Koch, 2001]. In this study we simulate measurements of both systems for the estimation of heart parameters.

In simulating ECG and MCG measurements we use 32 and 64 sensors, and to simplify the model uniform grids are used but they can be extended to non-uniform configurations. Their spatial distribution is asymmetrical about the heart's location and Figures 4-1, 4-2, and 4-3 illustrate the location of the sensors relative to the torso.

4.2 MEASUREMENT MODEL

Let $\mathbf{r}_i$ be the location of the ith sensor and $\mathbf{t}_{j,k}$ be the jth sampling time during the kth cycle

for period length T. Then the electromagnetic field obtained at the ith sensor can be given

by ,

$$\mathbf{y}(\mathbf{r}_i,\mathbf{t}_{j,k}) = \mathbf{a}(\mathbf{r}_i,\mathbf{t}_{j,k},\boldsymbol{\theta}^k) + \mathbf{e}(\mathbf{r}_i,\mathbf{t}_{j,k}),$$

(29)

for $i = 1,\cdots,m$, $\quad j = 1,\ldots,n$, $\quad k = 1,\ldots,c$

where,

$$\mathbf{t}_{j,k} = \mathbf{t}_j + \sum_{l=1}^{k-1} T_l \,, \quad \mathbf{t}_j = j\Delta T_s,$$

where m is the number of sensors, n is the number of sample points within a heart cycle,

and ΔT_s is the sampling time. Let $y_e(\mathbf{r}_i,\mathbf{t}_{j,k})$ represent the electric potential measurement

and let $\mathbf{y}_b(\mathbf{r}_i,\mathbf{t}_{j,k})$ be a 3 x 1 vector that represents the magnetic field measurement. Then

in (29) the independent data measurements collected every heart cycle can be given by,

$$\mathbf{y}(\mathbf{r}_i,\mathbf{t}_{j,k}) = \left[\mathbf{y}(\mathbf{r}_i,\mathbf{t}_{j,1})^T,\ldots,\mathbf{y}(\mathbf{r}_i,\mathbf{t}_{j,c})^T\right]^T$$

(30)

where we define our 4 x 1 measurement vector as,

$$\mathbf{y}(\mathbf{r}_i,\mathbf{t}_{j,k}) = \left[y_e(\mathbf{r}_i,\mathbf{t}_{j,k})^T,\mathbf{y}_b(\mathbf{r}_i,\mathbf{t}_{j,k})^T\right]^T$$

(31)

Also, $\mathbf{a}(\mathbf{r}_i,\mathbf{t}_{j,k},\boldsymbol{\theta}^k) = \left[\mathbf{a}(\mathbf{r}_i,\mathbf{t}_{j,k},\boldsymbol{\theta}^1)^T,\ldots,\mathbf{a}(\mathbf{r}_i,\mathbf{t}_{j,k},\boldsymbol{\theta}^c)^T\right]^T$ is a source-to-sensor array transfer

vector for c number of heart cycles, which can be computed at a particular location and

time using Geselowitz's equation,

$$\mathbf{B}(r,t)=\left(\frac{\mu_0}{4\pi}\right)\int_G \mathbf{J}^i(r,t)\times\nabla\left(\frac{1}{R}\right)dv+\left(\frac{\mu_0}{4\pi}\right)\sum_p \int_{S_p}(\sigma_p'-\sigma_p'')\,V(r,t)\,\nabla\left(\frac{1}{R}\right)\times d\mathbf{S}_p$$

where $R=r-r'$ is the distance between the observation point r and r', a point in the source region. We use θ^k to represent a (potentially) unknown vector of heart electrical parameters such as excitability or conductivity, which are the coefficients of the diffusion model as explained in Chapter 2. These parameters affect the current which in turn affects the impressed current density $\mathbf{J}^i$ and shapes the electrical potential and magnetic field. Therefore, although there is no explicit analytical expression, V and $\mathbf{B}$ are uniquely determined. In (29) we use $\mathbf{e}(\mathbf{r}_i,\mathbf{t}_{j,k})$ to denote the error residuals which are due to measurement and modeling noises.

Note that the subscript k is used to denote that the electrical parameters can potentially change from cycle to cycle. A parameter that changes throughout the cycle is labeled as 'short-scaled time varying' while a 'long-scale time varying' parameter only changes at the beginning of every cycle. A parameter that is constant throughout the activation process is time invariant and will remain named as such. Let $\theta=[\theta_1;\cdots,\theta_r]^T$ denote a vector of deterministic time invariant (DTI) heart parameters. Then (29) can be re-written such that the k superscript on the parameter is dropped, as follows,

$$\mathbf{y}(\mathbf{r}_i,\mathbf{t}_{j,k})=\mathbf{a}(\mathbf{r}_i,\mathbf{t}_{j,k},\theta)+\mathbf{e}(\mathbf{r}_i,\mathbf{t}_{j,k}) \tag{32}$$

with the exception that in the stochastic case the parameter values at different times in the heart cycle may be random with probability distribution function (PDF) $\theta^k\sim N\!\left(\mu^*,\sigma^{2^*}\right)$, for unknown mean and variance. In the remainder of the thesis we will consider two

cases; one is the deterministic case in which the parameters are completely unknown. The second, often referred to as the stochastic case, assumes that certain prior knowledge of the electrical parameters is available. Note that in biomedical engineering this prior knowledge can often be obtained using either in-vitro studies or by the results of the previous estimation procedures on previous patients. Therefore, a relatively good guess for the distribution of the parameters may be available. In parameter estimation the PDF of the data measurements can be vital to estimation algorithms. In the next section, we will discuss the corresponding statistical models of the measurement data vector.

4.3 PARAMETRIC MODEL

In this section we discuss parameter estimation for the following noise models:

 i.   Homogeneous Spatially Uncorrelated

 ii.   Non-Homogenous Spatially Uncorrelated

 iii. Spatially Correlated

We develop the expressions for the PDF, f, of $\mathbf{y}(\mathbf{r}_i, \mathbf{t}_{j,k})$ for each model.

4.3.1 DTI Parameters - Homogeneous Spatially Uncorrelated Noise

We assume Gaussian noise that is uncorrelated in space and time, from cycle to cycle, and with constant variance from sensor to sensor. For a deterministic time invariant parameter, recall (32), for $\mathbf{e}(\mathbf{r}_i, \mathbf{t}_{j,k}) \sim N(0, \sigma^2)$, and covariance R expressed,

$$R = \text{cov}\left(\mathbf{e}(\mathbf{r}_i, \mathbf{t}_{j,k}), \mathbf{e}(\mathbf{r}_{i'}, \mathbf{t}_{j',k'})\right) = \text{E}\left(\left(\mathbf{e}(\mathbf{r}_i, \mathbf{t}_{j,k}) - \mu_e\right)\left(\mathbf{e}(\mathbf{r}_{i'}, \mathbf{t}_{j',k'}) - \mu_{e'}\right)^T\right)$$

$$= \sigma^2 \delta(i - i') \delta(j - j') \delta(k - k')$$
(33)

where E denotes the expectation operator, μ_e is the zero mean of the noise vector, and where δ is the Kronecker delta defined as ,

$$\delta(j - j') = \begin{cases} 1, & j = j' \\ 0, & j \neq j' \end{cases}, \quad \delta(k - k') = \begin{cases} 1, & k = k' \\ 0, & k \neq k' \end{cases}$$
(34)

Since,

$$\mu_y = \text{E}\left(\mathbf{y}(\mathbf{r}_i, \mathbf{t}_{j,k})\right) = \text{E}\left(\mathbf{a}(\mathbf{r}_i, \mathbf{t}_{j,k}, \boldsymbol{\theta})\right) + 0 = \mathbf{a}(\mathbf{r}_i, \mathbf{t}_{j,k}, \boldsymbol{\theta})$$
(35)

where μ_y is the mean of the measurement vector , the distribution of $\mathbf{y}(\mathbf{r}_i, \mathbf{t}_{j,k})$, is therefore,

$$\mathbf{y}(\mathbf{r}_i, \mathbf{t}_{j,k}) \sim N\left(\mathbf{a}(\mathbf{r}_i, \mathbf{t}_{j,k}, \boldsymbol{\theta}), R\right)$$
(36)

4.3.2 DTI Parameters - Non-Homogenous Spatially Uncorrelated Noise

We assume Gaussian noise that is uncorrelated in space, time, and from one cycle to another. However the variance changes from one sensor to another and it is further assumed that it does not change from cycle to cycle. The mean $\mu_y = \mathbf{a}(\mathbf{r}_i, \mathbf{t}_{j,k}, \boldsymbol{\theta})$ remains unchanged from Section 4.3.1.1 and the covariance Q is written to reflect this,

$$Q = \text{cov}\left(\mathbf{y}(\mathbf{r}_i, \mathbf{t}_{j,k}), \mathbf{y}(\mathbf{r}_{i'}, \mathbf{t}_{j',k'})\right) = diag\{\sigma_1^2, \sigma_2^2, \cdots, \sigma_m^2\}\delta(j - j')$$
(37)

for maximum m number of sensors. Therefore,

$$\mathbf{y}\!\left(\mathbf{r}_i, \mathbf{t}_{j,k}\right) \sim N\!\left(\mathbf{a}\!\left(\mathbf{r}_i, \mathbf{t}_{j,k}, \mathbf{\theta}\right), Q\right) \tag{38}$$

4.3.3 DTI Parameters - Spatially Correlated Noise

We assume Gaussian noise that is uncorrelated in time, and from one heart cycle to another. However, there exists spatial correlation. This model can also be switched so that there is temporal correlation and in that case, the same expressions that follow would apply. To reflect the spatial covariance in the noise, (37) is rewritten to solve for the new covariance,

$$M = \mathrm{cov}\!\left(\mathbf{y}\!\left(\mathbf{r}_i, \mathbf{t}_{j,k}\right), \mathbf{y}\!\left(\mathbf{r}_{i'}, \mathbf{t}_{j',k'}\right)\right) = \Sigma_{i-i'}\,\delta\!\left(j - j'\right)\delta\!\left(k - k'\right) \tag{39}$$

where $\Sigma_{i-i'}$ denotes the spatial correlation matrix. Finally, in this case,

$$\mathbf{y}\!\left(\mathbf{r}_i, \mathbf{t}_{j,k}\right) \sim N\!\left(\mathbf{a}\!\left(\mathbf{r}_i, \mathbf{t}_{j,k}, \mathbf{\theta}\right), M\right) \tag{40}$$

It is easily seen that the variance of $\mathbf{y}\!\left(\mathbf{r}_i, \mathbf{t}_{j,k}\right)$ thus far is the variance of the noise and we conclude that it is independent of the type of parameter. Therefore, for the rest of this chapter, expressions (33), (37), and (39) will be used as the definitions of the variance for the three noise models listed in Section 4.2.

4.3.4 DTV Parameters

The parameters are time varying and therefore, the mean μ_y will change from one heart cycle to another. Therefore, the distribution of the measurement vector is rewritten to reflect that the mean is now a function of the heart cycle. For the three noise models respectively,

$$\mathbf{y}(\mathbf{r}_i, \mathbf{t}_{j,k}) \sim N\big(\mathbf{a}(\mathbf{r}_i, \mathbf{t}_{j,k}, \mathbf{\theta}^k), R\big) \tag{41}$$

$$\mathbf{y}(\mathbf{r}_i, \mathbf{t}_{j,k}) \sim N\big(\mathbf{a}(\mathbf{r}_i, \mathbf{t}_{j,k}, \mathbf{\theta}^k), Q\big) \tag{42}$$

$$\mathbf{y}(\mathbf{r}_i, \mathbf{t}_{j,k}) \sim N\big(\mathbf{a}(\mathbf{r}_i, \mathbf{t}_{j,k}, \mathbf{\theta}^k), M\big) \tag{43}$$

where R,Q, and M are the expressions for the covariance of $\mathbf{y}(\mathbf{r}_i, \mathbf{t}_{j,k})$ as we defined in Sections 4.3.1, 4.3.2,and 4.3.3, respectively.

4.3.5 STO Parameters

We assume that the heart parameters in (28) are normal random variables that are 'long-scale' time varying as defined in Section 4.1 where $\mathbf{\theta}^k \sim N\big(\mu^*, \sigma^{2^*}\big)$ for unknown μ^* and σ^{2^*}. In this case, the assumption that the measurement vector $\mathbf{y}(\mathbf{r}_i, \mathbf{t}_{j,k})$ is Gaussian no longer holds because the distribution of the transfer vector $\mathbf{a}(\mathbf{r}_i, \mathbf{t}_{j,k}, \mathbf{\theta}^k)$ is unknown due to the non-linear function of the stochastic parameters. Assuming that $\mathbf{a}(\mathbf{r}_i, \mathbf{t}_{j,k}, \mathbf{\theta}^k)$ and $\mathbf{e}(\mathbf{r}_i, \mathbf{t}_{j,k})$ are independent random variables, the PDF of $\mathbf{y}(\mathbf{r}_i, \mathbf{t}_{j,k})$, as derived in Appendix B, is written,

$$f_Y(y) = f_z\big(\mathbf{y}(\mathbf{r}_i, \mathbf{t}_{j,k}) - \mathbf{e}(\mathbf{r}_i, \mathbf{t}_{j,k})\big) \otimes f_e\big(\mathbf{e}(\mathbf{r}_i, \mathbf{t}_{j,k})\big) \tag{44}$$

where $z = \mathbf{a}(\mathbf{r}_i, \mathbf{t}_{j,k}, \mathbf{\theta}^k)$ and $\otimes$ represents the convolution operator. Further, the mean of $\mathbf{y}(\mathbf{r}_i, \mathbf{t}_{j,k})$ is defined, [Papoulis, 2000],

$$\upsilon_y = \mathrm{E}\big(\mathbf{y}(\mathbf{r}_i, \mathbf{t}_{j,k})\big) = \mathrm{E}\big(\mathbf{a}(\mathbf{r}_i, \mathbf{t}_{j,k}, \mathbf{\theta}^k)\big) + \mathrm{E}\big(\mathbf{e}(\mathbf{r}_i, \mathbf{t}_{j,k})\big) = \mathrm{E}\big(\mathbf{a}(\mathbf{r}_i, \mathbf{t}_{j,k}, \mathbf{\theta}^k)\big) \tag{45}$$

Then, by definition of the expected value,

$$\upsilon_y = \int\limits_{-\infty}^{\infty} \mathbf{a}\big(\mathbf{r}_i, \mathbf{t}_{j,k}, \boldsymbol{\theta}^k\big) f_{\boldsymbol{\theta}}(\boldsymbol{\theta}) d\theta \qquad (46)$$

As claimed in the introduction of this chapter, the statistical properties of the heart parameters are important, which for example can be seen in (46) as the PDF of these variables directly influences the mean of the measurement vector.

The covariance is derived,

$$\begin{aligned}
\text{cov}\big(\mathbf{y}(\mathbf{r}_i, \mathbf{t}_{j,k}), \mathbf{y}(\mathbf{r}_{i'}, \mathbf{t}_{j',k'})\big) &= \text{E}\Big(\big(\mathbf{y}(\mathbf{r}_i, \mathbf{t}_{j,k}) - \upsilon_y\big)\big(\mathbf{y}(\mathbf{r}_{i'}, \mathbf{t}_{j',k'}) - \upsilon_{y'}\big)^T\Big) \\[2mm]
&= \text{E}\big(\mathbf{y}(\mathbf{r}_i, \mathbf{t}_{j,k}) \cdot \mathbf{y}(\mathbf{r}_{i'}, \mathbf{t}_{j',k'})^T\big) - \big(\upsilon_y \cdot \upsilon_{y'}^T\big) \\[2mm]
&= \text{E}\big(\mathbf{a}(\mathbf{r}_i, \mathbf{t}_{j,k}, \boldsymbol{\theta}^k) \cdot \mathbf{a}(\mathbf{r}_{i'}, \mathbf{t}_{j',k'}, \boldsymbol{\theta}^k)^T\big) + \text{E}\big(\mathbf{a}(\mathbf{r}_i, \mathbf{t}_{j,k}, \boldsymbol{\theta}^k) \cdot \mathbf{e}(\mathbf{r}_i, \mathbf{t}_{j,k})\big) + \\[2mm]
&\quad \text{E}\big(\mathbf{a}(\mathbf{r}_{i'}, \mathbf{t}_{j',k'}, \boldsymbol{\theta}^k) \cdot \mathbf{e}(\mathbf{r}_{i'}, \mathbf{t}_{j',k'})^T\big) + \text{E}\big(\mathbf{e}(\mathbf{r}_i, \mathbf{t}_{j,k}) \cdot \mathbf{e}(\mathbf{r}_{i'}, \mathbf{t}_{j',k'})^T\big) - \big(\upsilon_y \cdot \upsilon_{y'}^T\big)
\end{aligned}$$

$$(47)$$

The independence of $\mathbf{a}(\mathbf{r}_{i'}, \mathbf{t}_{j',k'}, \boldsymbol{\theta}^k)$ and $\mathbf{e}(\mathbf{r}_{i'}, \mathbf{t}_{j',k'})$ allows the cancellation of the middle terms because the expected value of the noise is zero. This yields,

$$\begin{aligned}
\text{cov}\big(\mathbf{y}(\mathbf{r}_i, \mathbf{t}_{j,k}), \mathbf{y}(\mathbf{r}_{i'}, \mathbf{t}_{j',k'})\big) &= \text{E}\big(\mathbf{a}(\mathbf{r}_i, \mathbf{t}_{j,k}, \boldsymbol{\theta}^k) \cdot \mathbf{a}(\mathbf{r}_{i'}, \mathbf{t}_{j',k'}, \boldsymbol{\theta}^k)^T\big) + \\[2mm]
&\quad \text{E}\big(\mathbf{e}(\mathbf{r}_i, \mathbf{t}_{j,k}) \cdot \mathbf{e}(\mathbf{r}_{i'}, \mathbf{t}_{j',k'})^T\big) - \big(\upsilon_y \cdot \upsilon_{y'}^T\big)
\end{aligned}$$

$$(48)$$

where $\upsilon_{y'}$ is the expected value of $\mathbf{y}(\mathbf{r}_{i'}, \mathbf{t}_{j',k'})$ and $E\left(\mathbf{e}_{i,j,k}(t) \cdot \mathbf{e}_{i',j',k'}(t)^T\right)$ is the variance of the noise. Therefore the PDF of $\mathbf{y}(\mathbf{r}_i, \mathbf{t}_{j,k})$ is defined by (44), with mean υ_y. The covariance corresponds to (48) where the variance is defined for each noise model as in Section 4.3 respectively,

$$\mathrm{cov}\left(\mathbf{y}(\mathbf{r}_i, \mathbf{t}_{j,k}), \mathbf{y}(\mathbf{r}_{i'}, \mathbf{t}_{j',k'})\right) = E\left(\mathbf{a}(\mathbf{r}_i, \mathbf{t}_{j,k}, \boldsymbol{\theta}^k) \cdot \mathbf{a}(\mathbf{r}_{i'}, \mathbf{t}_{j',k'}, \boldsymbol{\theta}^k)^T\right) + R - \left(\upsilon_y \cdot \upsilon_{y'}^T\right) \qquad (49)$$

$$\mathrm{cov}\left(\mathbf{y}(\mathbf{r}_i, \mathbf{t}_{j,k}), \mathbf{y}(\mathbf{r}_{i'}, \mathbf{t}_{j',k'})\right) = E\left(\mathbf{a}(\mathbf{r}_i, \mathbf{t}_{j,k}, \boldsymbol{\theta}^k) \cdot \mathbf{a}(\mathbf{r}_{i'}, \mathbf{t}_{j',k'}, \boldsymbol{\theta}^k)^T\right) + Q - \left(\upsilon_y \cdot \upsilon_{y'}^T\right) \qquad (50)$$

$$\mathrm{cov}\left(\mathbf{y}(\mathbf{r}_i, \mathbf{t}_{j,k}), \mathbf{y}(\mathbf{r}_{i'}, \mathbf{t}_{j',k'})\right) = E\left(\mathbf{a}(\mathbf{r}_i, \mathbf{t}_{j,k}, \boldsymbol{\theta}^k) \cdot \mathbf{a}(\mathbf{r}_{i'}, \mathbf{t}_{j',k'}, \boldsymbol{\theta}^k)^T\right) + M - \left(\upsilon_y \cdot \upsilon_{y'}^T\right) \qquad (51)$$

4.4 PARAMETER ESTIMATION

To investigate the feasibility of using ECG/MCG measurements to estimate the heart parameters it is possible to use numerous estimation techniques and algorithms. They all have advantages and disadvantages including accuracy, efficiency and computational cost. We choose the non-linear least squares (LS) and the maximum likelihood estimation (MLE) methods. In LS there are no requirements for the assumptions of noise making it ideal to be used as a benchmark for comparison with MLE. Further, the MLE is asymptotically efficient, meaning it reaches optimal performance as the number of samples tends to infinity.

4.4.1 Least Squares

The main idea behind LS estimation is to fit an analytical model to the measurement vector by minimizing the distance between them. Recall that the simulation measurements observed at the sensors are expressed $\mathbf{y}(\mathbf{r}_i, \mathbf{t}_{j,k}) = \mathbf{a}(\mathbf{r}_i, \mathbf{t}_{j,k}, \theta^k) + \mathbf{e}(\mathbf{r}_i, \mathbf{t}_{j,k})$, for θ^k, a vector that represents the unknown heart parameters.

Let $\hat{\mathbf{y}}(\mathbf{r}_i, \mathbf{t}_{j,k}) = \hat{\mathbf{a}}(\mathbf{r}_i, \mathbf{t}_{j,k}, \theta^k)$ represent the analytical model for the propagation of electrical signals in the heart, as seen in Section 3.3.3. The LS estimate is that $\hat{\theta}^k$ which will minimize the sum of the squares of the residual $\hat{\mathbf{R}}$,

$$\hat{\theta}_{LS} = \min \hat{\mathbf{R}} = \left\| \mathbf{y}(\mathbf{r}_i, \mathbf{t}_{j,k}) - \hat{\mathbf{a}}(\mathbf{r}_i, \mathbf{t}_{j,k}, \theta^k) \right\|_2^2 \qquad (52)$$

Note that LS does not take into account the noise distribution. To solve (52), we take the partial derivative with respect to the parameter we wish to estimate and equate it to zero.

$$\frac{\partial}{\partial \theta_r} \left[\sum_{k=1}^{c} \left(\mathbf{y}(\mathbf{r}_i, \mathbf{t}_{j,k}) - \hat{\mathbf{a}}(\mathbf{r}_i, \mathbf{t}_{j,k}, \hat{\theta}_{LS}^{\ k}) \right)^2 \right] = 0 \qquad (53)$$

$$-2 \sum_{k=1}^{c} \left(\mathbf{y}(\mathbf{r}_i, \mathbf{t}_{j,k}) - \hat{\mathbf{a}}(\mathbf{r}_i, \mathbf{t}_{j,k}, \hat{\theta}_{LS}^{\ k}) \right) \cdot \frac{\partial}{\partial \theta_r} \left(\hat{\mathbf{a}}(\mathbf{r}_i, \mathbf{t}_{j,k}, \hat{\theta}_{LS}^{\ k}) \right) = 0 \qquad (54)$$

To solve (54) an estimation algorithm is used with an initial guess for $\hat{\theta}_{LS}^{\ k}$ and an optimization routine which continues until the minimum value for the residual is achieved. The 2-norm squared difference is computed at each step; therefore it is easy to understand that the speed and accuracy of the algorithm greatly depends on how close the initial estimate is to the true value of the parameter. Various search algorithms exist for

optimization; however the Nelder-Mead method, [Avriel, 2003], which is discussed in Chapter 6, is used in this study.

4.4.2 Maximum Likelihood Estimation

The maximum likelihood estimation (MLE) method finds the parameter that provides the best fit with the assumed PDF of the measurement vector. In this section, to simplify the notation we let,

$$\left[\mathbf{y}\left(\mathbf{r}_i,\mathbf{t}_{j,1}\right)^T, \mathbf{y}\left(\mathbf{r}_i,\mathbf{t}_{j,k}\right)^T, \ldots, \mathbf{y}\left(\mathbf{r}_i,\mathbf{t}_{j,c}\right)^T \right]^T = \left[\mathbf{y}_1^T, \mathbf{y}_k^T, \ldots, \mathbf{y}_c^T \right]^T \tag{55}$$

so that the spatial-temporal dependence is assumed implicitly, and the subscript on the measurement vector denotes the kth heart cycle. Similar notation is also used for the transfer and noise vectors. In MLE the estimate $\hat{\boldsymbol{\theta}}^k{}_{ML}$ is that which most likely caused the observed measurement to occur, or more specifically with which the PDF is maximized.

4.4.3 MLE for Deterministic Parameters

In Sections 4.3.1 and 4.3.2 the distribution of the measurement vector $\mathbf{y}_k$ was derived for both types of deterministic parameters with all three noise models. In each case the PDF was Gaussian with mean μ_y, and some specified covariance Σ that matched the variance of the noise. The likelihood function that describes the joint probability of the measurement is expressed,

$$\begin{aligned} l\left(\mathbf{y}_k;\hat{\boldsymbol{\theta}}^k\right) &= \Pi_{k=1}^c \left(2\pi \det(\Sigma)^{\frac{1}{2}} \exp\left(-\frac{1}{2}\left(\mathbf{y}_k - \mu_y\right)^T \Sigma^{-1}\left(\mathbf{y}_k - \mu_y\right) \right) \right) \\ &= 2\pi \det(\Sigma)^{\frac{1}{2}} \exp\left(-\frac{1}{2}\sum_{k=1}^c \left(\mathbf{y}_k - \mu_y\right)^T \Sigma^{-1}\left(\mathbf{y}_k - \mu_y\right) \right) \end{aligned} \tag{56}$$

where minimizing the exponent will thereby maximize (56) yielding an estimate for $\hat{\boldsymbol{\theta}}^k$ that most likely caused the observed measurement with that probability distribution. Therefore,

$$
\begin{aligned}
\hat{\boldsymbol{\theta}}^k{}_{ML} &= \arg\max_{\hat{\boldsymbol{\theta}}}\left(l\big(\mathbf{y}_k;\hat{\boldsymbol{\theta}}^k\big)\right) \\
&= \arg\min_{\hat{\boldsymbol{\theta}}}\left(-\frac{1}{2}\sum_{k=1}^{c}\big(\mathbf{y}_k-\mu_y\big)^T\hat{\Sigma}_{ML}^{-1}\big(\mathbf{y}_k-\mu_y\big)\right)
\end{aligned}
\tag{57}
$$

Again, theoretically, to solve (57) we take the derivative with respect to the parameter we want to estimate, and set it equal to zero. Similar to LS, we use an estimation algorithm to find $\hat{\boldsymbol{\theta}}^k{}_{ML}$. The covariance matrix $\hat{\Sigma}_{ML}$, for an initial guess $\hat{\boldsymbol{\theta}}^k{}_{ML}$ is expressed,

$$
\hat{\Sigma}_{ML} = \frac{1}{j}\sum_{j=1}^{n}\big(\hat{\mathbf{y}}_k-\hat{\mu}_y\big)^T\big(\hat{\mathbf{y}}_k-\hat{\mu}_y\big)
\tag{58}
$$

where $\hat{\mathbf{y}}_k = \hat{\mathbf{a}}_k+\hat{\mathbf{e}}_k$ and $\hat{\mu}_y = \mathrm{E}\big(\hat{\mathbf{y}}_k\big)$. Then, $\hat{\Sigma}_{ML}$ is used to solve (57) and find the estimate.

If the noise $\hat{\mathbf{e}}_k \sim N\big(0,\sigma^2\big)$, then covariance $\hat{\Sigma}_{ML} = \sigma^2$ and (57) becomes a LS expression, and $\hat{\boldsymbol{\theta}}^k{}_{ML} = \hat{\boldsymbol{\theta}}^k{}_{LS}$. That is, the best possible estimate is that of the least-squares because in this situation the smallest possible variance is achieved. However, if the noise does not conform to those assumptions, the MLE regression procedure must be carried out with an initial guess for $\hat{\boldsymbol{\theta}}^k{}_{ML}$. The previous statement justifies using $\hat{\boldsymbol{\theta}}_{LS}$ as the initial guess, and the algorithm becomes a form of weighted least-squares.

4.4.4 MLE for Stochastic Parameters

As discussed in **Section 4.3.3** the PDF of the measurement vector is not easily derived

when the parameters are stochastic. The likelihood function is in fact the PDF expressed,

$$l(\mathbf{y}_k;\mathbf{\theta}^k) = \int_{-\infty}^{\infty} f_z(\mathbf{y}_k - \mathbf{e}_k) f_e(\mathbf{e}_k) de \tag{59}$$

where $z = \mathbf{a}_k$, $\mathbf{\theta}^k \sim N(\mu^*, \sigma^{2^*})$, for unknown mean and variance.

The MLE is then,

$$\begin{aligned}\hat{\mathbf{\theta}}^k{}_{ML} &= \arg\max_{\hat{\mathbf{\theta}}_0}\left(l(\mathbf{y}_k;\hat{\mathbf{\theta}}^k)\right) \\ &= \arg\max_{\hat{\mathbf{\theta}}_0}\left(\int_{-\infty}^{\infty} f_z(\mathbf{y}_k - \mathbf{e}_k) f_e(\mathbf{e}_k) de\right)\end{aligned} \tag{60}$$

for $\hat{\mathbf{\theta}}_0$, the parameter vector that corresponds to the PDF of $\mathbf{y}_k$.

4.4.5 Estimating Time of Activation

Noting that we return to the previous notation, we recall (29) assuming that the electrical

activation process in the heart starts at time τ within the heart cycle. The model is then

described,

$$\mathbf{y}(\mathbf{r}_i,\mathbf{t}_{j,k}) = \mathbf{a}(\mathbf{r}_i,(\mathbf{t}-\tau)_{j,k},\mathbf{\theta}^k) + \mathbf{e}(\mathbf{r}_i,\mathbf{t}_{j,k}), \tag{61}$$

We estimate the time at which activation starts by using a sequential method described as

follows. For a particular heart cycle k, we assume we can simulate

$\hat{\mathbf{y}}(\mathbf{r}_i,\mathbf{t}_{j,k}) = \hat{\mathbf{a}}(\mathbf{r}_i,(\mathbf{t}-\tau^*)_{j,k},\mathbf{\theta}^k)$ so that τ^* is defined sequentially every time as,

$$\tau_{j,k}^* = \mathbf{t}_j + \sum_{l=1}^{k-1} T_l \tag{62}$$

Then, if at each iteration the cost between the two measurement vectors is computed,

$$\cos t_j = \left\| \mathbf{y}(\mathbf{r}_i, \mathbf{t}_{j,k}) - \hat{\mathbf{y}}(\mathbf{r}_i, \mathbf{t}_{j,k}) \right\|_2^2 \tag{63}$$

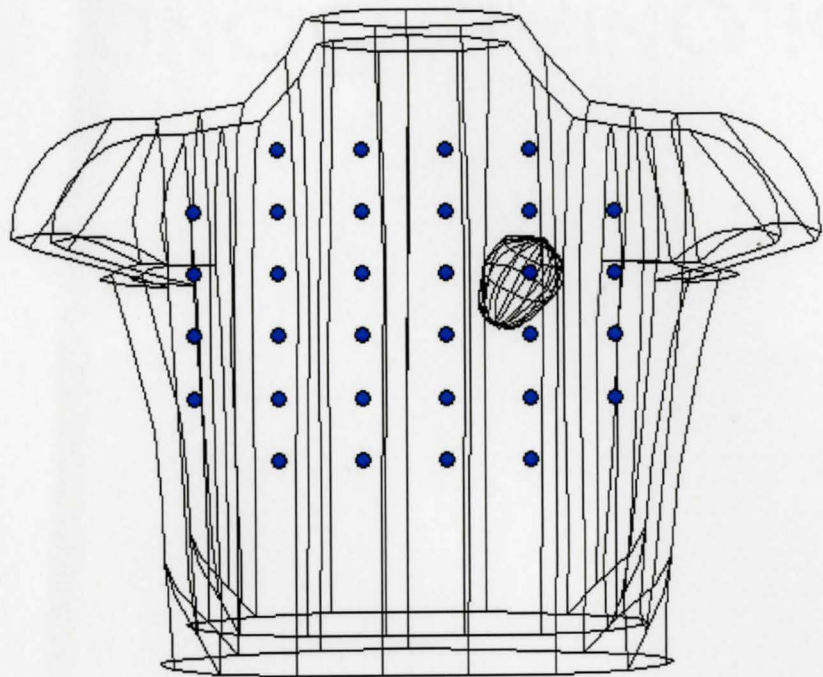for $j = 1, \ldots, n$, then the minimal $\cos t_j$ will occur when $\tau^* = \tau$.
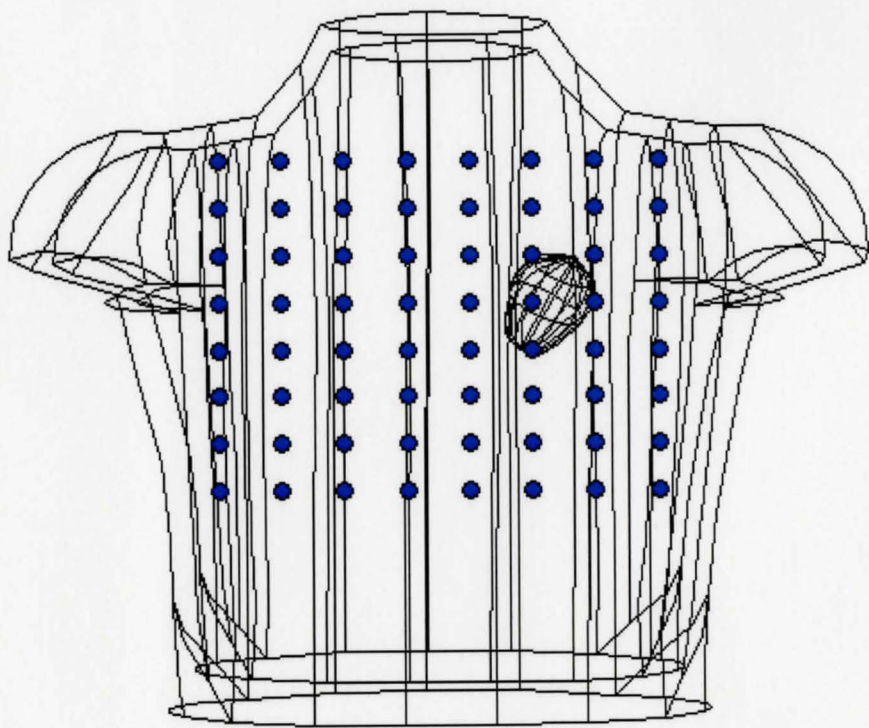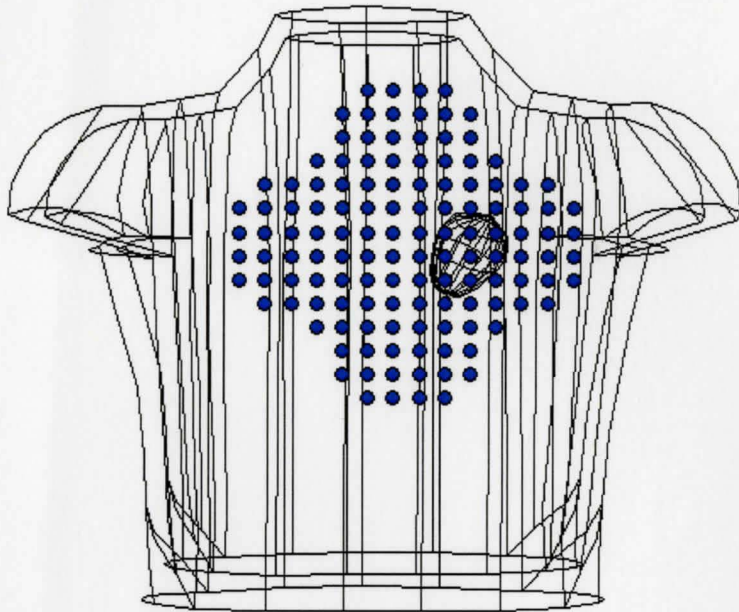
Figure 4 - 1: Thirty-two Sensors on Torso Surface

Figure 4 - 2: Sixty-four Sensors on Torso Surface

Figure 4 - 3: One Hundred Twenty-eight Sensors on Torso Surface

5   NUMERICAL EXAMPLES

We use numerical examples to demonstrate the performance of our proposed estimators. Note that we are using simulated measurements on the torso surface to validate that the parameters can be estimated and that the inverse model is applicable, and can be used in a realistic clinical environment. In this chapter we first detail our numerical examples, where we present the parameters of the diffusion model, and the noise models, that we used for our estimation. We also discuss how we will measure the performance of our results. Then we present our numerical results, where we discuss the implementation of our estimation algorithms in Matlab and we evaluate their performance using the aforementioned measures. To simplify the notation we use the same form as in Section 4.4.2 where the spatial-temporal dependence is implied.

In implementing the diffusion model we set the torso conductivity to $5\mu\, S/m$ [Malmivuo, 1995], $\varepsilon = 0.01$, $\alpha = 0.1$, $\beta = 0.5$, $\gamma = 1$, and $\delta = 0$ as done in Comsol's Model Gallery. We assume the heart cycle is 750ms in length and choose the diffusivity D so that the activation wavefront traverses the whole heart in 250ms according to this approximation [Cengel, 2003],

$$D \cong \frac{d^2}{4\tau} \tag{64}$$

where d is the distance traveled in cm, and τ denotes time in seconds. We sample measurements at 100 Hz for 4 heart cycles. In Figures 5-1 and 5-2 we show the electric potential and magnetic field measured at the ECG/MCG arrays on the torso surface during one heart cycle.

We import the measurement vector from Comsol and we use Matlab for the numerical estimation algorithms. In Figure 5-3 we show an example of our Matlab code, where the user is prompted for the number of sensors, the dimensions of the torso in cm, the number of heart cycles, and the signal-to-noise ratio (SNR) ratio. Let σ_e^2 and σ_b^2 represent the powers of the noise for the measurement vectors $\mathbf{y}_{ek}$ and $\mathbf{y}_{bk}$ such that,

$$\sigma_e^2 = \frac{1}{mnc}\sum_{j=1}^{n}\sum_{=1}^{c}\left\|\mathbf{y}_{ek} - \hat{\mathbf{y}}_{ek}\right\|^2$$

$$\sigma_b^2 = \frac{1}{mnc}\sum_{j=1}^{n}\sum_{=1}^{c}\left\|\mathbf{y}_{bk} - \hat{\mathbf{y}}_{bk}\right\|^2$$

where recall $\hat{\mathbf{y}}_k$ represents the analytical model which we mentioned in Chapter 4 and the subscripts e and b denote the electric potential and magnetic field respectively. Then the SNR in dB is defined as,

$$SNR = 10\log\left(\frac{\sum\left\|\mathbf{y}_k\right\|^2}{\sigma^2}\right), \tag{65}$$

where we assume $\sigma^2 = \sigma_e^2 + \sigma_b^2$ is the power of the noise.

In simulating the modeling noise we choose two cases for which to run the estimation; white Gaussian noise (WGN), and spatially correlated noise (CN). First, WGN is achieved using a random number generator in Matlab where the variables have a normal distribution. The second, CN, is computed from the white noise using low pass filtering in the frequency domain. We apply a fast Fourier transform which yields the coefficients of the white noise. We then modify the magnitude of these coefficients so that the spectral density is no longer flat which introduces correlation in the time domain. Therefore, by transforming the Fourier coefficients back a spatially correlated matrix is obtained. Because we want to compare estimation results between the two noise distributions, when we design our filter we ensure that the correlated noise has the same power as the input WGN. A control variable is used which computes the input power and modifies the spectral density such that output power closely matches that of the input.

In all examples, unless otherwise stated, we assume a uniform 32 sensor array is used for ECG/MCG measurements. In our numerical study we choose two heart parameters, the diffusivity D, and excitability ε, to show the applicability of estimation algorithms.

5.1 PERFORMANCE MEASURE

To measure the performance of our estimator, we compute the mean square error (MSE) where the amount by which an estimator $\hat{\theta}^k$ differs from its true value is given by,

$$MSE\left(\hat{\theta}^k\right) = \left\| \left(\hat{\theta}^k - \theta^k \right)^2 \right\|^2 \tag{66}$$

where the MSE is averaged over all heart cycles. The magnitude of the $MSE(\hat{\theta}^k)$ will allow us to evaluate the performance of our estimation.

We also compute the MSE for the measurement vector, which can be termed 'curve fitting' because we wish to determine whether the analytical model fits the measured data. This will allow us to determine how much modeling error is present when we simulate surface measurements in comparison with the analytical model. The error between the model $\hat{\mathbf{y}}_k$ and the surface measurements is given by,

$$MSE(\hat{\mathbf{y}}_k) = \left\| (\hat{\mathbf{y}}_k - \mathbf{y}_k)^2 \right\|^2 \tag{67}$$

Then we compute the Cramer Rao Bound (CRB) which puts a lower bound on the variance of our unbiased estimator $\hat{\theta}^k$ and is given by,

$$\mathrm{var}(\hat{\theta}_p^k) \geq \left[\mathbf{T}(\theta^k) \right]_{pp}^{-1} \tag{68}$$

for $p = 1,2,\ldots,r$ and where we assume $\theta^k = \left[\theta_1^k; \cdots, \theta_r^k \right]^T$ is a known vector of deterministic parameters and $\mathbf{T}(\theta^k)$ denotes the $r \times r$ Fisher Information Matrix (FIM) given by,

$$\mathbf{T}(\theta^k)_{pq} = -\mathrm{E}\left(\frac{\partial \ln f_Y(\mathbf{y}_k; \theta^k)}{\partial \theta_p} \frac{\partial \ln f_Y(\mathbf{y}_k; \theta^k)}{\partial \theta_q} \right) \tag{69}$$

for $p = 1,2,\ldots,r$, $q = 1,2,\ldots,r$ and where $f(\mathbf{y}_k; \theta^k)$ is the PDF of the observation vector given the parameter . We compute the derivative in (69) at the true value of θ^k to obtain a

measure of the amount of information content carried by $\mathbf{y}_k$ about the unknown parameter.

As derived in [Kay, 1993] for $\mathbf{y}_k \sim N\left(\mu\left(\theta^k\right),\Sigma\left(\theta^k\right)\right)$ the FIM is given by,

$$\mathbf{T}\left[\theta^k\right]_{pq} = \left[\frac{\partial\mu\left(\theta^k\right)}{\partial\theta_p}\right]^T \Sigma^{-1}\left(\theta^k\right)\left[\frac{\partial\mu\left(\theta^k\right)}{\partial\theta_q}\right] + \frac{1}{2}tr\left[\Sigma^{-1}\left(\theta^k\right)\frac{\partial\Sigma\left(\theta^k\right)}{\partial\theta_p}\Sigma^{-1}\left(\theta^k\right)\frac{\partial\Sigma\left(\theta^k\right)}{\partial\theta_q}\right]$$

(70)

$$\text{where } \frac{\partial\mu\left(\theta^k\right)}{\partial\theta_p} = \begin{bmatrix} \dfrac{\partial\left[\mu\left(\theta^k\right)\right]_{11}}{\partial\theta_p} & \dfrac{\partial\left[\mu\left(\theta^k\right)\right]_{12}}{\partial\theta_p} & \cdots & \dfrac{\partial\left[\mu\left(\theta^k\right)\right]_{1m}}{\partial\theta_p} \\ \dfrac{\partial\left[\mu\left(\theta^k\right)\right]_{21}}{\partial\theta_p} & \dfrac{\partial\left[\mu\left(\theta^k\right)\right]_{22}}{\partial\theta_p} & \cdots & \dfrac{\partial\left[\mu\left(\theta^k\right)\right]_{2m}}{\partial\theta_p} \\ \vdots & \vdots & \ddots & \\ \dfrac{\partial\left[\mu\left(\theta^k\right)\right]_{n1}}{\partial\theta_p} & \dfrac{\partial\left[\mu\left(\theta^k\right)\right]_{n2}}{\partial\theta_p} & \cdots & \dfrac{\partial\left[\mu\left(\theta^k\right)\right]_{nm}}{\partial\theta_p} \end{bmatrix}$$

(71)

where tr denotes the trace operator, Σ denotes the covariance matrix, and m, n denote the number of sensors and time samples, respectively. We compute the FIM such that the modeling noise is White Gaussian with $\Sigma = \sigma^2\mathbf{I}$ which using (70) reduces to [Kay,1993],

$$\mathbf{T}\left[\theta^k\right]_{pq} = \left[\frac{\partial\tilde{\mathbf{a}}\left(\theta^k\right)}{\partial\theta_p}\right]^T \frac{1}{\sigma^2}\mathbf{I}\left[\frac{\partial\tilde{\mathbf{a}}\left(\theta^k\right)}{\partial\theta_q}\right]$$

(72)

where $\tilde{\mathbf{a}}\left(\theta^k\right)$ is of the same form as (71). Note that in (71) we use the subscript k to denote the cycle and therefore we can compute the CRB of the estimator for each kth heart cycle. We then compute the CRB for spatially correlated noise, where the covariance matrix is of the same format as (38).

For scalar θ^k the FIM is given by,

$$T[\theta^k] = \frac{1}{\sigma^2}\left(\left(\frac{\partial \breve{\mathbf{a}}(\theta^k)}{\partial \theta}\right)^2\right) \tag{73}$$

where $\breve{\mathbf{a}}(\theta^k)$ is of the same form as (71) but for a scalar parameter.

Now we discuss the analytical approach to evaluating the CRB for stochastic parameters however we leave the numerical computation as future work. As we showed in Section 4.3.4 the PDF of the measurement vector can be expressed as the convolution in (40). Recall that $f_Y(\mathbf{y}_k;\theta^k)$ represents the PDF of $\mathbf{y}_k$ for parameter $\theta^k \sim N(\mu*,\Sigma*)$. Then (69) is re- written,

$$T(\theta^k)_{pq} = -\mathrm{E}\left(\left(\frac{\partial \ln f_Y(\mathbf{y}_k;\theta^k)}{\partial \theta_p}\right)^2\right) \tag{74}$$

where the partial derivative is now conditional on the PDF of the parameter, $f_\theta(\theta^k)$, and we can evaluate it using,

$$\frac{\partial \ln f_Y(\mathbf{y}_k;\theta^k)}{\partial \theta_p} = \frac{1}{g(\mathbf{y}_k;\theta^k)} \times \frac{\partial g(\mathbf{y}_k;\theta^k)}{\partial \theta_p} \times \frac{\partial f_\theta(\theta^k)}{\partial \theta_p} \tag{75}$$

To compute the CRB substitute (74) in (73) to yield the FIM.

5.2 NUMERICAL RESULTS

In this section we choose to first display the estimation results using ECG measurements only, and then ECG/MCG. We perform the estimation for 32, 64, and 128 sensors, although any number can be entered into the program. We plot results for two different noise models; white Gaussian noise (WGN) and spatially correlated noise (CN).

5.2.1 LS Estimation

In Matlab we use the *fminsearch* command which minimizes the least-squares cost function by using the Nelder-Mead simplex search method [Lagarias, 1998]. In Figure 5-4 we illustrate a sample call to *fminsearch* which then returns the least squares estimate. Note that we supply an initial guess for the estimate which can have a significant effect on the output.

We first assume the excitability and diffusivity parameters are DTI and in Figures 5-5, 5-6 we show $MSE(\hat{\theta})$ for both WGN and CN using ECG measurements from 32 and 64 sensors, respectively. Then we repeat the estimation using ECG/MCG measurements which we show in Figures 5-7, 5-8.

To implement deterministic 'short-scale' time varying parameters we use two slow changing cosines such that,

$$\theta_i = \alpha_1 \cos(w_1(i)) + \alpha_2 \cos(w_2(i)) \tag{76}$$

where w is in radians, and where α is the parameter we wish to estimate. The estimation results for ECG and ECG/MCG are shown in Figures 5-9,10-12.

Then we run the estimation again but this time with stochastic parameters that are 'long-scale' time varying and have Gaussian distribution with unknown mean and variance. We show our $MSE(\hat{\theta})$ plots in Figures 5-13,14-16.

5.2.2 MLE Estimation

As we explained in Chapter 4 for WGN the MLE method is equivalent to the LS and therefore we only implement the MLE for spatially correlated noise. For DTI and DTV parameters we implement them in the same way as described in the previous section. We then compute the MLE by using the *fminsearch* command again to minimize the exponent of the PDF as shown in (55). We display the $MSE(\hat{\theta})$ estimation results for DTI and DTV parameters in Figures 5-17,18-20 respectively, where in each plot we include the results for 32 and 64 sensors.

We leave the computation of MLE for stochastic parameters as future work, where the PDF of the measurement vector must first be computed. As an example we try to illustrate the PDF for one Gaussian parameter by running a Monte-Carlo simulation and plotting a histogram of ECG measurements. We ran the simulation using Matlab, and in Figure 5-21 we show the histogram for the excitability parameter.

5.2.3 Curve Fitting and Estimation of Activation Time

We show $MSE(\hat{y})$ as a function of SNR(dB) for ECG and ECG/MCG measurements where the plots include results for both WGN and CN. Although it is uncommon to perform the MCG measurement by itself, for completeness we show the $MSE(\hat{y})$ for

ECG, MCG, and ECG/MCG for 32 sensors in Figure 5-22. The rest of the plots follow in Figures 5-23, 24.

We demonstrate the applicability of our technique to estimate the time of activation using ECG and ECG/MCG in Figure 5-25. We use DTI parameters and we compute $MSE(\hat{\theta})$ as a function for SNR for WGN.

5.3 PERFORMANCE ANALYSIS

We evaluate the performance of the estimation algorithms by making some observations regarding the plots in Section 5.2.

5.3.1 LS Estimation

As we expected we observe that for LS estimation there is no significant difference in $MSE(\hat{\theta})$ between WGN and spatially CN of the same power. We expected this result because LS does not take into account the noise distribution. In comparing ECG versus ECG/MCG sensor arrays, we notice that the inclusion of the magnetic field yields a higher error. In fact, we notice this trend throughout our results, and we discuss it in the CRB section later in this chapter.

As for difference in the number of sensors, we notice specifically that for DTI and STO parameters 64 sensors yield slightly larger mean square errors while the results are similar between 32 and 64 sensors for DTV parameters.

We compared $MSE(\hat{\theta})$ for the different type of parameters. We see that when using ECG sensor array; STO parameters have the largest mean square error, while DTI and DTV are similar. When using ECG/MCG arrays the $MSE(\hat{\theta})$ is largest for DTI parameters, then smaller for DTV, and least for STO parameters.

5.3.2 MLE

In our estimation results we do not see conclusive results when comparing $MSE(\hat{\theta})$ plots of 32 versus 64 sensors. We also saw a similar result with LS estimation, and we suspect it is related to the uniform grid of sensors and that the power of the signal may decay as the distance from the heart increases.

However we do notice again that ECG/MCG sensor array measurements have larger $MSE(\hat{\theta})$. Unlike LS, we do not see a significant difference in estimation error between DTI and DTV parameters.

We expected that MLE will give us the best fit for the assumed PDF of our measurement vector, and we verified this in our plot as we see that $MSE(\hat{\theta})$ is significantly smaller in comparison to LS estimation error.

5.3.3 Curve Fitting and Estimating Time of Activation

When comparing $MSE(\hat{y})$ for the two noise distributions we see that there is a significant difference which we expected. We know that WGN and correlated noise will affect our surface measurements differently and therefore the error in curve fitting will be different. We also observe that in both cases of sensor arrays, $MSE(\hat{y})$ is higher for 64 sensors.

Our proposed method for estimating the activation time yielded somewhat large MSE errors, which suggests that our algorithm which minimizes the cost sequentially is not a good method.

5.3.4 CRB

We now discuss the CRB, which we computed for both ECG and ECG/MCG measurements. In Figure 5-26 we show the $CRB(\hat{\theta})$ versus the two parameters, for a 32 ECG sensor array with WGN modeling noise where SNR = 5dB.

We then compute $CRB(\hat{\theta})$ as a function of SNR and plot it along with the $MSE(\hat{\theta})$ from LS and MLE for DTI parameters.

As expected, we have further evidence in Figure 5-27 that the CRB gives the lowest variance attainable, followed by MLE estimation and then LS.

We run the same computation for ECG/MCG and we display the results in Figures 5-28, 29. We notice that the CRB for ECG measurements is lower than for ECG/MCG measurements, which suggests that using the magnetic field measurements might not provide significant improvement in our ability to estimate the parameters. In fact, we saw similar results in estimating the parameters using both LS and MLE. This is an unexpected result because we do not introduce any additional parameters that might affect the FIM. However we suspect that in introducing an additional dimensionality in the measurement vector with MCG, this may have resulted in higher nonlinearity in the

model, and thus a higher CRB. In reality, MCG may provide useful especially, for example, when torso conductivity is not known.

We run the CRB computation again, but this time for 64 sensors for both ECG, and ECG/MCG which we show in Figures 5-30,31-33. As expected the variance decreases as the number of sensors increase, which verifies for us that with more information the FIM increases and should yield better estimation results.

We show our results for the CRB computation for spatially correlated noise in Figures 5-34, 35-37. In comparison with WGN, we see that the CRB is higher for the correlated noise, which we expected since there are additional covariance matrix parameters. Again we notice that CRB for ECG/MCG is higher than for ECG, which we commented on earlier.

To further illustrate the CRB results in a 2D plot, we choose 1 value from each of the previously presented 3D figures and plot it versus the type of sensor array. Therefore in Figure 5-38 we see for example, that for 1 set of parameters, the CRB value for 32 ECG sensor array is higher than 64 ECG sensor array, thus summarizing the observations we made earlier. This figure also presents a comparison between WGN and CN.
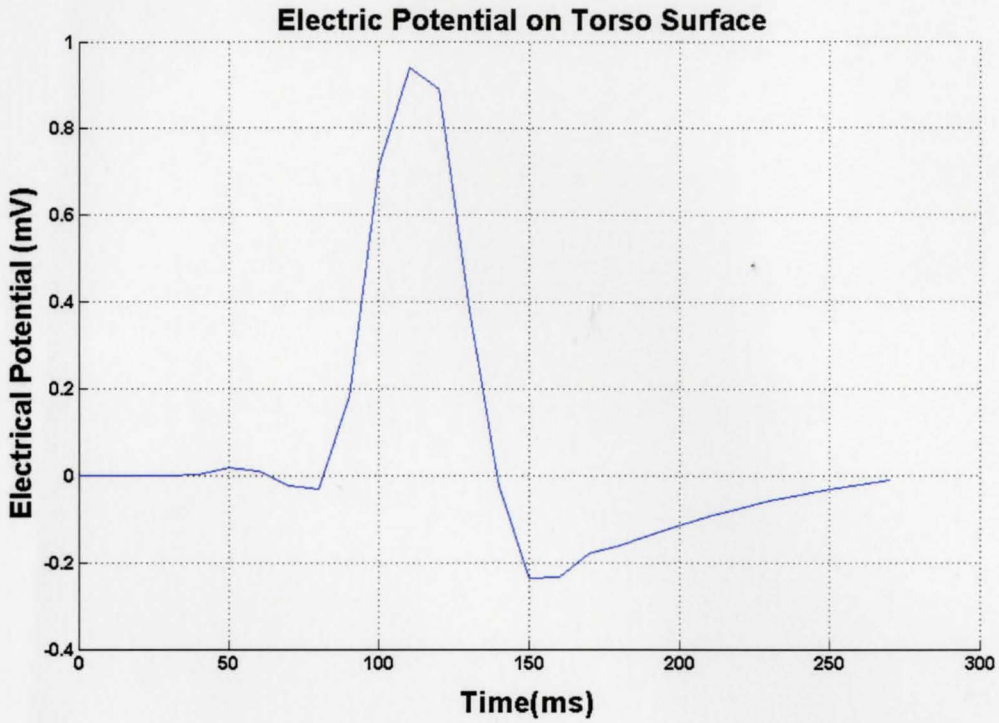
Figure 5 - 1: Electric Potential on Torso Surface
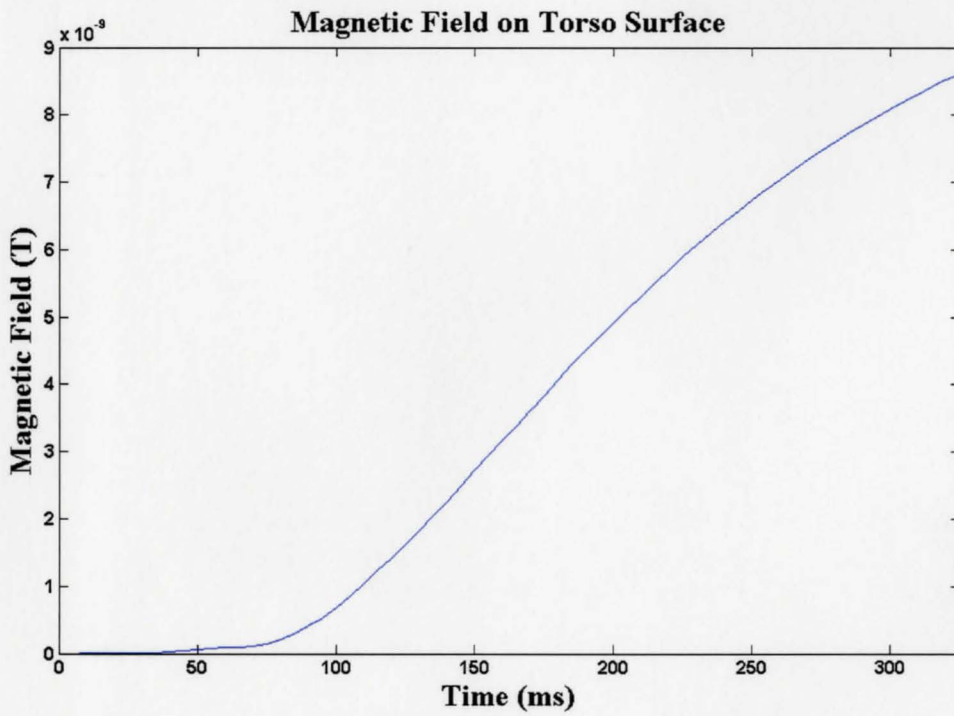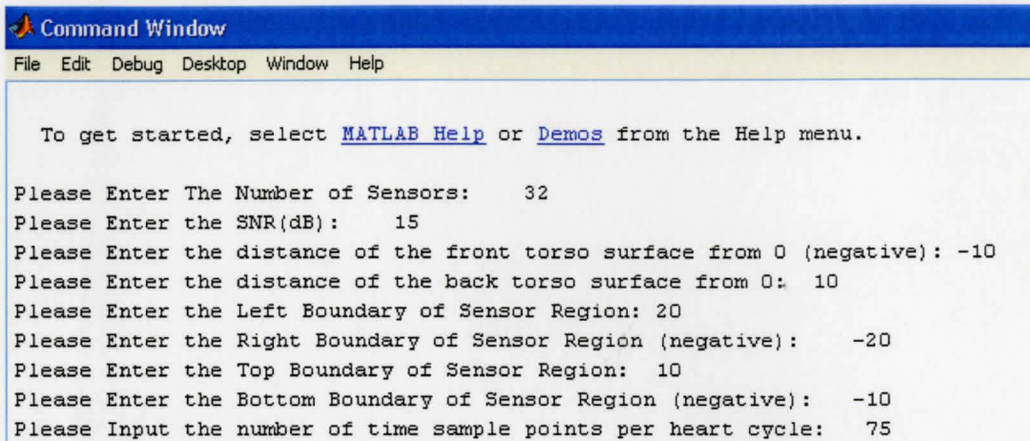
Figure 5 - 2: Magnetic Field on Torso Surface
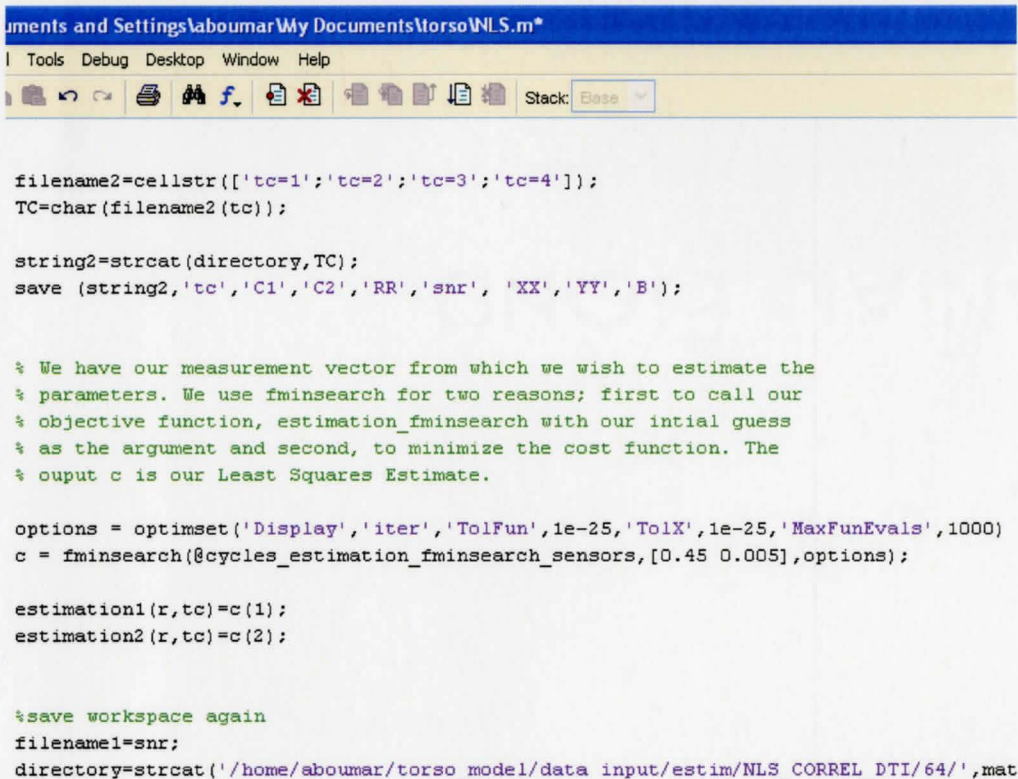
```
Command Window
File   Edit   Debug   Desktop   Window   Help

   To get started, select MATLAB Help or Demos from the Help menu.

Please Enter The Number of Sensors:    32
Please Enter the SNR(dB):    15
Please Enter the distance of the front torso surface from 0 (negative): -10
Please Enter the distance of the back torso surface from 0:   10
Please Enter the Left Boundary of Sensor Region: 20
Please Enter the Right Boundary of Sensor Region (negative):    -20
Please Enter the Top Boundary of Sensor Region:   10
Please Enter the Bottom Boundary of Sensor Region (negative):   -10
Please Input the number of time sample points per heart cycle:   75
```

Figure 5 - 3: User Input Prompt for Estimation

```
uments and Settings\aboumar\My Documents\torso\NLS.m*
  Tools   Debug   Desktop   Window   Help
                                            Stack: Base


filename2=cellstr(['tc=1';'tc=2';'tc=3';'tc=4']);
TC=char(filename2(tc));

string2=strcat(directory,TC);
save (string2,'tc','C1','C2','RR','snr', 'XX','YY','B');


% We have our measurement vector from which we wish to estimate the
% parameters. We use fminsearch for two reasons; first to call our
% objective function, estimation_fminsearch with our intial guess
% as the argument and second, to minimize the cost function. The
% ouput c is our Least Squares Estimate.

options = optimset('Display','iter','TolFun',1e-25,'TolX',1e-25,'MaxFunEvals',1000)
c = fminsearch(@cycles_estimation_fminsearch_sensors,[0.45 0.005],options);

estimation1(r,tc)=c(1);
estimation2(r,tc)=c(2);


%save workspace again
filename1=snr;
directory=strcat('/home/aboumar/torso_model/data input/estim/NLS_CORREL_DTI/64/',mat
```

Figure 5 - 4: LS in Matlab, fminsearch Function Call
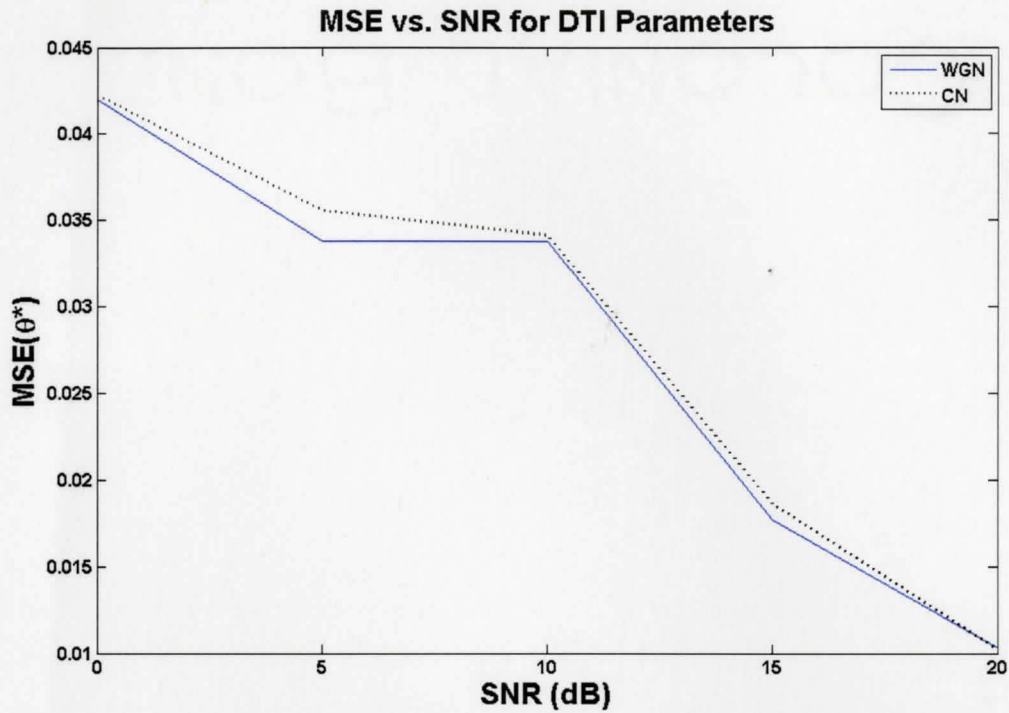
Figure 5 - 5: LS Estimation from 32 ECG Sensors for DTI Parameters
Note that we use θ* to denote $\hat{\theta}$
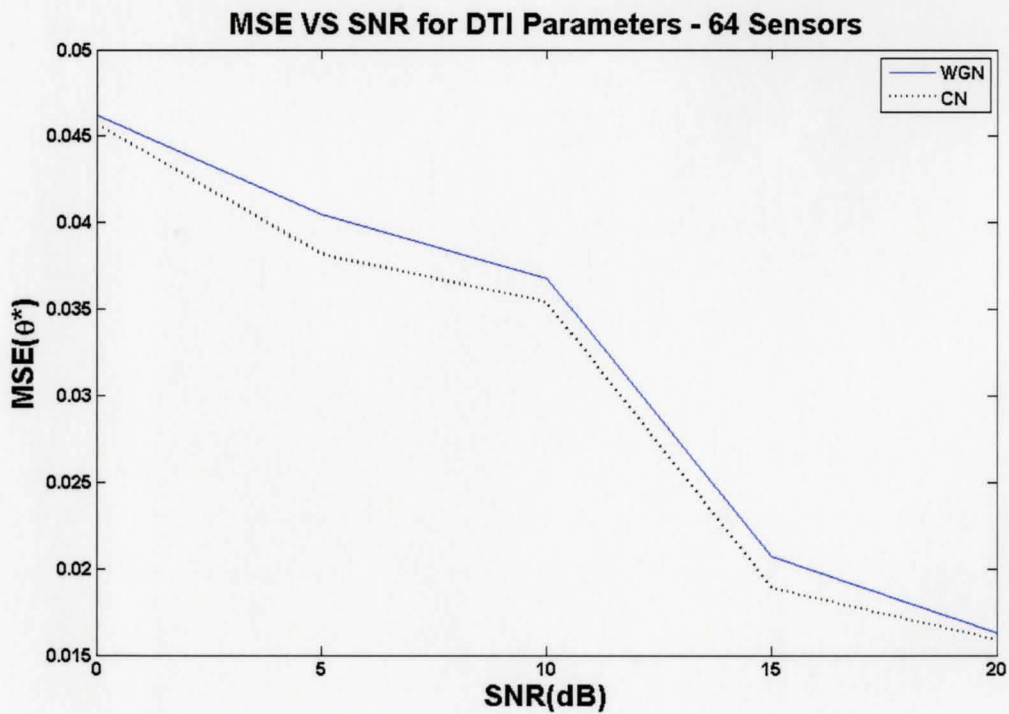
Figure 5 - 6: LS Estimation from 64 ECG Sensors for DTI Parameters
Note that we use θ* to denote $\hat{\theta}$
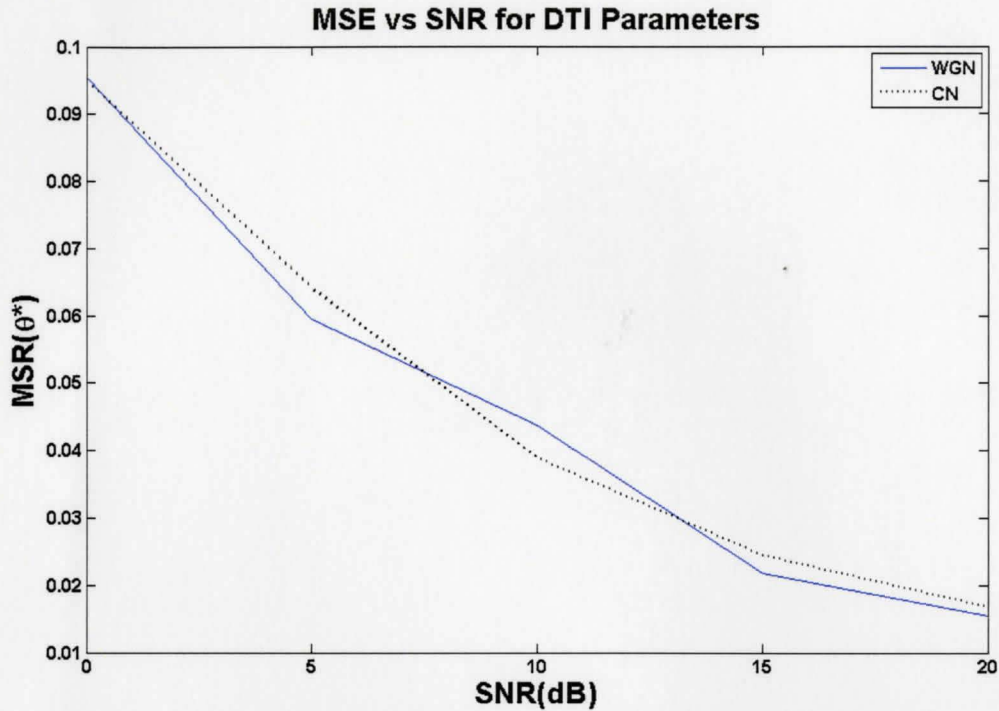
Figure 5 - 7: LS Estimation from 32 ECG/MCG Sensors for DTI Parameters
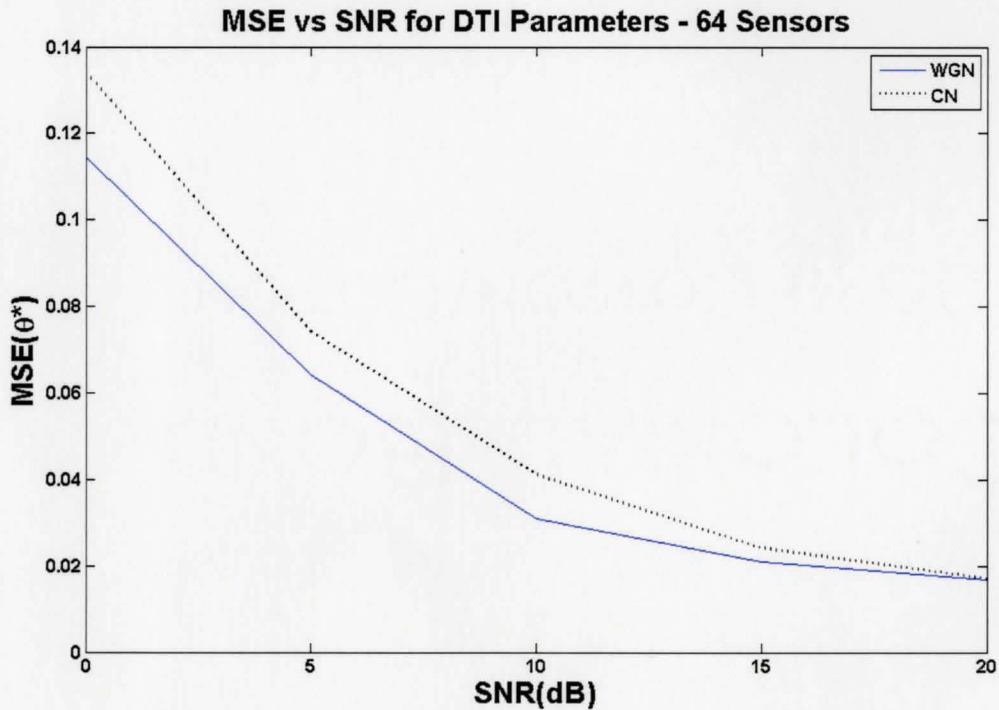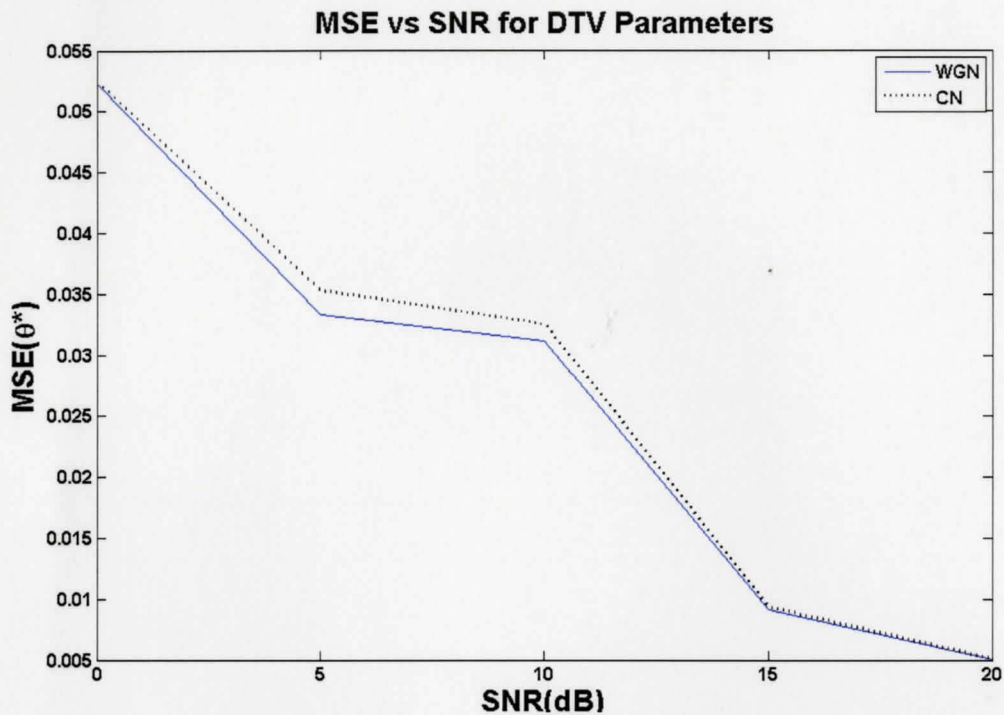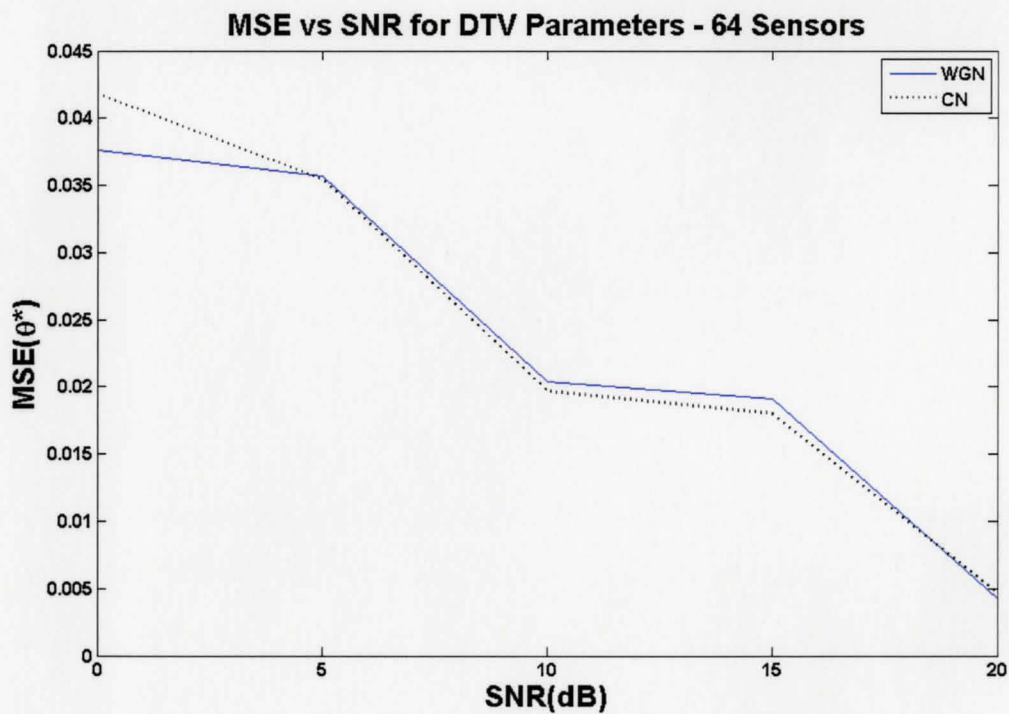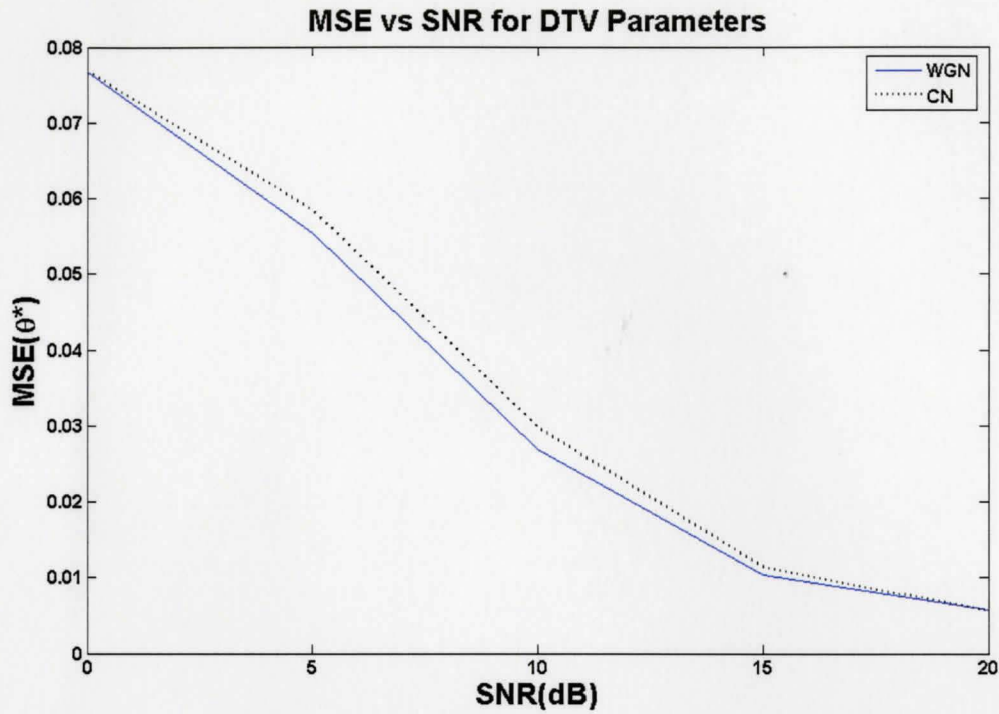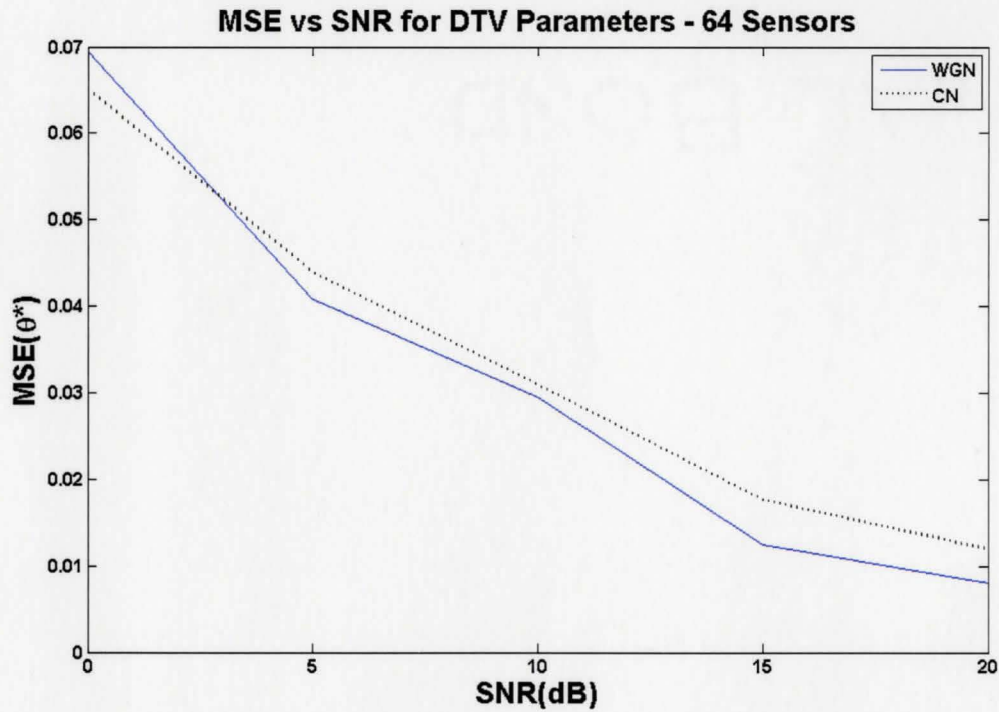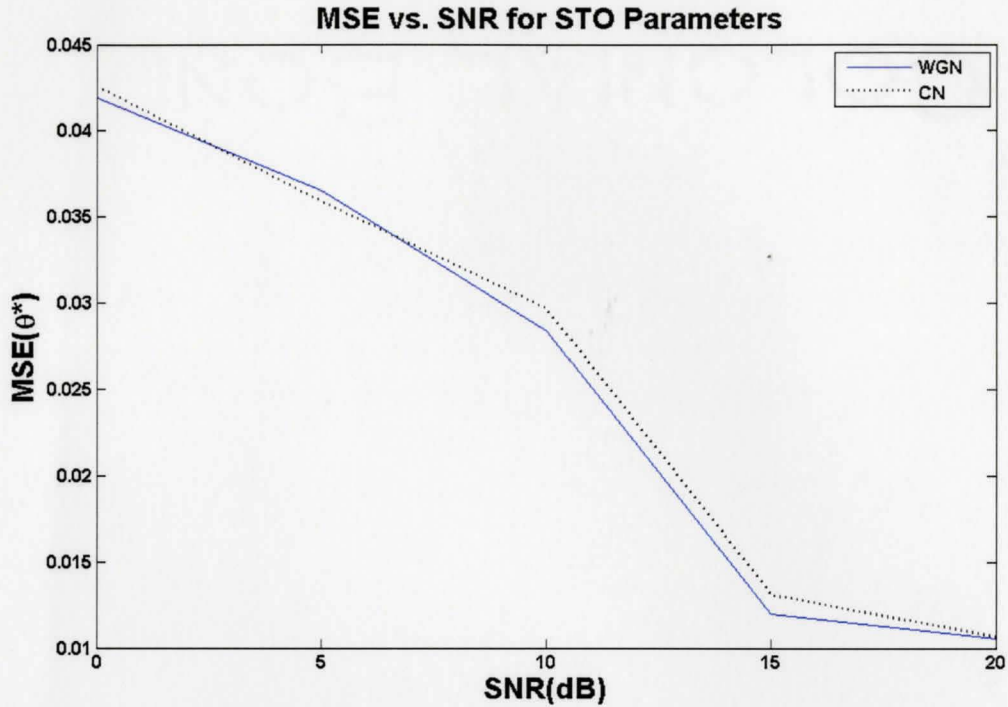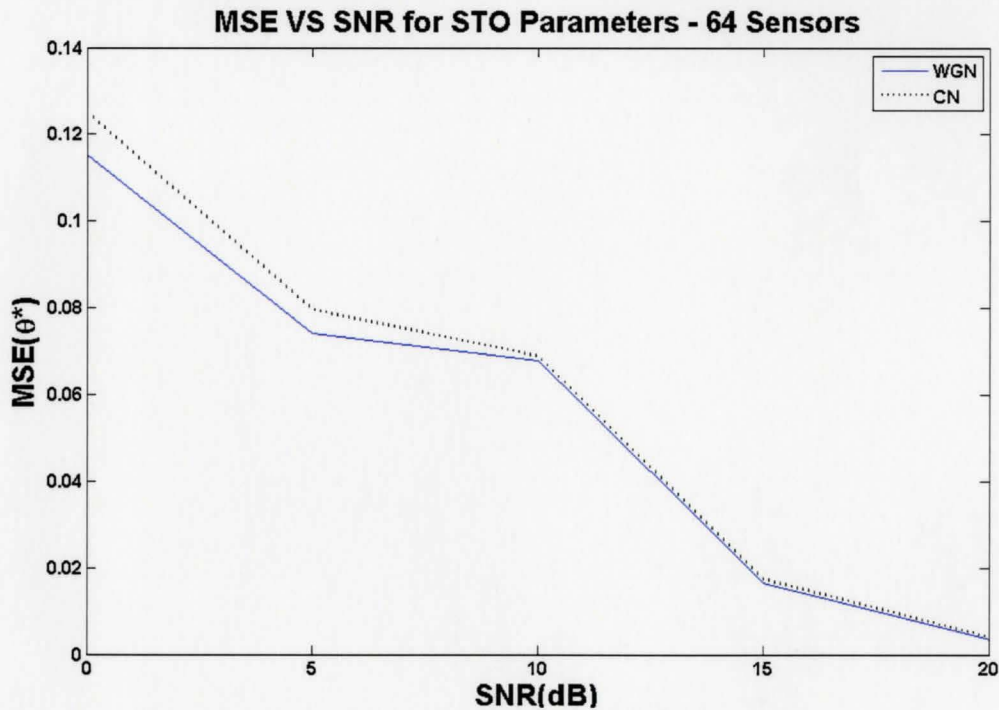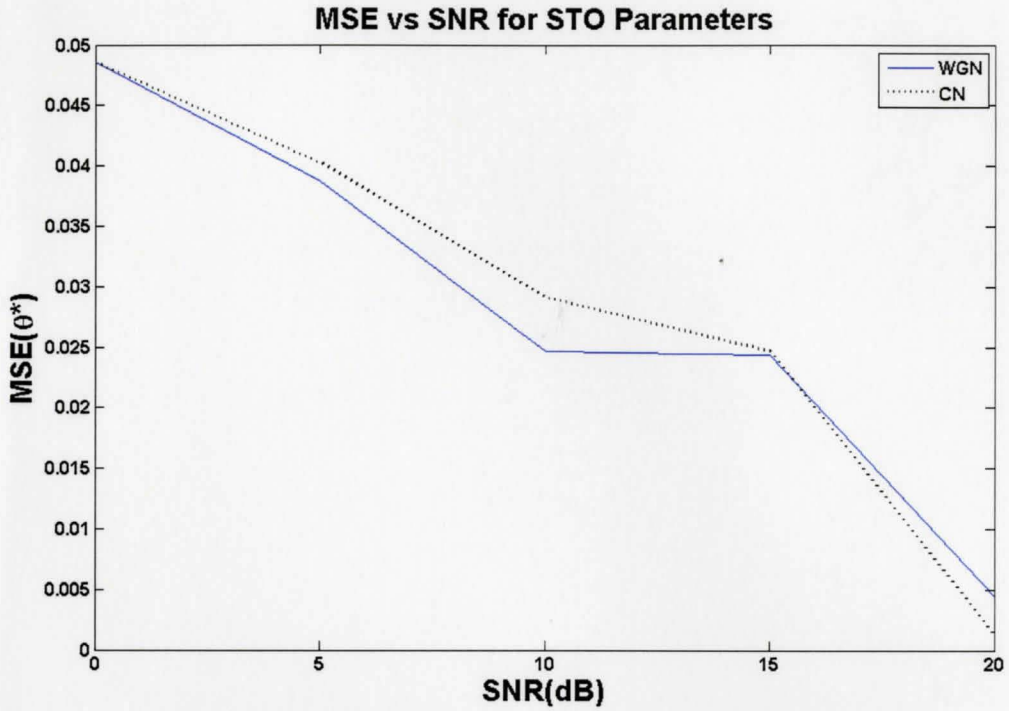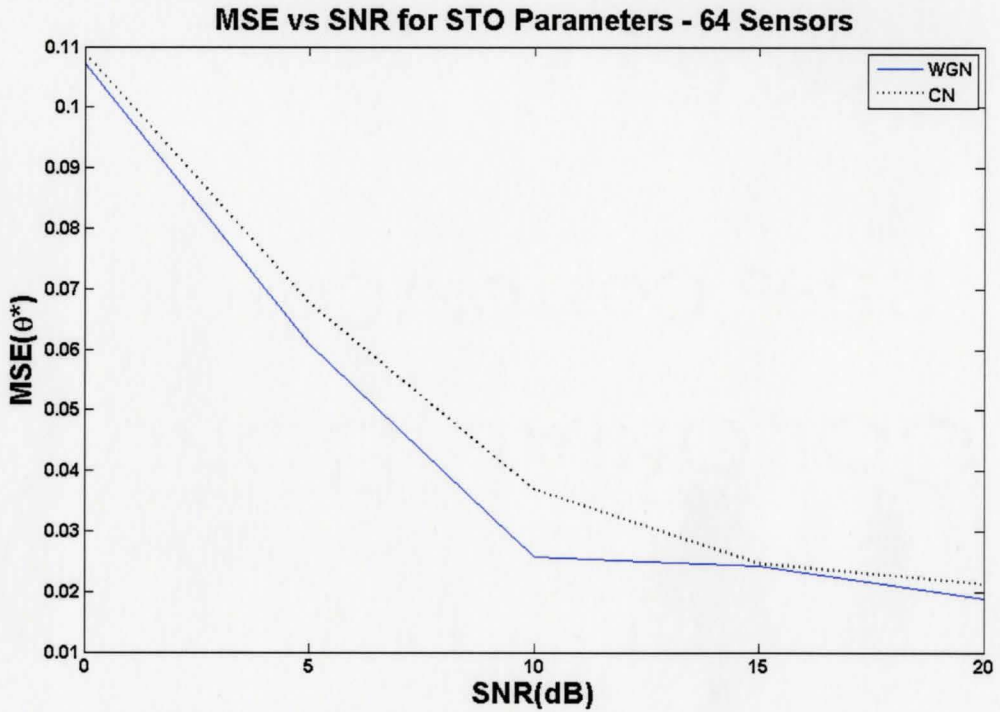Note that we use θ* to denote $\hat{\theta}$

Figure 5 - 8: LS Estimation from 64 ECG/MCG Sensors for DTI Parameters
Note that we use θ* to denote $\hat{\theta}$

Figure 5 - 9: LS Estimation from 32 ECG Sensors for DTV Parameters
Note that we use θ* to denote $\hat{\theta}$

Figure 5 - 10: LS Estimation from 64 ECG Sensors for DTV Parameters
Note that we use θ* to denote $\hat{\theta}$

Figure 5 - 11: LS Estimation from 32 ECG/MCG Sensors for DTV Parameters
Note that we use θ^* to denote $\hat{\theta}$

Figure 5 - 12: LS Estimation from 64 ECG/MCG Sensors for DTV Parameters
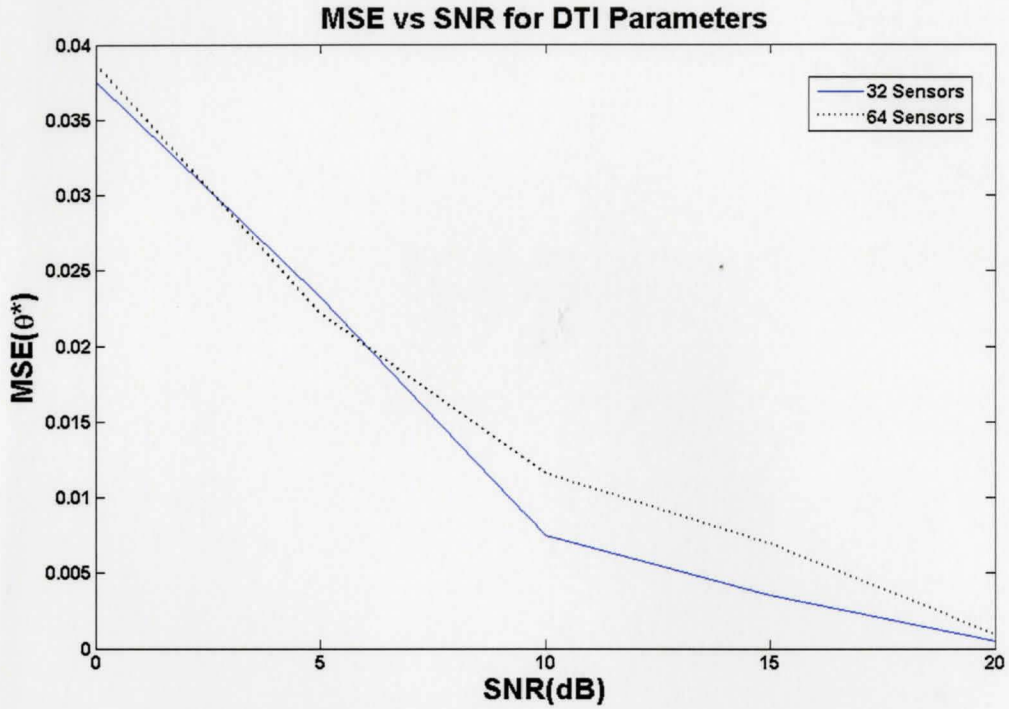Note that we use θ^* to denote $\hat{\theta}$

Figure 5 - 13: LS Estimation from 32 ECG Sensors for STO Parameters
Note that we use θ* to denote $\hat{\theta}$

Figure 5 - 14: LS Estimation from 64 ECG Sensors for STO Parameters
Note that we use θ* to denote $\hat{\theta}$

Figure 5 - 15: LS Estimation from 32 ECG/MCG Sensors for STO Parameters
Note that we use θ* to denote $\hat{\theta}$

Figure 5 - 16: LS Estimation from 64 ECG/MCG Sensors for STO Parameters
Note that we use θ* to denote $\hat{\theta}$

Figure 5 - 17: MLE from ECG Sensors for DTI Parameters
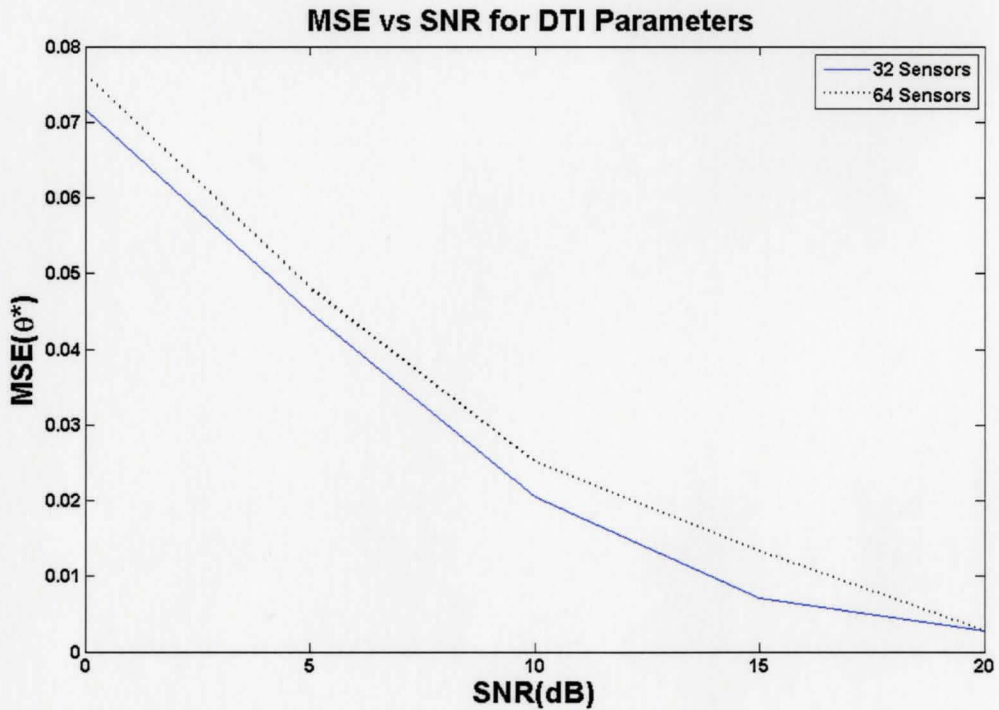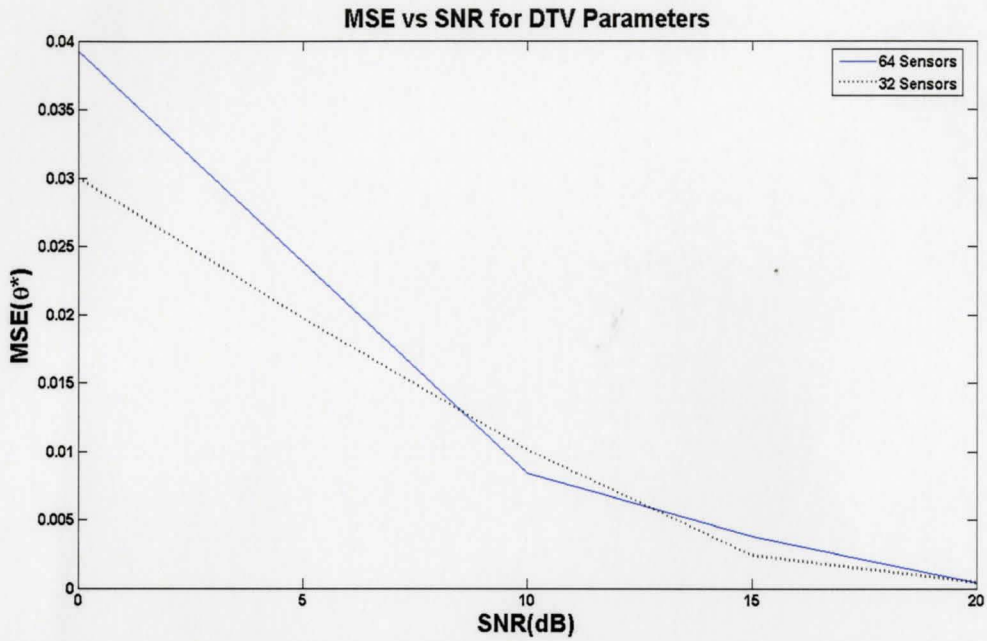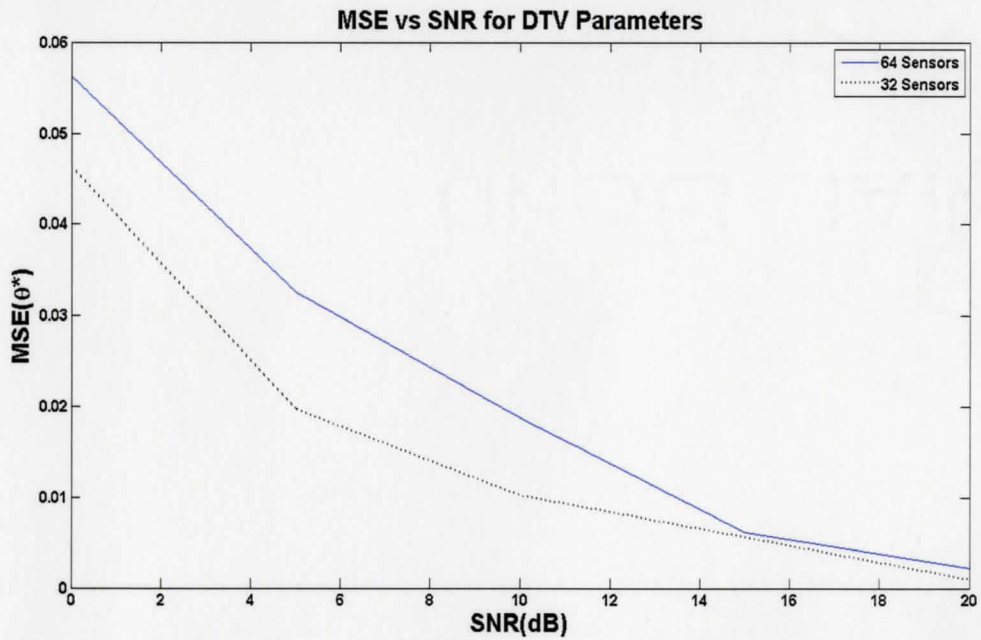Note that we use θ^* to denote $\hat{\theta}$

Figure 5 - 18: MLE from ECG/MCG Sensors for DTI Parameters
Note that we use θ^* to denote $\hat{\theta}$

Figure 5 - 19: MLE from ECG Sensors for DTV Parameters
Note that we use θ^* to denote $\hat{\theta}$

Figure 5 - 20: MLE from ECG/MCG Sensors for DTV Parameters
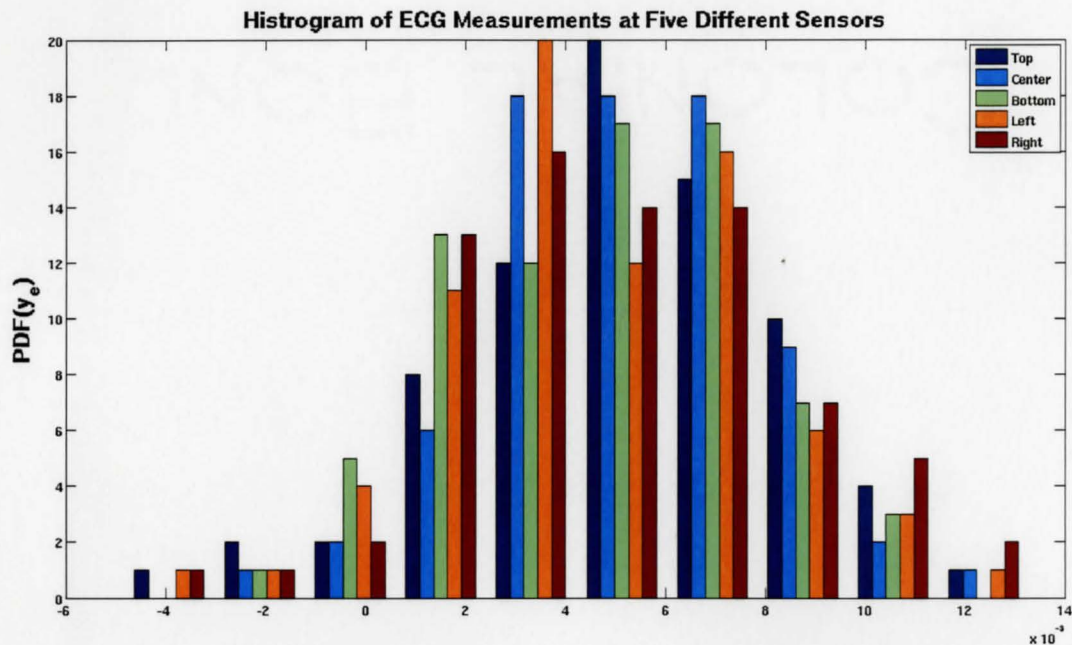Note that we use θ^* to denote $\hat{\theta}$

Figure 5 - 21: Histogram Example for PDF of ECG Measurement Vector. Sensor location relative to center of the heart
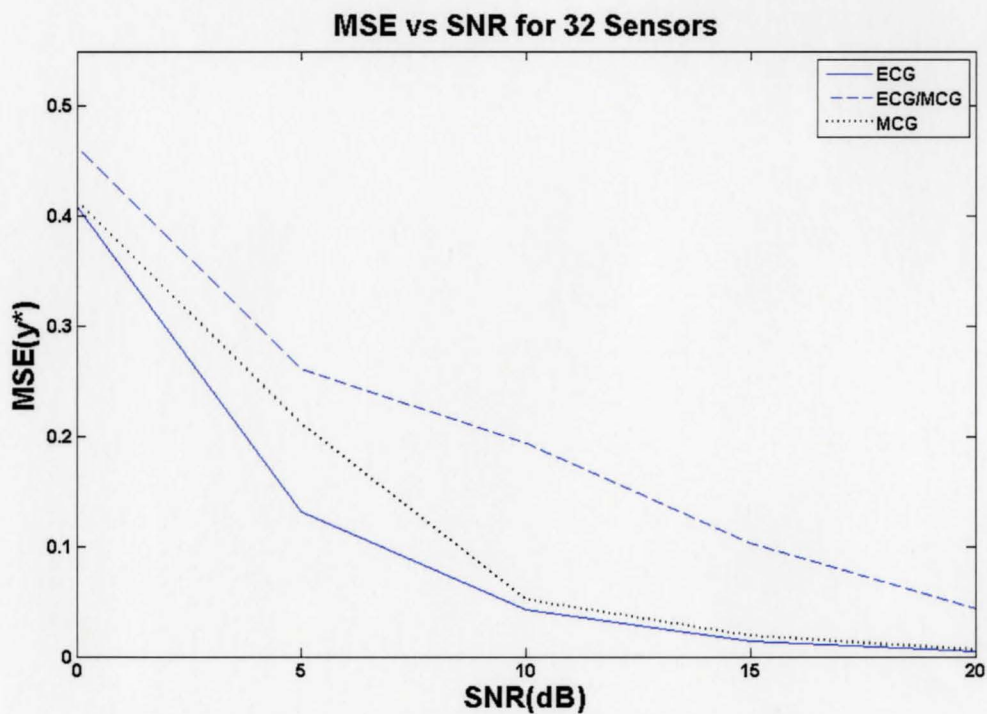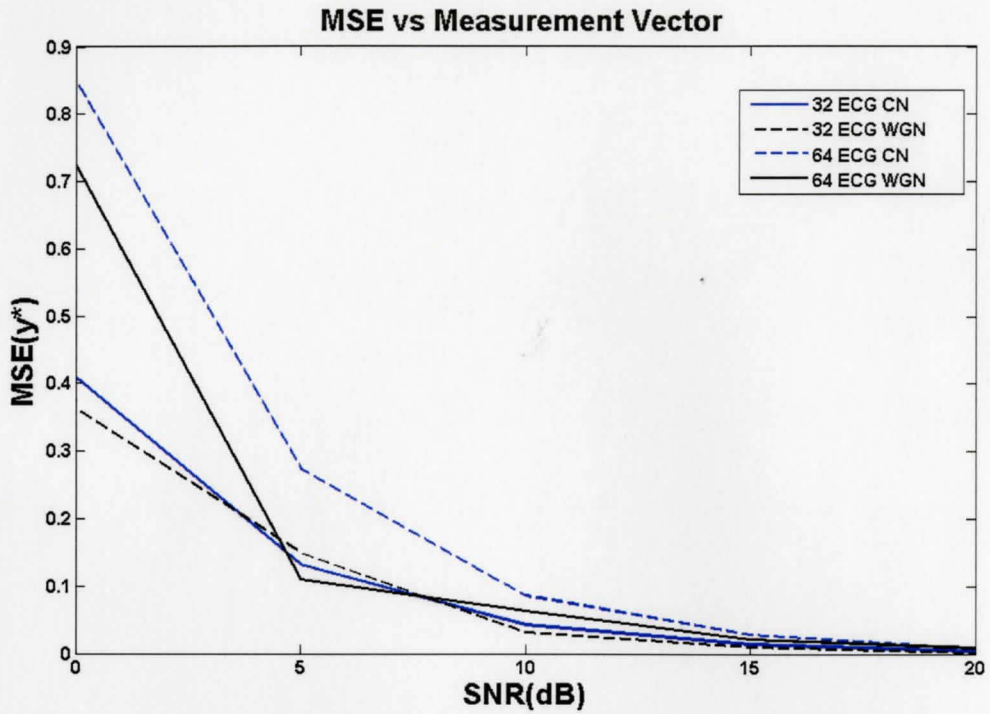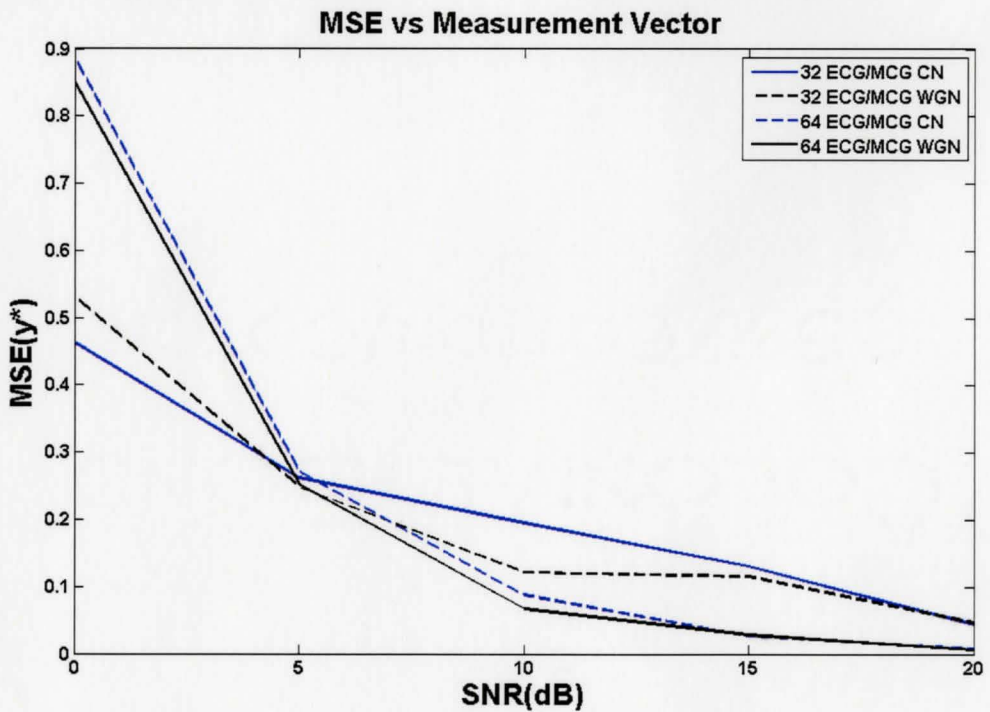

Figure 5 - 22: Curve Fitting Comparison from 32 sensors for ECG/MCG

Note that we use y* to denote $\hat{y}$

Figure 5 - 23: Curve Fitting for ECG Sensors
Note that we use y* to denote $\hat{y}$

Figure 5 - 24: Curve Fitting for ECG/MCG Sensors
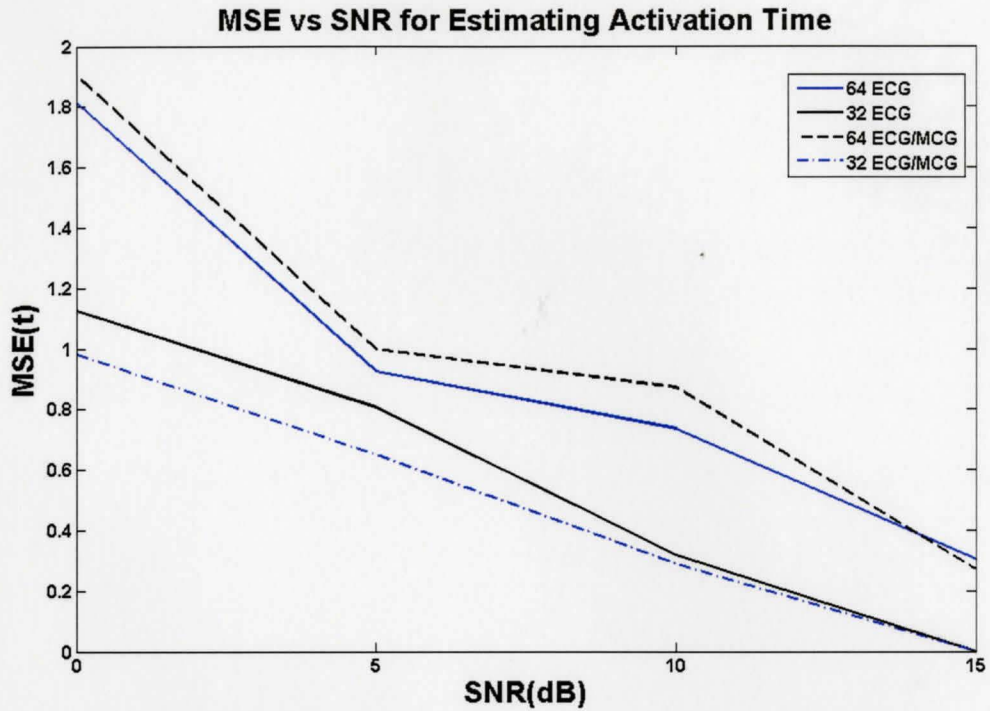Note that we use y* to denote $\hat{y}$

Figure 5 - 25: Estimating Activation Time
Please note we use t to denote τ

Figure 5 - 26: CRB for SNR=5dB from 32 ECG Sensors with White Gaussian Noise

Figure 5 - 27: MSE for LS, MLE and $_{CRB}$ $(\hat{\theta})$ **from 32 ECG Sensors**

Figure 5 - 28: CRB for SNR=5dB from 32 ECG/MCG Sensors with White Gaussian Noise
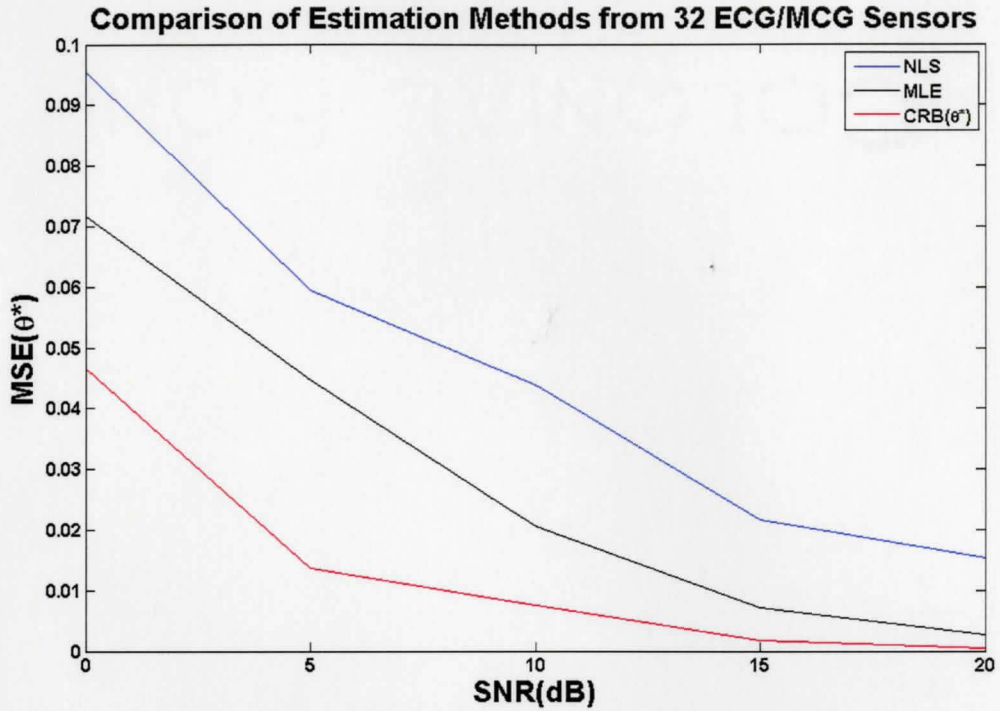
Figure 5 - 29: MSE for LS, MLE and CRB $\left(\hat{\theta}\right)$ **from 32 ECG/MCG Sensors**
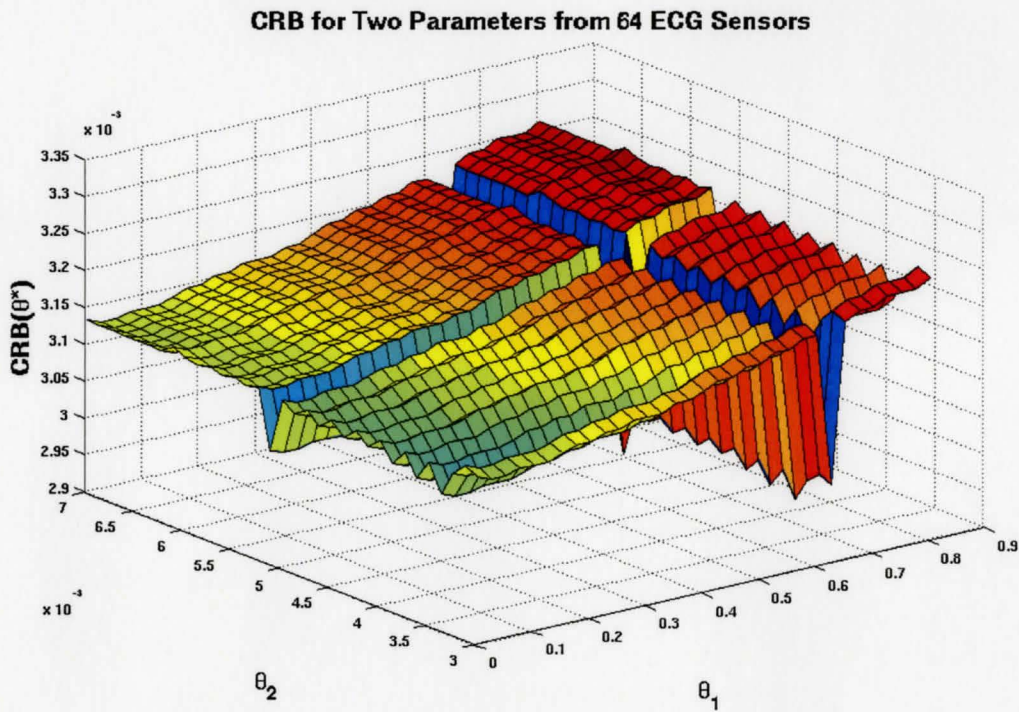
Figure 5 - 30: CRB for SNR=5dB from 64 ECG Sensors with White Gaussian Noise

Comparison of Estimation Methods from 64 ECG Sensors
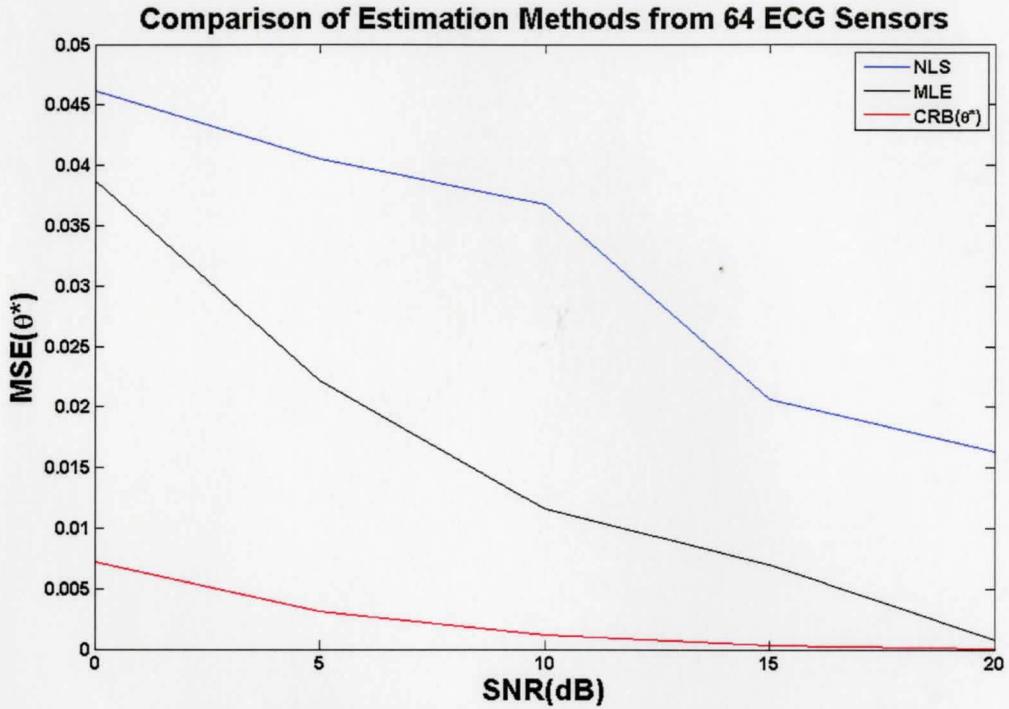
Figure 5 - 31: MSE for LS, MLE and $_{CRB}$ $(\hat{\theta})$ from 64 ECG Sensors
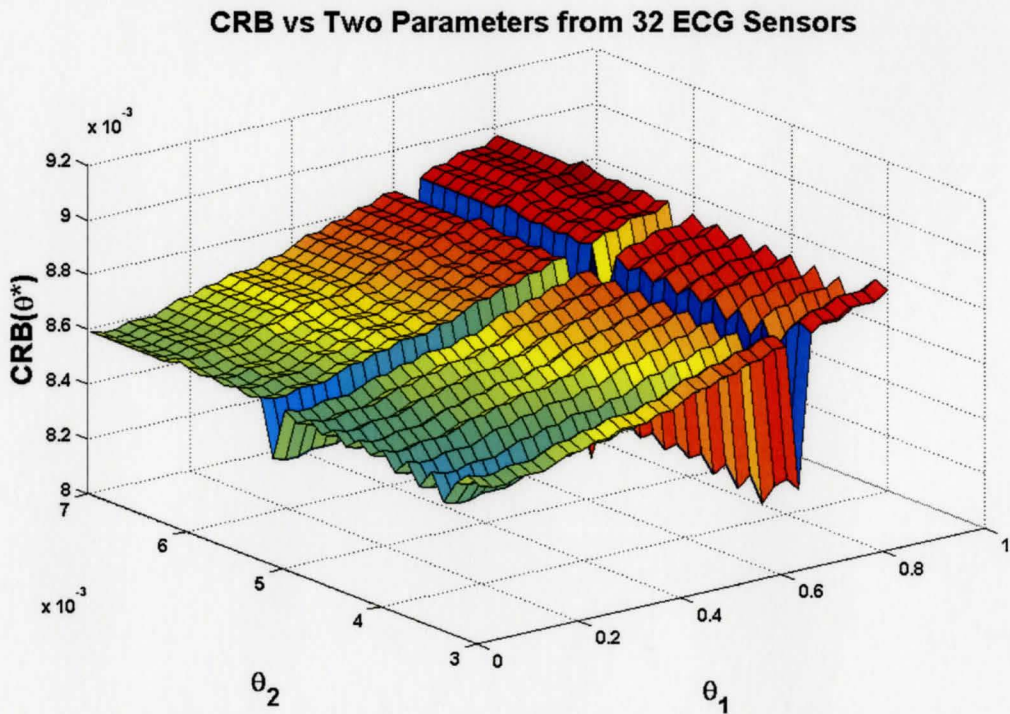
CRB for Two Parameters from 64 ECG/MCG Sensors

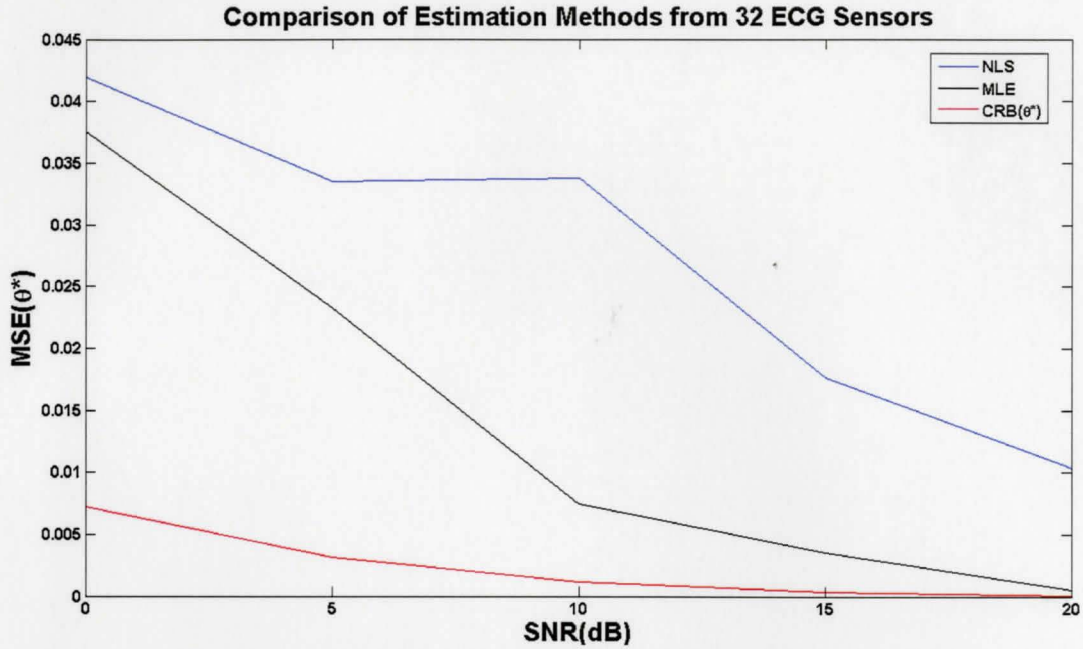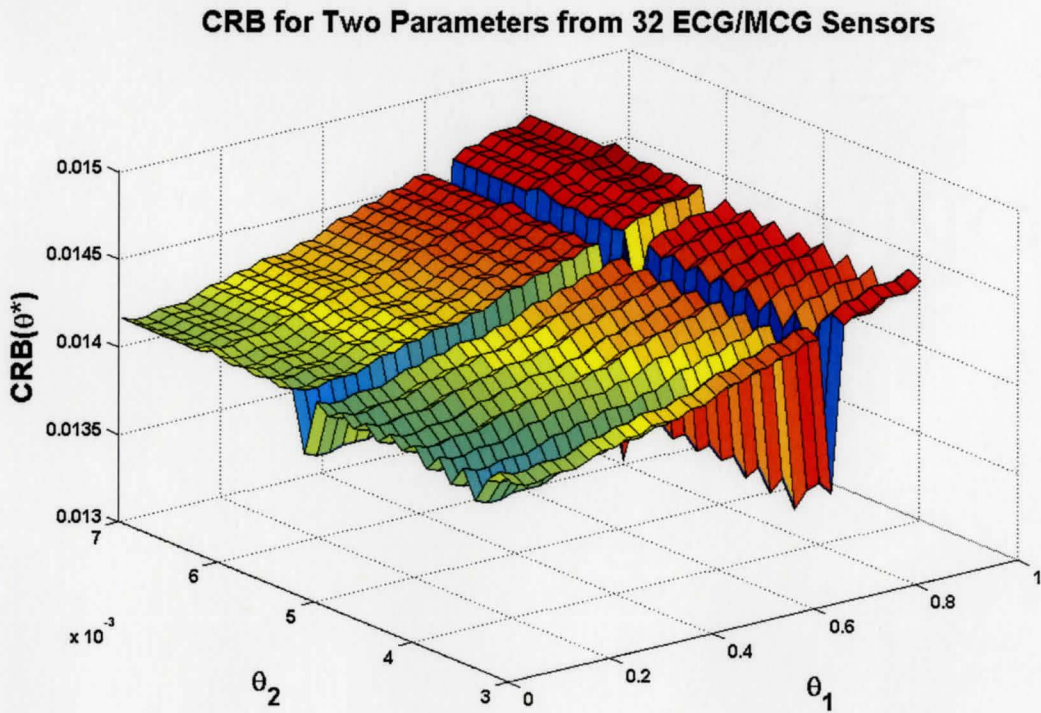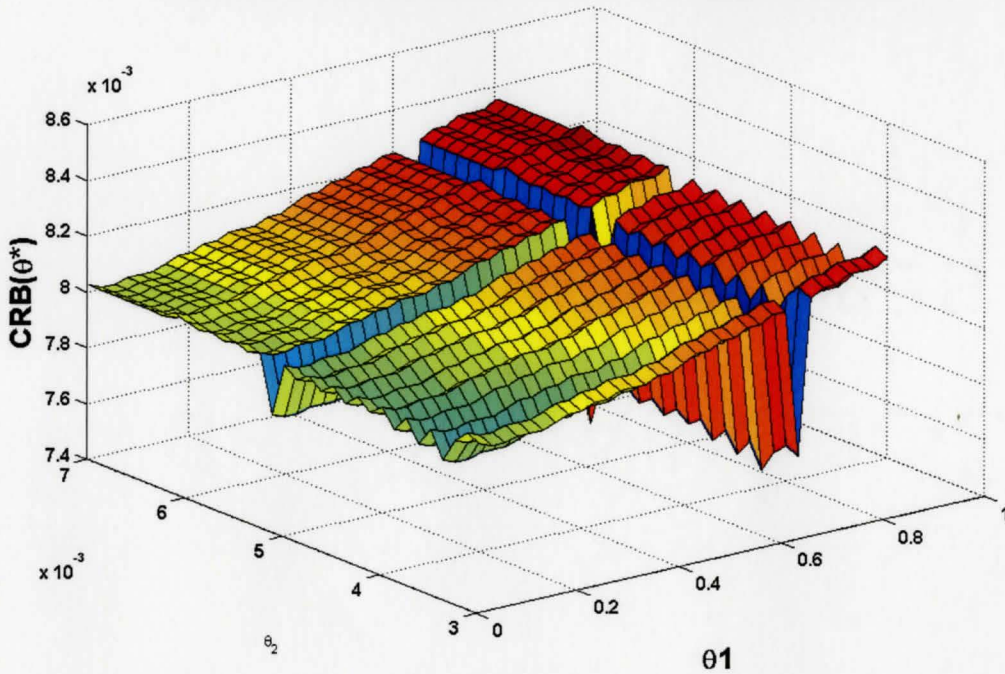Figure 5 - 32: CRB for SNR=5dB from 64 ECG/MCG Sensors with White Gaussian Noise
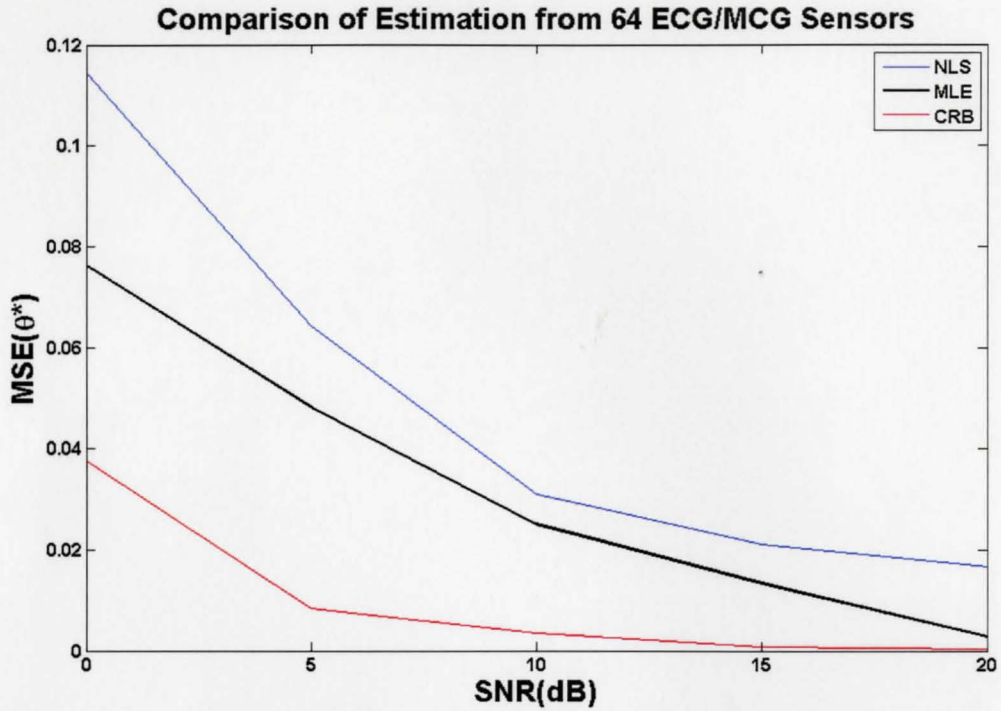
Figure 5 - 33: MSE for LS, MLE and $_{CRB}$ $(\hat{\theta})$ from 64 ECG/MCG Sensors
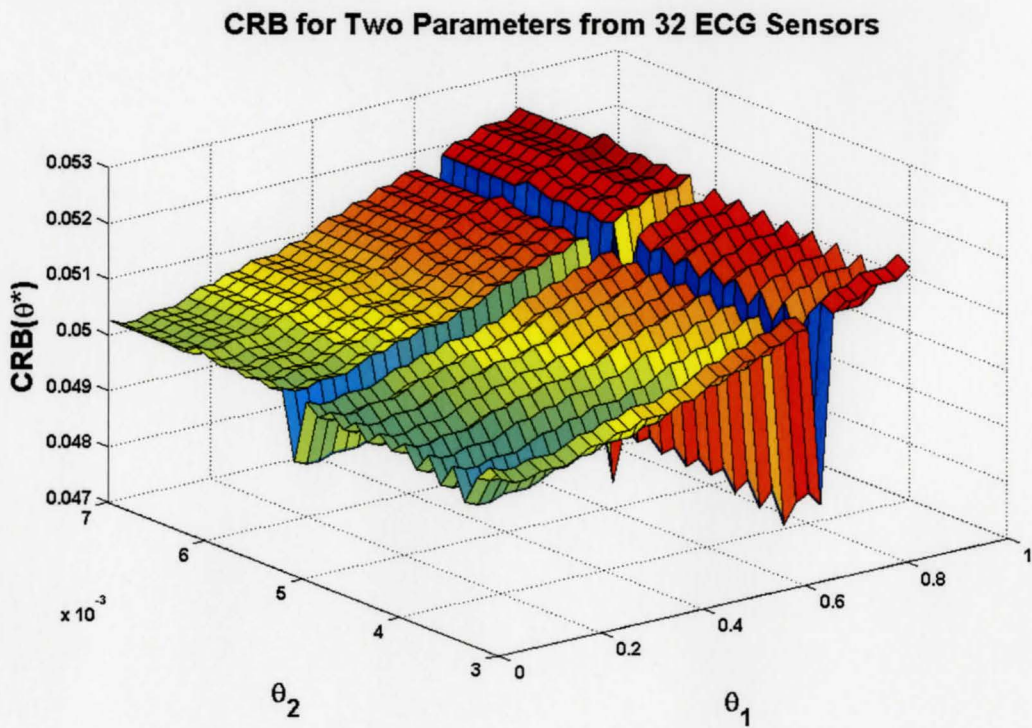
Figure 5 - 34: CRB for SNR=5dB from 32 ECG Sensors with Spatially Correlated Noise

CRB from Two Parameters from 32 ECG/MCG Sensors
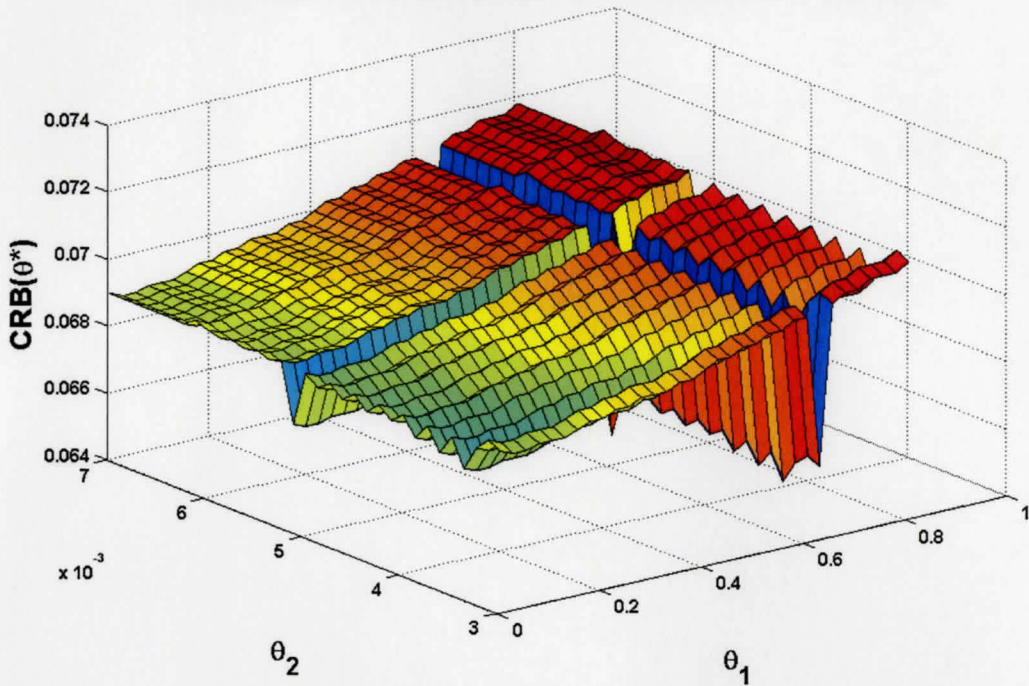
Figure 5 - 35: CRB for SNR=5dB from 32 ECG/MCG Sensors with Spatially Correlated Noise

CRB for Two Parameters from 64 ECG Sensors
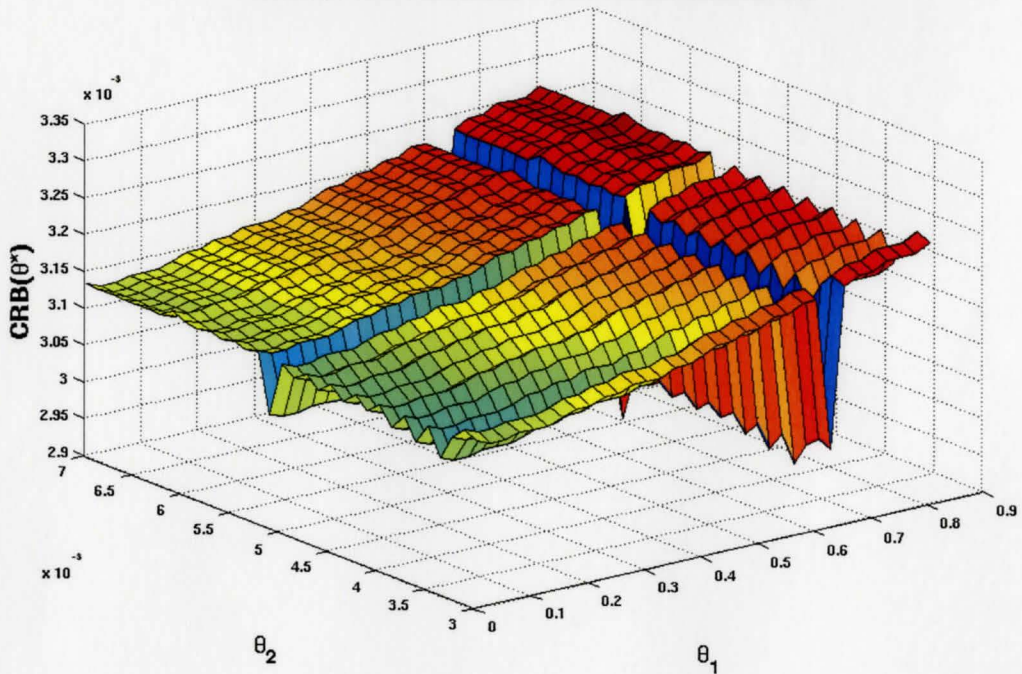
Figure 5 - 36: CRB for SNR=5dB from 64 ECG Sensors with Spatially Correlated Noise

CRB for Two Parameters from 64 ECG/MCG Sensors
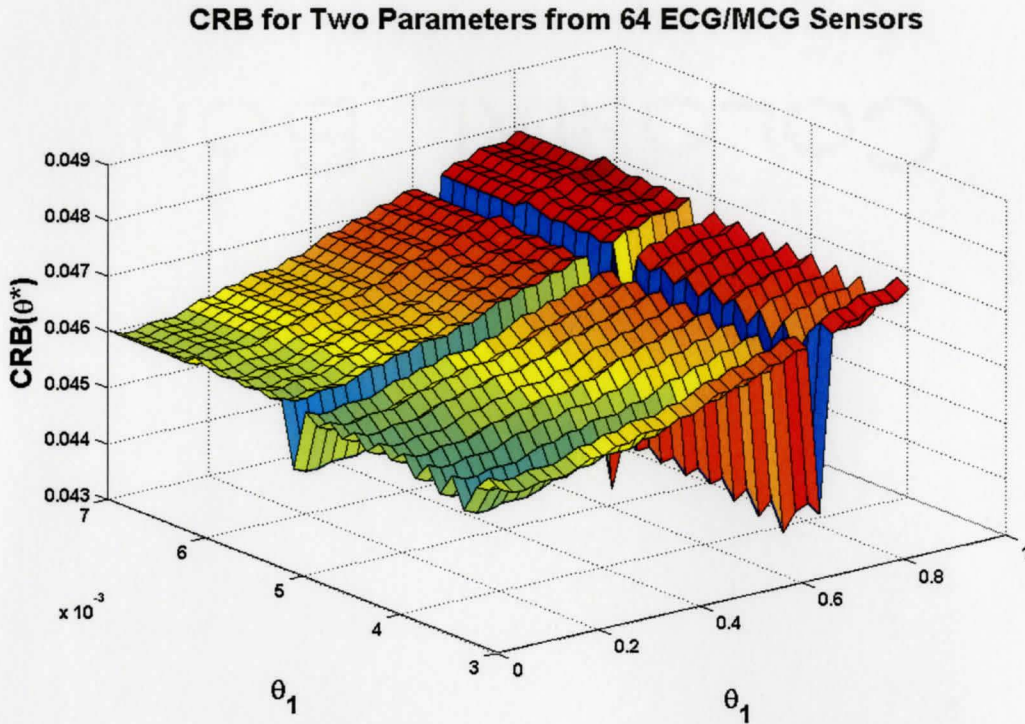
Figure 5 - 37: CRB for SNR=5dB from 64 ECG/MCG Sensors with Spatially Correlated Noise

Comparison of CRB(θ)**

Legend:
- CN - 32
- CN - 64
- WGN - 32
- WGN - 64
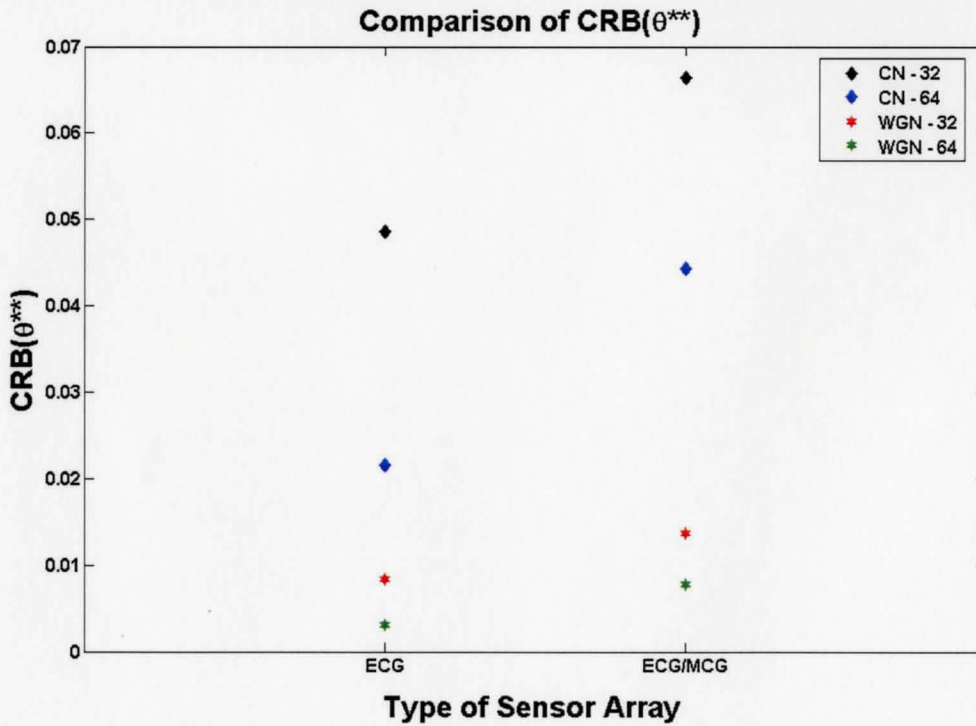
Figure 5 - 38: Comparison of CRB for ECG versus ECG/MCG Sensor Arrays
Note that we use θ** to denote θ

6   CONCLUSION

We proposed a numerical model for the estimation of the physiological parameters of the electrical activation of the heart. We used a diffusion model to describe the wave propagation and our computational model included necessary software tools to simulate ECG/MCG sensor arrays on the torso surface. We demonstrated how the coefficients, which represent diffusion parameters, can be estimated using a non-linear optimization algorithm that minimized the error between the predicted model and the measured data vectors. Our numerical examples included deterministic and stochastic parameters, along with two different model noise distributions. We then analyzed the performance of our model by computing the mean square error for each example, and by computing the CRB to show the lower bound on the variance of the estimator. We showed that estimating the parameters that describe the electrical propagation from ECG/MCG sensors on the human torso surface is feasible. However, the extent to which an improvement is gained by using MCG sensors was not determined as the estimation results were inconclusive.

Future possibilities for this work include the computation of the MLE estimator and CRB when the parameters are stochastic, which we mentioned earlier. Also in terms of the sensor array, certain locations might be less or more sensitive to modeling noise, and different configurations for the sensors as well as increasing the number of channels, are some options for extending this work. From a physiological aspect, cardiac activation

can be affected by changes in heart parameters, for example the loss of cardiac conductivities. This model can also easily be modified to estimate any particular parameter. Another potential application of this estimation model is to be able to locate the region of activation accurately and therefore produce a clearer picture of the electrical activation process. In our work we assumed a constant diffusion coefficient in a homogenous medium which can be extended so that an inhomogeneous reaction-diffusion model is used. Further, the proposed algorithm may be developed to account for arbitrary spatial variation in the diffusivity tensor. The case of an anisotropic medium is also of interest because the extent to which surface measurements are affected by the resulting change in the activation wavefront is still unknown. Further investigation into whether magnetocardiography can provide us with additional clinically valuable information using the diffusion model is needed.

APPENDIX   A

We derive the Geselowitz expressions for the electromagnetic field outside volume conductors as we presented in Chapter 2. To ensure the completeness of the derivations some assumptions are restated here. All derivations are referenced from [Geselowitz, 1967].

In regions that contain no bioelectric sources current density $\mathbf{J}$ is linearly related to $\mathbf{E}$, the electric field intensity.   We assume that the capacitative component of tissue impedance is negligible for small frequencies. Therefore in a region with no bioelectric sources and with conductivity σ, the current density is expressed,

$$\mathbf{J} = \sigma \mathbf{E} \tag{77}$$

We also assume that electromagnetic wave effects can be neglected; the electric field at each instant is therefore computed from the gradient of V, the electric scalar potential,

$$\mathbf{E} = -\nabla V \tag{78}$$

Therefore combining the active regions and those with no bioelectric sources, (77) is modified into

$$\mathbf{J} = \sigma \mathbf{E} + \mathbf{J}^i \tag{79}$$

Since we deemed tissue capacitance as negligible, using (78),

$$\nabla \cdot \mathbf{J} = 0$$
$$\nabla \cdot \mathbf{J}^i = \nabla \cdot \sigma \nabla V = \sigma \nabla^2 V \tag{80}$$

We assume a volume G that is divided into M number of homogenous regions separated

by boundaries S_p, $p = 1, \cdots, M$. Each region is isotropic with $\mathbf{J}^i = \sigma \mathbf{E}$ and is denoted G_p,

$p = 1, \cdots, M$. At each boundary, the electrical potential and the normal component of the

current density are continuous resulting in,

$$
\begin{aligned}
V'(S_p) &= V''(S_p) \\
\sigma'_p \nabla V'(S_p) \cdot \mathbf{n}_p &= \sigma''_p \nabla V''(S_p) \cdot \mathbf{n}_p
\end{aligned}
\tag{81}
$$

where the prime and double prime notation represents each side of the boundary, and the

normal direction is from single prime to double prime. Using Greene's theorem,

$$
\sum_p \int_{S_p} \left[\sigma'_p \left(\left(\frac{1}{R}\right)' \nabla V' - V' \nabla \left(\frac{1}{R}\right)' \right) - \sigma''_p \left(\left(\frac{1}{R}\right)'' \nabla V'' - V'' \nabla \left(\frac{1}{R}\right)'' \right) \right] \cdot dS_p
$$

$$
= \sum_v \int_v \left[\left(\frac{1}{R}\right) \nabla \cdot \sigma \nabla V - V \nabla \cdot \sigma \nabla \left(\frac{1}{R}\right) \right] dv
\tag{82}
$$

where $R = r - r'$ defines the distance between the observation point r and r', a point in

the source region. Then (82) is re-written,

$$
\sum_p \int_{S_p} \left[(\sigma' \nabla V' - \sigma'' \nabla V'') \frac{1}{R} - (\sigma' V - \sigma'' V'') \nabla \left(\frac{1}{R}\right) \right] \cdot dS_p = \sum_v \int_v \frac{1}{R} \nabla \cdot \sigma \nabla V dv + 4\pi \sigma V
\tag{83}
$$

Using the equations from the assumptions made (83) is then transformed as follows,

$$4\pi\sigma V = -\int \frac{1}{R}\nabla \cdot \mathbf{J}^i dv - \sum_p \int_{S_p} V(\sigma' - \sigma'')\nabla\left(\frac{1}{R}\right)\cdot dS_p \qquad (84)$$

The first integral on the right is transformed,

$$\int \nabla \cdot \left(\frac{\mathbf{J}^i}{R}\right)dv = \int \left(\frac{\mathbf{J}^i}{R}\right)\cdot dS = \int \left(\mathbf{J}^i \cdot \nabla\left(\frac{1}{R}\right) + \frac{1}{R}\nabla \cdot \mathbf{J}^i\right)dv \qquad (85)$$

We assume $\mathbf{J}^i$ vanishes on the boundaries S and therefore at the boundary of the region containing the sources,

$$\int \frac{1}{R}\nabla \cdot \mathbf{J}^i dv = -\int \mathbf{J}^i \cdot \nabla\left(\frac{1}{R}\right)dv \qquad (86)$$

Therefore the equation presented in Chapter 2 is derived as,

$$4\pi\sigma V = \int_G \mathbf{J}^i \cdot \nabla\left(\frac{1}{R}\right)dv + \sum_p \int_{S_p} V(\sigma''_p - \sigma'_p)\nabla\left(\frac{1}{R}\right)\cdot dS_p - \int_{S_p} \sigma V \nabla\left(\frac{1}{R}\right)\cdot dS_o \qquad (87)$$

Similar derivations for the magnetic field outside a volume conductor are presented in

[Geselowitz, 1970].

APPENDIX B

We derive the PDF of the measurement vector when the parameters are stochastic. As shown in Chapter 4, the measurement vector which represents the measurement of the electromagnetic fields at the sensors is given by,

$$\mathbf{Y}(\mathbf{r}_i, \mathbf{t}_{j,k}) = \mathbf{a}(\mathbf{r}_i, \mathbf{t}_{j,k}, \boldsymbol{\theta}^k) + \mathbf{e}(\mathbf{r}_i, \mathbf{t}_{j,k}),$$

$$\text{(88)}$$

for $i = 1, \cdots, m, \quad j = 1, \ldots, n, \quad k = 1, \ldots, c$

We assume $z = \mathbf{a}(\mathbf{r}_i, \mathbf{t}_{j,k}, \boldsymbol{\theta}^k)$ and that by definition the PDF is represented as follows,

$$f_Y(y) = \frac{\partial F_Y(\mathbf{y}(\mathbf{r}_i, \mathbf{t}_{j,k}))}{\partial t}$$

$$\text{(89)}$$

where $F_Y(\mathbf{y}(\mathbf{r}_i, \mathbf{t}_{j,k})) = P\{\mathbf{Y} \leq \mathbf{y}\} = P\{\mathbf{a}(\mathbf{r}_i, \mathbf{t}_{j,k}, \boldsymbol{\theta}^k) + \mathbf{e}(\mathbf{r}_i, \mathbf{t}_{j,k}) \leq \mathbf{y}\}$ is the cumulative distribution function given by,

$$F_Y(\mathbf{y}(\mathbf{r}_i, \mathbf{t}_{j,k})) = \int\limits_{e=-\infty}^{e=\infty} \int\limits_{z=-\infty}^{z=y-e} f_{z,e}(\mathbf{z}, \mathbf{e}) dz de$$

$$\text{(90)}$$

where $f_{z,e}(\mathbf{z}, \mathbf{e})$ is the joint PDF. Note that in (78) and (79) the spatio-temporal dependence is implied and reduced notation is used.

Using Leibniz's rule,

$$f_Y(y) = \frac{dF_Y(y)}{dy} = \frac{d(\mathbf{y} - \mathbf{e})}{dy} \cdot f_{z,e}(\mathbf{y} - \mathbf{e}, \mathbf{e}) - \frac{d(-\infty, \mathbf{e})}{dy} \cdot f(-\infty, \mathbf{e}) + \int\limits_{-\infty}^{\infty} \frac{\partial(\mathbf{z}, \mathbf{e})}{\partial y} dz$$

$$\text{(91)}$$

Therefore,

$$f_Y(y) = \int\limits_{e=-\infty}^{\infty} f_{z,e}(\mathbf{y}-\mathbf{e},\mathbf{e})de \qquad (92)$$

Due to independence $f_{z,e}(\mathbf{y}-\mathbf{e},\mathbf{e}) = f_z(\mathbf{y}-\mathbf{e}) * f_e(\mathbf{e})$ and the PDF is then given by,

$$f_Y(y) = f_z\big(\mathbf{y}(\mathbf{r}_i,\mathbf{t}_{j,k}) - \mathbf{e}(\mathbf{r}_i,\mathbf{t}_{j,k})\big) \otimes f_e\big(\mathbf{e}(\mathbf{r}_i,\mathbf{t}_{j,k})\big) \qquad (93)$$

where $z = \mathbf{a}\big(\mathbf{r}_i,\mathbf{t}_{j,k},\mathbf{\theta}^k\big)$ and $\otimes$ represents the convolution operator.

.

REFERENCES

[Abboud, 1993]   Abboud, S., Berenfeld, O. (1993) Simulation of ECG Using a Heart Model with Reaction-Diffusion Action Potentials. *Computers in Cardiology 1993. Proceedings.* 5-8 Sep. pp. 233-236

[Abboud, 1996]   Abboud, S., Berenfeld, O. (1996). Simulation of cardiac activity and the ECG using a heart model with a reaction-diffusion action potential. *Med Eng Phys.* Dec;18(8):615-25.

[Avriel, 2003]   Avriel, M. (2003). Nonlinear Programming: Analysis and Methods. Dover Publishing, New York

[Barrill, 2004]   Barrill, T. (2004). Six Second ECG Workbook. Skillstat Learning Online.

[Baule, 1970]   Baule, GM. McFee, R. (1970). The magnetic heart vector. *American Heart Journal.* Vol.79, No.2, pp.223-236, February.

[Bray, 2002]   Bray, W.O., (2002). The Fitzhugh-Nagumo Model, Nonlinear Dynamics Seminar, University of Maine (unpublished).

[Bub, 2002]   Bub, G. (2002). Optical Mapping of Pacemaker Interactions. PhD Thesis. McGill University

[Cengel, 2003]   Cengel, Y. (2003). Heat Transfer A Practical Approach, 2nd edition, McGraw-Hill, New York.

[Durrer, 1970]   Durrer, D., Th. Van Dam,R., Freud, G. E., Janse, M.J., Meijler, F. L., and Arzbaecher, R.C. (1970). Cardiac Electrophysiology (Cardiac Anatomy, Conduction System, Activation of the Ventricles). *Circulation*, vol.41, pp. 889-912.

[Fitzhugh, 1955]   Fitzhugh R. (1955) Mathematical models of threshold phenomena in the nerve membrane. *Bull. Math. Biophysics*, 17, pp. 257--278

[Geselowitz, 1967]   Geselowitz, D. B., (1967). On Bioelectric Potentials in an inhomogeneous volume conductor. *Biophys. J.*, vol. 7, pp.1-10.

[Geselowitz, 1970]   Geselowitz, D. B., (1970). On the Magnetic Field Generated Outside an Inhomogeneous Volume Conductor by Internal Current Sources. *IEEE transactions on Magnetics*,vol. 6, no.2, pp.346-347.

[Guevara, 1991]   Guevara, M.R. (1991). Theory of Heart. Springer-Verlag, New York.

[Gulrajani, 1998(1)] Gulrajani, R. (1998). Bioelectricity and Biomagnetism. John Wiley & Sons, Inc. New York

[Gulrajani, 1998]   Gulrajani, R. (1998). The Forward and Inverse Problems of Electrocardiography. *IEEE Engineering in Medicine and Biology Magazine*, Volume 17, Issue 5, pp. 84 - 101, 122

[Hodgkin, 1952]   Hodgkin, A.L., Huxley, A.F. (1952). A Quantitative Description of Membrane Current and its Application to Conduction and Excitation in Nerve. *J.Physiol.*,117, pp.500-544.

[Holden, 1998]   Holden, A. (1998) Nonlinearity in the Heart. *Physics World,* pp.29-34

[Horacek, 1995]   Horacek, B.M. (1995). The forward and inverse problem of electrocardiography. *In: Ghista, D.N.(Ed): 2nd Gauss Symposium: Medical Mathematics and Physics*. Vieweg-Verlag, Wiesbaden.

[Itozaki, 2003]   Itozaki, Hideo. (2003). SQUID Application research in Japan. *Supercond. Sci. Technol.*16, pp. 1340-1343

[Jeremic, 2000]   Jeremic, A.,Nehorai, A. (2000). Estimating Current Density in the Heart using ECG/MCG Spatio-temporal Analysis, *IEEE Int. Conf Acoust., Speech,Signal Processing.*, Volume 1, pp. 323 - 327(2000)

[Jeremic, 2003]   Jeremic, A., Nehorai, A. (2003). Estimating Current Density in the Heart Using Structured and Unstructured Covariance Analysis. *IEEE EMBS,* Cancun, Mexico.

[Jin, 2002]   Jin, J. (2002). The Finite Element Method in Electromagnetics. John Wiley & Sons, Inc. New York

[Kay, 1993]   Kay, S. (1993). Fundamentals of Statistical Signal Processing: Estimation Theory. Prentice Hall, New Jersey

[Koch, 2001]   Koch, Hans. (2001). SQUID Magnetocardiography: Status and Perspectives. *IEEE Transactions on Applied Superconductivity*, Vol 11, No. 1, March 2001

[Lagarias, 1998]   Lagarias, J.C., J. A. Reeds, M. H. Wright, and P. E. Wright (1998), Convergence Properties of the Nelder-Mead Simplex Method in Low Dimensions, *SIAM Journal of Optimization*, Vol. 9 Number 1, pp. 112-147, 1998.

[Macfarlane,1989]   Macfarlane PW, Lawrie TDV (eds.) (1989): *Comprehensive Electrocardiology: Theory and Practice in Health and Disease*, 1st ed., Vols. 1, 2, and 3, pp. 1785. Pergamon Press, New York.

[MacLeod,1998]   MacLeod, R., Brooks, D. (1998). Recent Progress in Inverse Problems in Electrocardiology. *IEEE EMBS Magazine*, 17(1), 73-83

[Martini, 1999]   Martini, R. (1999). Fundamentals of Anatomy and Physiology. 5th edition. Prentice Hall 1998

[Malmivuo, 1995]   Malmivuo, J., Plonsey, R. (1995). Bioelectromagnetism – Principles and Applications of Bioelectric and Biomagnetic Fields, Oxford University Press, New York. Chapter 7.

[Moreau, 2004]   Moreau-Villéger , V., Delingette, H., Sermesant, M., Faris, O. McVeigh, E., Ayache, N. Global and local parameter estimation of a model of the electrical activity of the heart. *Rapport de recherche de l'INRIA - Sophia Antipolis , Equipe : EPIDAURE* Juillet 2004 - Document en anglais

[Nerbonne, 2000]   Nerbonne, J. (2000). Molecular basis of functional voltage-gated K^+ channel diversity in the mammalian myocardium. *Journal of Physiology*, 525(2), pp. 285-298

[Noble, 1962]   Noble, D. (1962). A Modification of the Hodgkin-Huxley Equations Applicable to Purkinje Fibre Action and Pace-maker Potentials. *Journal of Physiology* , 160, pp. 317-352

[Panfilov, 1996]   Panfilov, A., Aliev, R. (1996). A simple two-variable model of cardiac excitation. *Chaos Solitons and Fractals* 7(3), 293 - 301

[Plonsey, 1974]   Plonsey, R. (1974). The Formulation of Bioelectric Source-field Relationships in Terms of Surface Discontinuities. *J. Franklin Inst.*, vol. 297, pp.317-324.

[Plonsey, 1982]   Plonsey, R., Pilkington. (1982). Engineering Contributions to Biophysical Electrocardiography. IEEE Press, New York.

[Rogers, 1994]   Rogers, J., McCulloh, A. (1994). A Collocation – Galerkin Finite Element Model of Cardiac Action Potential Propagation . *IEEE Transactions on Biomedical Engineering.,*vol. 41 (8)

[Rudy, 1988]   Rudy, y., Messinger-Rapport, B.J. (1988). The Inverse Solution in Electrocardiography: Solutions in terms of Epicardial Potentials. *CRC Crit Rev Biomed Eng* 16:215-269

[Sachse, 2004]   Sachse, Frank B. (2004). Computational Cardiology, Springer,Germany

[Steinburg, 2005]   Steinberg , B.A. Roguin, A. Watkins, S. Hill, P. Fernando, D., Resar, J. (2005). Magnetocardiogram Recordings in a Nonshielded Environment—Reproducibility and Ischemia Detection . *Annals of Noninvasive Electrocardiology.* 10 (2), pp.152–160.

[Varghese, 1995]   Varghese, A. (1995). The Biomedical Engineering Handbook, Chapter 11, Membrane Models. CRC Press. pp. 139-161